

NASA/CR—2011-216977



Integration of NASA-Developed Lifing Technology for PM Alloys into DARWIN[®]

*R. Craig McClung, Michael P. Enright, and Wuwei Liang
Southwest Research Institute, San Antonio, Texas*

March 2011

NASA STI Program . . . in Profile

Since its founding, NASA has been dedicated to the advancement of aeronautics and space science. The NASA Scientific and Technical Information (STI) program plays a key part in helping NASA maintain this important role.

The NASA STI Program operates under the auspices of the Agency Chief Information Officer. It collects, organizes, provides for archiving, and disseminates NASA's STI. The NASA STI program provides access to the NASA Aeronautics and Space Database and its public interface, the NASA Technical Reports Server, thus providing one of the largest collections of aeronautical and space science STI in the world. Results are published in both non-NASA channels and by NASA in the NASA STI Report Series, which includes the following report types:

- **TECHNICAL PUBLICATION.** Reports of completed research or a major significant phase of research that present the results of NASA programs and include extensive data or theoretical analysis. Includes compilations of significant scientific and technical data and information deemed to be of continuing reference value. NASA counterpart of peer-reviewed formal professional papers but has less stringent limitations on manuscript length and extent of graphic presentations.
- **TECHNICAL MEMORANDUM.** Scientific and technical findings that are preliminary or of specialized interest, e.g., quick release reports, working papers, and bibliographies that contain minimal annotation. Does not contain extensive analysis.
- **CONTRACTOR REPORT.** Scientific and technical findings by NASA-sponsored contractors and grantees.

- **CONFERENCE PUBLICATION.** Collected papers from scientific and technical conferences, symposia, seminars, or other meetings sponsored or cosponsored by NASA.
- **SPECIAL PUBLICATION.** Scientific, technical, or historical information from NASA programs, projects, and missions, often concerned with subjects having substantial public interest.
- **TECHNICAL TRANSLATION.** English-language translations of foreign scientific and technical material pertinent to NASA's mission.

Specialized services also include creating custom thesauri, building customized databases, organizing and publishing research results.

For more information about the NASA STI program, see the following:

- Access the NASA STI program home page at <http://www.sti.nasa.gov>
- E-mail your question via the Internet to help@sti.nasa.gov
- Fax your question to the NASA STI Help Desk at 443-757-5803
- Telephone the NASA STI Help Desk at 443-757-5802
- Write to:
NASA Center for AeroSpace Information (CASI)
7115 Standard Drive
Hanover, MD 21076-1320

NASA/CR—2011-216977



Integration of NASA-Developed Lifing Technology for PM Alloys into DARWIN[®]

*R. Craig McClung, Michael P. Enright, and Wuwei Liang
Southwest Research Institute, San Antonio, Texas*

Prepared under Contract NNC08CB06C

National Aeronautics and
Space Administration

Glenn Research Center
Cleveland, Ohio 44135

March 2011

Trade names and trademarks are used in this report for identification only. Their usage does not constitute an official endorsement, either expressed or implied, by the National Aeronautics and Space Administration.

Level of Review: This material has been technically reviewed by NASA technical management.

Available from

NASA Center for Aerospace Information
7115 Standard Drive
Hanover, MD 21076-1320

National Technical Information Service
5301 Shawnee Road
Alexandria, VA 22312

Available electronically at <http://www.sti.nasa.gov>

TABLE OF CONTENTS

	<i>Page</i>
1.0 INTRODUCTION	1
1.1 Background.....	1
1.2 Approach	2
2.0 STATUS SUMMARIES	5
2.1 Research in P/M Lifting Conducted at NASA Glenn Research Center	5
2.1.1 Determination of Anomaly Distributions	5
2.1.2 Calculation of Fracture Probability	9
2.2 A Summary of Current DARWIN Capabilities Relevant to P/M Lifting.....	16
2.2.1 Determination of Anomaly Distributions	17
2.2.2 Calculation of Fracture Probability	17
3.0 ALGORITHM DEVELOPMENT.....	25
3.1 Algorithms for Multiple Anomaly Types.....	25
3.1.1 Introduction	25
3.1.2 Estimating Marginal Probability Densities from Component Failure Data	27
3.1.3 Application to Gas Turbine Engine Materials	35
3.2 Development of an Unfolding Algorithm for Estimating Spheroid Parameters from Sectioning Data Measurements.....	42
3.2.1 Introduction	42
3.2.2 The Stereological Equation	42
3.2.3 Numerical Solution of the Stereological Equation	43
3.2.4 Application Example.....	44
3.2.5 Discussion.....	49
3.3 Algorithms for Modeling the Growth Rates of Small Fatigue Cracks	50
3.3.1 Introduction	50
3.3.2 Analysis Methods	50
3.3.3 Results	52
3.3.4 Discussion.....	59

TABLE OF CONTENTS (cont.)

	<i>Page</i>
4.0 PROGRAM PLAN FOR FUTURE RESEARCH	61
5.0 SUMMARY	65
6.0 BIBLIOGRAPHY	67

LIST OF FIGURES

<i>Figure</i>	<i>Page</i>
1. Crack formation computations are performed via a user-supplied crack formation module.....	18
2. The conditional probability of fracture failure $P(F d)$ of multiple anomaly materials is dependent on the number of anomalies j at a specified location in the component.....	22
3. For multiple anomaly materials, both the probability of fracture given an anomaly $P(F_i d_j)$ and the anomaly occurrence probability $P(d_i)$ are dependent on the number of anomalies present.....	22
4. For components with multiple anomalies of multiple types at multiple locations, the probability of failure can be modeled using several nested series systems to represent the various failure events.	24
5. Analytical probability of failure values associated with single and multiple anomalies of a single type for the example component containing multiple anomaly types.....	28
6. Analytical and simulated probability of failure of failure values for the example component containing two anomaly types were in close agreement, as expected.	30
7. CDF values for individual anomaly types estimated from censored failure data were significantly different from the analytical values.	31
8. CDF values for individual anomaly types estimated using the combined Kaplan-Meier/Meeker-Escobar approach were in close agreement with the analytical values.	34
9. The transformed CDF values based on the Kaplan-Meier/Meeker-Escobar approach were in close agreement with the analytical parent distributions.	35
10. The marginal CDFs for each anomaly type were obtained from the Kaplan-Meier/Meeker-Escobar fit of the failure data.....	38

LIST OF FIGURES (cont.)

<i>Figure</i>	<i>Page</i>
11. The parent CDFs were determined by transforming the marginal CDF values for each anomaly type.	39
12. The influence of volume to surface area ratio on probability of failure and associated contribution of: (a) surface NMPs, (b) subsurface NMPs, and (c) surface pores.	40
13. Bivariate histograms (stereograms) of anomaly size and shape parameter associated with anomalies in the fictitious material: (a) original population of spheroids, and (b) predicted population of spheroids based on sectioning data transformed using the Cruz-Orive unfolding algorithm.	46
14. Influence of the number of section plane measurements on predicted spheroid size parameter values: (a) 10 × 10 bin grid, and (b) 5 × 5 bin grid.	47
15. Influence of the number of section plane measurements on predicted spheroid shape parameter values: (a) 10 × 10 bin grid, and (b) 5 × 5 bin grid.	48
16. Schematic Kitagawa diagram relating smooth specimen fatigue endurance limit ($\Delta\sigma_e$) and large-crack threshold (ΔK_{th}).	51
17. Comparison of small-crack and large-crack growth rate data for Ti-6Al-4V tested by Lenets <i>et al.</i> and Caton <i>et al.</i> at $R = 0.1$	53
18. Comparison of small-crack and large-crack growth rate data for Ti-6Al-4V tested by Lenets <i>et al.</i> and Caton <i>et al.</i> at $R = 0.1$, with small-crack data adjusted using El Haddad parameter.	54
19. Comparison of small-crack and large-crack growth rate data for IN-100 tested by Jha <i>et al.</i> at $R = 0.05$	55
20. Comparison of small-crack and large-crack growth rate data for IN-100 tested by Jha <i>et al.</i> at $R = 0.05$, with small-crack data adjusted using two estimates of the El Haddad parameter.	55
21. Comparison of small-crack and large-crack growth rate data for U720 at $R = -0.33$	57
22. Comparison of small-crack and large-crack growth rate data for U720 at $R = -0.33$, with small-crack data adjusted using El Haddad parameter.	57
23. Comparison of small-crack and large-crack growth rate data for U720 at $R = -1$	58
24. Comparison of small-crack and large-crack growth rate data for U720 at $R = -1$, with small-crack data adjusted using El Haddad parameter.	58

LIST OF TABLES

<i>Table</i>	<i>Page</i>
1. Anomaly Parameters for Example Component Containing Two Types of Anomalies	28
2. Simulated Failure of Example Component with Two Types of Anomalies	29
3. Simulated CDF Values for Example Component Containing Two Types of Anomalies	29
4. Failure CDF for Anomaly Type A Using Kaplan-Meier Approach Combined with Meeker-Escobar Data Fit	33
5. Failure CDF for Anomaly Type B Using Kaplan-Meier Approach Combined with Meeker-Escobar Data Fit	33
6. Anomaly Types Associated with Nickel-Based Superalloy Test Specimens	35
7. Component Failure CDF for Nickel-Based Superalloy Smooth Specimen Fatigue Failure Data with Applied Stress of 1100 MPa	36
8. Failure CDF for Surface NMPs Using Kaplan-Meier/Meeker-Escobar Approach	37
9. Failure CDF for Subsurface NMPs Using Kaplan-Meier/Meeker-Escobar Approach	37
10. Failure CDF for Surface Pores using Kaplan-Meier/Meeker-Escobar Approach	38
11. Influence of Component Volume to Surface Area Ratio on Number of Anomalies for Each Anomaly Type.....	39
12. Spheroid Parameters Associated with Application Example	45

1.0 INTRODUCTION

In recent years, Southwest Research Institute[®] (SwRI[®]) and NASA Glenn Research Center (GRC) have worked independently on the development of probabilistic lifing methods for materials used in gas turbine engine rotors. The two organizations have addressed different but complementary technical challenges. This final report summarizes a brief investigation into the current status of relevant technology at SwRI and GRC with a view towards a future integration of methods and models developed by GRC for probabilistic lifing of powder metallurgy (P/M) nickel turbine rotor alloys into the DARWIN[®] software developed by SwRI.

1.1 Background

Previous Activity at SwRI. Work at SwRI was originally motivated by incidents involving uncontained rotor fracture at Sioux City, Iowa, in 1989 and Pensacola, Florida, in 1996. As a result of these incidents, the Federal Aviation Administration (FAA) requested that the aircraft engine industry, through the Aerospace Industries Association (AIA) Rotor Integrity Sub-Committee (RISC), review available techniques to determine whether a damage tolerance approach could be introduced to produce a reduction in the rate of uncontained rotor events. During the development of this probabilistic damage tolerance approach, it became apparent to RISC that the capabilities and effectiveness of the emerging technology could be significantly enhanced by further research and development. SwRI, in partnership with four major U.S. engine manufacturers and with guidance from RISC, proposed and was awarded a series of major FAA grants beginning in 1995 to address identified shortfalls in technology and data.

One of the key outcomes of this work has been the probabilistic damage tolerance computer code DARWIN (Design Assessment of Reliability With INspection). DARWIN integrates finite element models and stress analysis results, fracture mechanics models, material anomaly data, probability of anomaly detection, and uncertain inspection schedules with a user-friendly graphical user interface (GUI) to determine the probability-of-fracture of a high-energy rotating component as a function of operating cycles with and without inspections.

Initial DARWIN capabilities were focused on the hard alpha titanium problem, which had caused the Sioux City incident. Later DARWIN work focused on surface damage at machined circular holes, which had caused the Pensacola incident. With direct guidance from the FAA, DARWIN has been tailored to address specific advisory circulars issued by the FAA, including AC 33.14-1 for titanium hard alpha, AC 33.70-2 on circular holes in all materials, and the more general AC 33.70-1 for all engine life-limited parts. The FAA has indicated that DARWIN is an acceptable means of compliance with these advisory circulars, and DARWIN has been employed in the formal FAA certification process for numerous engines.

Some elementary DARWIN capabilities have also been developed to address superalloys with high anomaly occurrence rates, including probabilistic three-dimensional (3D) descriptions of anomaly sizes and orientations, and provisions for users to integrate their own probabilistic crack formation life modules. However, this work has been limited due to other, more pressing FAA and RISC priorities, and additional effort on these topics is not planned under the current FAA grant.

At the request of the FAA and the engine industry, SwRI began licensing and providing formal user support for DARWIN in 2000. Currently DARWIN is licensed by six aircraft engine companies and two foreign government laboratories. DARWIN is also available on a royalty-free basis to all U.S. government agencies.

Previous Activity at NASA Glenn Research Center. For more than twelve years, GRC has been actively investigating and developing models for the fatigue behavior of P/M nickel-based alloys that are being increasingly used in high energy rotating components for gas turbine engines. These alloys have many advantages over conventionally cast and wrought alloys, but they suffer from the rare occurrence of non-metallic defects (ceramic inclusions) that arise from the powder atomization process. These inclusions can have a potentially large detrimental effect on the fatigue life of individual components. GRC activity has primarily focused on understanding and modeling the effects of ceramic inclusions on fatigue life, and on developing improved life prediction methods that could be applied to components. The work has resulted in the development of an extensive and unique data base that captures the relationships between inclusion size and shape distributions and the low cycle fatigue life for various temperature and stress regimes. Probabilistic models and algorithms have been developed that simulate the effect of inclusion occurrence rate, size distribution and material processing forging strains on fatigue life. Work is continuing to refine these models further and to begin their verification and validation.

1.2 Approach

This report summarizes a joint critical review of previous work by SwRI and GRC to identify specific GRC data and models that could be integrated into DARWIN, to identify new DARWIN functionality that must be developed to enable this integration, to identify additional data or models that are needed, and then to outline a program plan to accomplish the desired integration. Some initial work was also performed to begin developing some of the needed algorithms.

This critical review began by SwRI and GRC each compiling and presenting to the other organization a detailed briefing describing the relevant background technology. SwRI summarized current DARWIN capabilities with special emphasis on multiple anomaly materials, while GRC summarized their existing data and models for P/M materials. SwRI then performed a detailed review and critique of this work, with a focus on determining how existing GRC data and models could fit into current DARWIN capabilities, as well as identifying apparent gaps in current DARWIN capabilities.

This briefing and the first critique was conducted at a face-to-face initial technical exchange meeting conducted at Honeywell Aerospace in Phoenix, Arizona on December 9, 2008. The main attendees were Jack Telesman and Peter Bonacuse from GRC, Craig McClung and Michael Enright from SwRI, and Peter Kantzos (formerly at GRC) from Honeywell. Most of the meeting was devoted to a series of technical presentations that summarized previous work at GRC and SwRI applicable to P/M lifing.

This technical exchange meeting launched efforts to develop formal written summaries of the existing data, models, and software, along with an initial assessment of future needs. These written summaries are provided in Section 2 of this final report.

New algorithm development was conducted in three areas. First, a methodology for estimating anomaly distributions for materials in which multiple anomaly types are operative was developed and verified. Second, an unfolding algorithm to estimate the dimensions and orientations of 3D spheroids based on 2D sectioning measurements was implemented and investigated. Third, the behavior of small fatigue cracks in U720 tests conducted by GRC was investigated, and an existing model to predict this small-crack behavior from large-crack growth rates was evaluated. These activities are described in Section 3.

One of the primary objectives of the current study was to identify technologies for assessment of P/M materials developed at GRC that could be transferred for use by gas turbine engine manufacturers. Based on the GRC status summary and the DARWIN capabilities summary, several technology gaps were identified related to (1) characterization and simulation of 3D anomalies based on data from different types of inspections, (2) understanding and analysis of anomaly deformation and breakup during the forging process, and (3) treatment of various factors that can influence fatigue crack growth lives. A program plan for the development and implementation of key algorithms and software modules in DARWIN to address the technology gaps was developed and is described in Section 4.

It was originally envisioned that, during the course of this project, SwRI would interact with all four of the major U.S. aircraft engine manufacturers as well as other government agencies that are performing research in the subject areas. This communication and consultation would be designed to assess previous industry work in this area and to provide a formal overview of the technical exchange activities conducted during this year, as well as the status summaries and program plans. The manufacturers and the government agencies would be invited to review and comment on this information, and their interest in participating in future implementation efforts would be assessed. However, as the funding scenario for future efforts changed, NASA GRC directed that this communication and consultation effort be de-emphasized at the present time. Informal conversations were conducted with two of the four manufacturers on topics of specific interest. In addition, relevant public domain literature authored by staff from various aircraft engine manufacturers was critically reviewed. About twenty technical reports, journal articles, and conference papers related to fatigue life prediction of P/M alloys were included in this exercise. A formal written summary was not prepared.

(This page intentionally left blank.)

2.0 STATUS SUMMARIES

2.1 Research in P/M Lifting Conducted at NASA Glenn Research Center

For more than ten years, NASA Glenn Research Center has been actively investigating and developing models for the fatigue behavior of powder metallurgy (P/M) nickel-based alloys used in high energy rotating components for gas turbine engines. The purpose of this section is to provide an overview of the major investigations and findings at GRC. The technical details are not repeated here, but GRC publications and presentations that provide those details are thoroughly cited. This status summary is an important first step towards the development of a plan for further research and development activities that would be necessary to integrate the GRC technology into the DARWIN software.

The GRC investigations focused on a single materials system—Udimet[®] 720—in both seeded and unseeded forms. Therefore, some of the specific conclusions of the GRC work may be limited to this specific material. However, it was the intent of GRC, and it is the intent of the current survey, to identify phenomena, relationships, and methods that are applicable to a broad range of P/M superalloys.

The GRC seeded investigations included two different types of seeds. One set of artificial inclusions was made of crushed Alcoa T64 alumina, a common crucible material, selected to represent a hard, blocky Type I inclusion. These seeds were screened to different size ranges in different studies, including -140/+170 mesh (nominal diameter 122 μm) and -80/+100 mesh. A second seed type was produced by crushing pre-baked Ram 90 alumina crucible paste, representative of soft/friable Type II inclusions. The Ram 90 seeds were screened to mesh sizes of either -270/+325 (nominal diameter 54 μm) or -140/+170. The base material was production quality U720 powder screened to -270 mesh and processed conventionally. Seeds did not affect the resultant microstructure. Seeding rates were chosen to ensure an appropriate number of surface inclusions in fatigue test specimens.

The GRC research can be organized into two broad categories. The first category involves the determination of the proper statistical descriptions of anomaly size, shape, and frequency. These anomaly distributions would then be used as input to the reliability calculations. The second category involves the calculation of the probability of fracture of a coupon or component, given that an anomaly is present. This determination involves some treatment of fatigue crack formation life and fatigue crack growth life, including the effects of various residual stresses.

2.1.1 Determination of Anomaly Distributions

Because non-metallic inclusions and other metallurgical defects can have a significant deleterious effect on the fatigue performance of P/M superalloys, the “cleanliness” of a particular alloy or material lot is a critical characteristic. Kantzos *et al.* (2004) have correctly emphasized that both the size and number of inclusions must be considered to characterize cleanliness.

Three different sources of data may be available to determine anomaly sizes and frequencies. The first is measurements of inclusions that have been completely separated from the matrix material, the second is measurements of implanted inclusions from sectioning of the material, and the third is measurements of implanted inclusions that initiated significant cracks in a fatigue test. Each is considered here in turn.

Non-metallic inclusions in powder metallurgy alloys tend to be irregularly shaped although mostly convex. The GRC approach to characterizing defect sizes and shapes employed an idealized ellipsoid model to approximate the defect geometry, whether data resulted from HLS, metallography, or fractography.

Calculation of Anomaly Distributions from Heavy Liquid Separation Data

Several methods have been attempted to separate ceramic inclusions from a base metal powder, including water elutriation, froth flotation, and heavy liquid separation (Roth *et al.*, 1994). The most successful of these methods has been heavy liquid separation (HLS), originally developed by Battelle for Wyman-Gordon, and developed further by GE and Wyman-Gordon for application to nickel-base powder alloys. In order to perform HLS analysis of anomaly sizes, the blended metal powder is mixed with a heavy liquid whose density is less than that of the superalloy powder but greater than the density of the inclusions. Low density ceramic inclusions float to the surface while higher density powder metal will sink. The ceramic inclusions can be separated from the solution and characterized (number and size) using standard visual examination techniques. A major concern with HLS is that the heavy liquid used (thallium malonate-formate solution) is highly toxic and requires careful handling procedures.

The HLS method can generate extensive data on the size and shape of inclusions, and these data can easily be characterized in terms of standard statistical quantities. These inclusions are typically lying on a flat surface when inspected, and so it is easy to identify and measure the largest dimension of the inclusion, as well as the size orthogonal to this dimension in the plane of the flat surface. However, the third dimension of the inclusion (the out-of-plane dimension) is not so easily measured, unless the inclusion is manipulated to present the third dimension to the optical plane.

In earlier GRC investigations of artificial seeds (Kantzios *et al.*, 2003; Bonacuse *et al.*, 2002), when no data were available for the third dimension, it was assumed that the relationship of the third dimension to the second dimension was the same as the relationship of the second dimension to the first dimension (*i.e.*, the mean and standard deviation were a factor of 0.667 times the size of the larger dimension), and it was further assumed that the correlation between the second and third dimensions was the same as between the first and second.

However, GRC subsequently generated data for the third dimension by inclining the tape (to which the seeds were adhered) perpendicular to the original inspection direction (Bonacuse *et al.*, 2006). The resulting data revealed that the assumed scaling of the third dimension (mean and standard deviation reduced by a factor of 0.667 relative to the second dimension) was remarkably accurate. It also revealed, however, that the correlation between the second and third dimensions was completely different than the first and second dimensions; the

third dimension was, in fact, inversely correlated with the second dimension. This was rationalized by noting that the largest size the minimum dimension can achieve is limited by the largest hole in the sieve, and inclusions with smaller third dimensions are more likely to fall through the sieve. Therefore, inclusions with the largest second dimensions are more likely to have smaller third dimensions or they would not have made it through the sieve to begin with.

The specific quantitative observations made by GRC about the relative dimensions of the anomalies are likely limited to the specific seeds used in this study. It is not clear if the qualitative observations are applicable to the broader class of inclusions in powder metal. Further data are needed to determine if this true. It also remains that additional effort would be required in practice to obtain quantitative data on the third dimension of inclusions using the HLS process.

Another inherent limitation of the HLS approach to characterizing inclusion size distributions is that the inclusions are characterized at the powder stage, before the component is forged into its production shape. GRC (Kantzios *et al.*, 2003) found that seed dimensions in forgings (as determined using metallographic sectioning) were significantly different from the original seed dimensions as characterized by HLS data, even after compensating for errors introduced by the sectioning method (discussed in the following section). The differences were attributed to seeds breaking up and the fragments becoming strung out along the extrusion direction during the forging process. The effective aspect ratios of the seeds in the forging were much larger than the aspect ratios of the initial seeds. Similar observations had been made for natural inclusions in an earlier study (Gabb *et al.*, 2000). Kantzos (2006) indicated that Type I inclusions tend to break up more, while Type II inclusions tend to deform more, and that larger inclusions tended to break up more.

Calculation of Anomaly Distributions from Sectioning Data

Because seed or inclusion dimensions can be altered by the forging process, it may be preferable to characterize these dimensions with measurements taken from the final forged shape. This can be done with metallographic sectioning of the forging. Metallographic sections can be taken along different planes (hoop, radial, axial) in order to determine seed dimensions and shapes in each of these planes.

However, this method also has inherent limitations, as Kantzos *et al.* (2003) has pointed out. One limitation is that the metallographic section will not, in general, pass through the maximum dimension of the defect, and so the resulting measurement will underestimate the actual size of the defect by an unknown amount. The distribution based on sectioning and the actual distribution tend to converge at the largest areas. Another limitation is that the same defect cannot be sectioned along three orthogonal planes, and so it is not possible to know the three-dimensional aspect ratio of any single defect.

Ghosn *et al.* (2003) presented a method to address the first limitation by “unfolding” the inclusion size distribution from the metallographic sectioning information. He adapted a published scheme to generate a 3D reconstruction of size distributions from 2D sections using an Expectation Maximization (EM) algorithm. The method is most commonly used for spherical bodies, but Ghosn also obtained equations for the special case of prolate spheroids of constant

shape (a spheroid being an ellipsoid having two equal axes). Ghosn *et al.* demonstrated that the method worked successfully to predict the actual size distribution of spherical shot peen media and -80+100 mesh metal powder from 2D section data; the method was less successful with -270 mesh metal powder. They also applied the same methods to the metallographic images of the largest seeds (fragmented particles) in forgings, documented in more detail by Kantzos *et al.* (2003). Evaluation of success was difficult because the “correct” answer was not known (the original seeds had severely broken up during forging). This method has not been demonstrated for general ellipsoids.

As noted earlier, the forging process can cause significant fragmentation of defects (Kantzios *et al.*, 2003). As a result, the “defect” observed in a metallographic image may in fact be a collection of neighboring defect fragments of varying size, proximity, and orientation. Therefore, GRC geometric models of defects in the forging employing an ellipsoidal form provide only an average shape reflecting the overall result of the forging process. The characteristic length of the major or minor axis of the “ellipse” in the sectioning plane generally represents the span of a collection of neighboring fragments, including some semi-arbitrary criterion for the maximum distance between neighboring particles that should be considered constituents of the same “defect.” In this spirit, the major axis is the longest dimension of this particle collection, and the minor axis is the approximate width of the collection along a direction orthogonal to the major axis.

This method requires metallographic sampling of relatively large areas in order to generate adequate data. The GRC studies of seeded material involved sampling 3500 mm² to 10,000 mm² of surface area (Kantzios *et al.*, 2004), but they noted that much larger areas would have to be sampled for unseeded material due to the significantly lower defect occurrence rates.

Calculation of Anomaly Distributions from Fractography Data

A third possibility (Kantzios *et al.*, 2004) is to determine anomaly distributions from inclusion measurements on the fracture surface itself. These measurements correspond to defects that actually caused fracture, not the general population of all defects in the material. The total number of defects thus characterized would generally be much smaller, which would present additional statistical challenges. Dimensional information on other orthogonal planes is generally not available.

Fractographic approaches do not give any real indication of how many inclusions were present in the tested volume. It is difficult to extrapolate from the extreme defect size distributions obtained from fatigue test coupons to those expected in a turbine rotor or a fleet of turbine rotors.

Kantzios *et al.* (2004) noted from their seeded studies that the size distribution for crack-initiating defects was larger than the initial (HLS) distribution for their seeded material, since fatigue was an extreme process that tended to favor the larger defects in the population. The opposite was true for unseeded (relatively clean) material: the size distribution for the crack-initiating defects was smaller than the initial HLS size distribution. The unseeded material was so clean (inclusions were so rare) that a large inclusion was unlikely to be found in the coupon volume tested even though some large inclusions were present in the original powder.

Comparative Remarks

Kantzos *et al.* (2004) concluded that all three of these methods—HLS, quantitative metallography, and quantitative fractography—were useful and capable of quantifying powder cleanliness to various degrees. They suggested that a combination of all three methods was desirable, although they did not propose any methods for such a combination. The HLS method is the only method that can provide an accurate size distribution as well as the defect occurrence rate. However, the HLS distribution needs to be adjusted in order to take into account the extent of defect fragmentation during forging.

Multiple Anomaly Types

All of these observations and methods are based on the assumption that only one type of defect is causing fatigue failure and therefore needs to be characterized. The cited GRC research did not explicitly address the issue of multiple anomaly types. All work was focused on non-metallic inclusions (and artificial seeds that were intended to emulate these natural inclusions). The seeded specimens always failed from inclusions (seeds).

Earlier GRC work on unseeded U720 did observe multiple failure modes, including some systematic effects that favored one failure mode over another. Gabb *et al.* (2000) performed unseeded U720 tests at 538C (1000°F) and found that strain ratio $R_\epsilon = 0$ tests predominantly (but not always) failed from cracks at elongated clusters of inclusions, while $R_\epsilon = -1$ tests usually failed from cracks emanating from large sheared grains (“grain facet failures”) or at pores, with a few inclusion failures also occurring. The total strain range in the $R_\epsilon = 0$ tests (0.75%) was slightly smaller than the total strain range in the $R_\epsilon = -1$ tests (0.90%). No quantitative treatment of different failure modes was offered.

Later GRC testing (Gabb *et al.*, 2002) at 650C (1200°F), three strain ratios, and a wider variety of strain ranges found that unseeded specimens failed at cracks initiated at two different types of inclusions as well as micropores. Micropore-initiated failures appeared to be rare. Initiation sites tended to be located at or near the surface in tests at high strain ranges and internal for lower strain ranges. Kantzos *et al.* (2004) reported that the unseeded fatigue test coupons failed from inherent inclusions as well as other flaws such as porosity and grain facets. Kantzos (2006) indicated tendencies toward pore failure at lower temperatures and higher strains, and towards inclusion failures at high temperatures and lower strains.

2.1.2 Calculation of Fracture Probability

The second major part of the reliability determination is the calculation of the probability of fracture, given that a defect does exist. This part includes several steps, including the determination of the initial crack size due to the inclusion, the number of fatigue cycles required to form a growing crack at the defect, and the number of fatigue cycles required to grow this crack to failure. The fatigue life can also be influenced by residual stress effects and environmental effects.

Determination of the Initial Crack Size

The size and shape of the crack-initiating inclusion must be translated into the size and shape of the initial fatigue crack in order to perform a fatigue crack growth (FCG) calculation.

Bonacuse *et al.* (2002) originally hypothesized that the inclusion with the largest cross-section orthogonal to the load would be the most likely to initiate a propagating fatigue crack. However, this assumption led to predicted distributions of initial crack area that were consistently smaller than what was revealed on the fracture surfaces. Bonacuse *et al.* (2006) subsequently proposed that the projected area of the inclusion on the plane orthogonal to the load might be a better predictor of the inclusion's crack initiating potential, noting that other researchers had come to the same conclusion.

Since the defects are being modeled as arbitrary ellipsoids, their orientation relative to the load plane is another important factor in determining the size and shape of the resulting fatigue crack. Bonacuse *et al.* (2002) reported that the extrusion and forging processes tend to orient the inclusions along the high strain directions. In forgings, sections taken from orthogonal directions seem to show a preferential orientation in the plane of the forging. Bonacuse *et al.* (2002) elaborated that there was a correlation between the magnitude of the processing strain and the degree of orientation: larger strains lead to more alignment. In addition, larger inclusions seemed to be more likely to orient themselves to the flow direction than smaller inclusions.

Kantzos *et al.* (2003, 2004) provided a more detailed report, presenting detailed forging maps with data indicating that the orientation of the inclusions in the forging was not random, but was correlated with the direction and magnitude of the metal forming strains in the forging process. Both break-up and orientation effects were stronger in the transition and rim regions of their simple disc shapes, where effective forging strains were largest. They speculated that these effects would be more significant in large forgings where the material flow and deformations are appreciably larger than in the pancake forgings used in the GRC study.

Detailed studies of these orientation correlations were not performed, so Bonacuse *et al.* (2006) optimized an assumed correlation to fit the available data. Combining this information with the projected area criterion mentioned earlier, Bonacuse *et al.* (2006) simulations showed reasonable success in predicting the distributions of crack-initiating defect sizes observed in fatigue tests.

Gabb *et al.* (2000) had earlier observed some statistical correlations between smooth specimen fatigue life and original location of the specimen within a complex forging shape for unseeded material, although the correlation coefficients were relatively low. It is not clear if these correlations might have been due to defect issues (perhaps arising from different forging strains at different locations in the forging) or due to base microstructure issues (such as grain size). This question was not addressed in the Gabb *et al.* work.

Most of the failure cracks in the GRC seeded studies initiated at inclusions on the specimen surface. Kantzos *et al.* (2004) reported that surface initiations frequently favored inclusions that were barely sectioned by the surface and whose bulk was mostly contained within the specimen. Internal initiations typically occurred at much larger inclusions than surface initiations.

This was as expected, due to the much larger volume sampled in the interior compared to the surface, and perhaps also because much smaller inclusions in the interior might not initiate growing cracks.

Given that defects are being modeled as arbitrarily oriented ellipsoids with three independent dimensions, and given that the intersection and/or projection of these ellipsoids with sectioning planes, load planes, and external surfaces defines significant area values with direct implications for life prediction, it is useful to be able to calculate these areas quickly and accurately. Bonacuse (2008) has derived a set of mathematical models for these parameters, including the intercepted area of a randomly sectioned ellipsoid, the dimensions and orientation of the intercepted ellipse, the area of a randomly oriented sectioned ellipse, the depth and width of a randomly oriented sectioned ellipse, and the projected area of a randomly oriented ellipsoid. Without these mathematical models, computationally expensive search algorithms would be required to compute these parameters, and this might not be feasible for probabilistic simulations of fatigue life and component reliability.

Calculation of Crack Formation Life

The nature and location of the initiating defect appears to have a significant impact on crack formation life.

Early GRC studies (Gabb *et al.*, 2000) with unseeded test coupons, where 75% of the cracks initiated sub-surface, concluded that most tests spent over 90% of life in the initiation phase (including both pores and inclusions). These estimates did not consider the possibility of slower FCG rates for embedded crack (in the absence of environmental effects), as discussed further below. This might mean that the formation life fraction was smaller than originally inferred.

More recent GRC seeding studies (Kantzos *et al.*, 2004), where most failures were initiated at the surface, observed little or no formation life for surface-connected inclusions. Crack formation at subsurface locations was not studied in detail in this work. In these seeded tests, the tendency for surface initiation was stronger at lower strain ranges and higher R ratios.

Gabb *et al.* (2002) found that prior exposure at elevated temperatures for extended periods of time shifted the failure locations from internal to surface, due to environmental attack on the surface. An increase in total scatter was attributed to the competing failure modes: internal initiations at inclusions or large grains (longer lives), or surface initiations at an environment-affected surface layer (shorter lives). Proper analysis required identifying and separating these two modes.

GRC has not proposed any general physics-based models to predict crack formation life as a function of defect size and shape, temperature, strain range, and mean stress. Gabb *et al.* (2003) developed a non-linear regression model describing the relationship between total fatigue test life and a combination of test control parameters (strain range and strain ratio) and defect characteristics (mean log inclusion areas and inclusion area densities) for a specific set of test results. However, this model did not differentiate between crack formation life and crack growth life.

Because crack formation life has not been isolated from crack growth life in GRC analyses, no explicit attention has been given to scatter in crack formation life.

Detailed studies of specimen surfaces using a special rotational stage in the scanning electron microscope (Telesman *et al.*, 2002, 2006) revealed that cracks were initiated at nearly all surface-breaking defects being monitored. However, not all initiated cracks grew to failure. The cracks that did grow to failure often formed at defects with mapped surface sizes that were actually smaller than the average of all monitored inclusions. This was interpreted as evidence of an “iceberg” effect: the most deleterious inclusions may be surface-breaking inclusions with much larger dimensions beneath the surface, as noted also by Kantzos *et al.* (2004).

Calculation of Crack Growth Life

The calculation of FCG life is a critical step in prediction of total fatigue life, particularly for situations where crack formation life is negligible. Because inclusions can be very small, the early growth of fatigue cracks formed at defects falls into the “small-crack” regime. One of the key issues is whether the growth of small cracks near defects follows the general trends of conventional long-crack growth behavior, or exhibits classical “small-crack” effects.

Telesman *et al.* (2006, 2007) showed crack growth data that, at first, appeared to exhibit classical small-crack effects: increased scatter, accelerated growth rates relative to the extrapolated Paris line, and growth at nominal ΔK values below the large-crack threshold. However, much of this behavior was characterized as “pop-in”: cracks appeared very quickly, but exhibited decreasing da/dN values and often arrested completely. No quantitative models were proposed by GRC for pop-in behavior, but machining residual stresses, crack closure, localized residual stresses due to coefficient of thermal expansion mismatch, or highly localized stress concentrations due to irregularly shaped inclusions (Kantzos *et al.*, 2004) were offered as potential explanations.

When Telesman *et al.* screened out this crack growth during the first 250 cycles, some of the apparent “small-crack” trends in the data vanished. The remaining data often agreed with the large-crack Paris line. However, some data still fell below the large-crack threshold, and some data (especially at $R \sim 0$) exhibited slightly faster growth than the Paris line. It was speculated that this might be due to reduced crack closure, since FCG rates were still bounded by high- R large-crack trend lines. Further study of the data is needed to determine how well the small-crack behavior is described by large-crack models.

As noted earlier, Telesman *et al.* (2002, 2007) and Kantzos *et al.* (2004) reported that most monitored inclusions initiated cracks for all test conditions, but only a few cracks grew to failure. It is not clear why some cracks arrest and some grow. The relative fraction of active inclusions was higher at higher strain ranges and higher R -ratios.

Relatively little attention was given to large-crack growth, aside from the generation of basic property data. Telesman *et al.* (2006) used a Walker model to correlate 1200°F long-crack FCG data generated with Kb -bar (surface crack) specimens at four negative and three positive R -ratios. Different Walker exponents were used at positive vs. negative stress ratios. Data were only shown at $R = 0.05, 0.5, -0.25,$ and -1 . No attention was given to scatter in large crack growth rates, since this is not usually a significant source of variability in this problem.

Bonacuse *et al.* (2003) reported a life prediction study based on simulations of inclusions with random size and shape distributions. Predicted seed maps (including orientation and intercepted surface areas) generally agreed with experimental observations. Fatigue life was calculated based on fatigue crack growth with no threshold or initiation considerations. The ten largest surface connected inclusions and all embedded inclusions in the simulated specimens were considered, with the lowest calculated life assumed to give the specimen life. Room temperature air FCG properties were used for embedded cracks, while elevated temperature air properties were used for surface cracks (see remarks below about environmental effects). The simulations exhibited mixed success in predicting observed behavior: conservative in some cases, non-conservative in others, and generally underestimating the observed life scatter.

Predictions of FCG lives for the seeded tests (for both surface and internal cracks) based on large crack growth rate models (assuming negligible crack formation life, and taking the size of the defect where the failure crack originated as the initial crack size) met with mixed success in work reported by Telesman *et al.* (2006). Predictions were reasonably accurate in some cases (especially for some larger seeds at $R = 0$), but very conservative in other cases. These calculations did not address small-crack behavior (including pop-in, decreasing da/dN , or crack arrest), machining residual stresses, or environmental effects. These latter two effects are discussed in subsequent sections.

Ghosn *et al.* (2005) documented some statistical analysis of the FCG data and used the analysis to perform a Monte Carlo simulation study. The number and size of the inclusions in each simulated bar was randomly generated from appropriate distributions. They lumped small-crack and large-crack data together and used simple linear Paris relationships to model the data. They developed empirical equations to describe the percentages of cracks with zero or negative growth as a function of the maximum stress. They also developed statistical expressions for the deviations from the Paris line, which were larger at smaller Walker-corrected ΔK values (consistent with smaller crack sizes). They presented an error analysis to claim that measurement errors were not a significant source of uncertainty. The simulations were generally successful at reproducing the overall trends in the observed life behavior, although some details were not satisfactorily predicted.

Residual Stress Effects

GRC has given considerable attention to surface residual stress effects in P/M alloys, but has not studied bulk residual stress effects (arising, for example, from forging or heat treating).

Effects of Residual Stress on Fatigue Life

Telesman *et al.* (2007) observed surface crack initiation very early in low-cycle fatigue (LCF) life at 1200°F, $R = 0$, and various strain ranges, for both as-machined and one shot-peened condition. Since the significant compressive residual stress induced by the shot peening (SP) did not delay surface crack initiation, but did increase total life for some test conditions, they concluded that residual stress affects crack growth rates, but not crack formation lifetimes.

Barrie *et al.* (2008) studied the effects of SP on fatigue behavior at 427C and 650C for multiple strain ranges from 0.6% to 1.2% and for strain ratios of -1, 0, and 0.5. An initial screening study of different SP conditions found that all SP conditions considered significantly improved life for the 54 μm seeded material, by shifting the failure from surface to interior. However, only SP to high intensity resulted in fatigue life improvement for the 122 μm seeded material, probably because the depth of the residual compressive stress was on the same order as the seed sizes.

Further studies by Barrie *et al.* (2008) with the selected high intensity/low coverage SP conditions (8A/200%) found some improvements in fatigue life at low strain ranges and low strain ratios. However, no improvements were observed at $R_e = 0.5$ or larger strain ranges. The larger strain ranges were observed to cause significant residual stress relaxation during the test. No explanation was given for the lack of effect at high strain ratio, but this would be consistent with a FCG explanation since the high R values would counteract some of the effects of the compressive residual stress from a crack closure standpoint. Barrie *et al.* did not study initiation or growth phases separately.

Relaxation of Residual Stresses

Residual stresses induced by shot peening or other surface enhancement methods can relax during thermal exposure and/or fatigue cycling.

Gabb *et al.* (2004) investigated thermal exposure effects in retired T700 disks manufactured from P/M alloy René 95. Residual stresses were measured in the as-received (full lifetime) disks, and then following thermal exposure at 593°C, 650°C, and 704°C for 1 hr, 24 hr, and 500 hr. Significant relaxation occurred. An empirical regression model was developed to describe the effects of T , t , initial cold work, and initial residual stress on stress relaxation and cold work relaxation. Stress relaxation was accentuated for combinations of high temperature with long time, as well as combinations of high initial compressive residual stress with high temperature, time, or initial cold work. The equations are not quantitatively predictive for other materials or conditions. Limited tensile specimen testing of mechanical stress relaxation with time and temperature found qualitatively similar trends, but no quantitative correlations were established.

Telesman *et al.* (2007) presented limited data on measurements of shot peening (8A, 200%) residual stress on specimens before and after LCF testing at 1200°F (650C), $R = 0$, $\Delta\varepsilon = 0.8\%$. Significant residual stress relaxation occurred. Another limited data set showed nearly complete relaxation of low plasticity burnishing (LPB) residual stress following LCF testing at 1200°F, $R = 0.5$, and $\Delta\varepsilon = 0.8\%$, although the conditions were cited as being “overly aggressive” to evaluate the effect of LPB on LCF life. One data set showed significant relaxation of LPB residual stress following 17 hrs at 1200°F (no fatigue cycling), suggesting that the relaxation observed in the LCF tests may have been primarily due to thermal mechanisms. LCF lifetimes with LPB were similar to untreated lifetimes. No models for residual stress relaxation were proposed.

Kantzos (2006) has presented data showing the effect of LCF cycling at 1200°F, $R = 0$, $\Delta\varepsilon = 0.8\%$ on SP residual stress for four different shot peening intensity-coverage combinations. All four conditions exhibited significant relaxation. No models were proposed.

Machining Residual Stresses

Telesman *et al.* (2002, 2006) speculated that low stress grind machining residual stresses (which are compressive on the surface) might be related to observed microcrack behavior (decreasing crack growth rates and crack arrest), although no specific mechanisms were proposed. Simple predictions (neglecting residual stresses) of surface crack growth rates at $R = 0$, $\Delta\varepsilon = 0.6\%$ significantly ($10\times$) overpredicted observed crack growth rates, but agreement was good at $\Delta\varepsilon = 0.8\%$. Telesman *et al.* (2002) noted that the higher strain ranges created enough plasticity to wash out the shallow machining residual stresses. Limited measurements of surface and near-surface residual stresses showed some relaxation in initial (machining-induced) residual stresses after only 250 LCF cycles. Limited test data were also presented showing that a single 1% overload increased the FCG rate and decreased the fatigue life for specimens with large (T64) defects. It was speculated that this effect might be due to residual stress reduction, but also perhaps due to potential inclusion debonding. Single 1.2% overloads did not affect the fatigue life for specimens with smaller 54 μm inclusions. Another group of specimens was electropolished to remove residual stresses, but the electropolishing (EP) step also preferentially removed matrix material surrounding the inclusions. The EP step resulted in a significant reduction in LCF life (but with a smaller number of inclusions initiating cracks). Another series of tests with thermal exposure in vacuum to reduce residual stress also reduced the fatigue life.

Environmental Effects

As noted earlier, Gabb *et al.* (2002) observed that prior exposure of unseeded fatigue specimens to elevated temperatures (650°C to 705°C) for extended periods of time (100 hr to over 1000 hr) caused a significant reduction in total fatigue life (up to 70 percent) and increased the scatter in life compared to unexposed levels. Fatigue tests were conducted at 650°C. The differences were attributed to a shift in failure mode from subsurface to surface initiation due to environmental attack on the surface (*i.e.*, a significant decrease in surface initiation life due to environmental effects, not related to surface inclusions). Unexposed fatigue tests at 704°C and a 650°C fatigue test with a 1 minute cyclic dwell period also exhibited surface failure modes consistent with the exposed tests.

Telesman *et al.* (2006) noted that proper modeling of subsurface crack growth required crack growth models for vacuum conditions (in the absence of environmental effects). A survey of the literature found only isolated vacuum FCG data (Paris regime) at high temperature (600°C and 700°C), but these data generally agreed with available room temperature air data (FCG rates were generally slower than elevated temperature air data). The possibility of using room temperature air data to model surface cracks was suggested.

2.2 A Summary of Current DARWIN Capabilities Relevant to P/M Lifting

SwRI has been actively developing technology and software to support probabilistic damage tolerance analysis of gas turbine engine rotors since 1995. One of the key outcomes of this work has been the DARWIN (Design Assessment of Reliability With INspection) computer code (Millwater *et al.*, 2000; Leverant *et al.*, 2004; McClung *et al.*, 2004a; McClung *et al.*, 2009). DARWIN integrates finite element models and stress analysis results, fracture mechanics models, material anomaly data, probability of anomaly detection, and uncertain inspection schedules with a user-friendly graphical user interface (GUI) to determine the probability-of-fracture of a high-energy rotating component as a function of operating cycles with and without inspections.

The SwRI work was originally motivated by an uncontained rotor fracture incident at Sioux City, Iowa, in 1989. As a result of this incident, the Federal Aviation Administration (FAA) requested that the aircraft engine industry, through the Aerospace Industries Association (AIA) Rotor Integrity Sub-Committee (RISC), review available techniques to determine whether a damage tolerance approach could be introduced to produce a reduction in the rate of uncontained rotor events. During the development of this probabilistic damage tolerance approach, it became apparent to RISC that the capabilities and effectiveness of the emerging technology could be significantly enhanced by further research and development. SwRI, in partnership with four major U.S. engine manufacturers and with guidance from RISC, proposed and was awarded a series of FAA grants beginning in 1995 to address identified shortfalls in technology and data.

Initial DARWIN capabilities were focused on the hard alpha titanium problem, which had caused the Sioux City incident. A general framework was established to address inherent material defects that could occur anywhere in an axisymmetric body, as described by a 2D finite element model. Another notable uncontained rotor incident in Pensacola, Florida, in 1996, was caused by surface damage at machined circular holes, and as a result, a second thrust of DARWIN development emerged. A second general framework was established to address induced material defects arising during manufacturing or maintenance processes, focusing on damage occurring at the component surface, and incorporating 3D finite element models.

With direct guidance from the FAA and the OEM Steering Committee, DARWIN has been tailored to address specific advisory circulars issued by the FAA, including AC 33.14-1 for titanium hard alpha, AC 33.70-2 on circular holes in all materials, and the more general AC 33.70-1 for damage tolerance of all engine life-limited parts. The FAA has indicated that DARWIN is an acceptable means of compliance with these advisory circulars, and DARWIN has been employed in the formal FAA certification process for numerous engines.

The FAA also directed that some basic DARWIN capabilities be developed to address superalloys with high anomaly occurrence rates, including powder metallurgy alloys. Some capabilities have already been implemented in DARWIN, although this work has been limited due to other, more pressing FAA and RISC priorities.

The purpose of this document is to summarize the existing capabilities in DARWIN that are relevant to the P/M lifing problem. The document follows the general outline of the summary of research in P/M lifing conducted at NASA Glenn Research Center.

2.2.1 Determination of Anomaly Distributions

DARWIN currently has no capability to derive or generate anomaly distributions. A limited number of distributions are provided in a special DARWIN library for specific anomaly types: hard alpha titanium anomalies (as a function of material vintage and billet/forging inspection sensitivity), and surface damage at machined circular holes. The user has the option of providing additional anomaly distributions as files in predetermined formats that DARWIN can read. The user cannot modify these distributions inside DARWIN itself.

For hard alpha titanium, the anomalies are assumed to have a spherical shape. The probability distribution of these anomalies is described in a two column format consisting of anomaly area and associated number of anomalies (exceedance format). For general materials such as P/M alloys, the anomalies are assumed to have an ellipsoidal shape. The probability distribution of these anomalies is based on the ellipsoid major axis (exceedance format), anomaly aspect ratios (normal or lognormal distributions), and three anomaly orientation angles (uniform or normal distributions).

2.2.2 Calculation of Fracture Probability

Determination of the Initial Crack Size

For titanium alloys with hard alpha anomalies, the initial crack dimensions are based on the anomaly area described in the anomaly distribution. The anomaly area is converted to crack dimensions assuming that the initial crack has a circular shape for embedded cracks, a half-circular shape for surface cracks, and a quarter-circular shape for corner cracks. For general materials, the initial crack dimensions are based on either the intersection or projection of the 3D anomaly with the fracture plane. Similar as for titanium hard alpha, the anomaly dimensions are adjusted when the crack is located near a surface or corner of a component. In addition, an initial or “production” inspection can be applied to general materials to remove components with anomalies that are detected prior to placement in service (this inspection cannot be applied to titanium materials, because the anomaly distributions for these materials were calibrated to components that had already been placed in service).

Calculation of Crack Formation Life

DARWIN has no built-in models to calculate the cycles required to form a fatigue crack at a material anomaly. However, DARWIN does facilitate user-provided crack formation models. A Crack Formation Module is provided that allows users to link their own specific crack formation algorithms with DARWIN, as shown in Figure 1. The Crack Formation Module and associated data are developed and maintained by the individual user. During run time, DARWIN communicates with the Crack Formation Module to obtain the crack formation life associated with an anomaly having specified temperature and applied stress values.

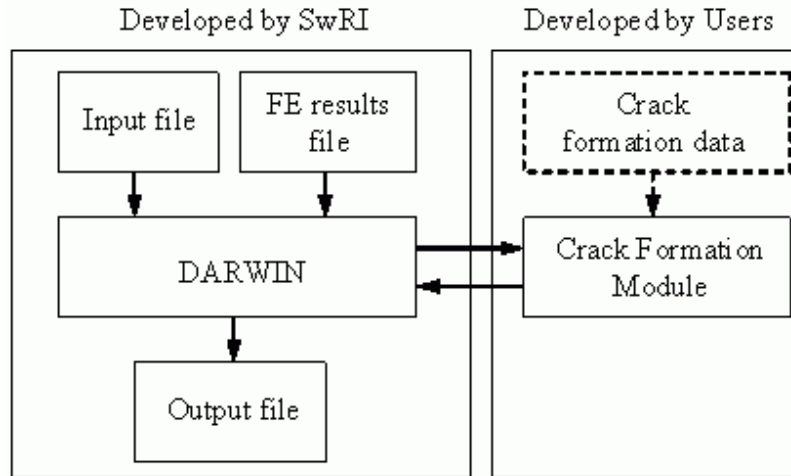


Figure 1. Crack formation computations are performed via a user-supplied crack formation module.

The Crack Formation Module is executed as a separate program that receives input from DARWIN. The following data are currently passed from DARWIN to the Crack Formation Module: global coordinates (r , z , θ), distance to the nearest free surface of the fracture mechanics plate, size of anomaly (a , c) in crack plane and orientation of plane, six components of stress at the anomaly location for each load pair, relaxed stresses (if shakedown is performed in DARWIN), and temperature at the anomaly location for each stress pair. The maximum temperature of each stress pair is provided to the formation module, and the crack plane is limited to hoop, axial, and radial stress planes. These data are used by the Crack Formation Module for crack formation life prediction. The following data are passed from the Crack Formation Module to DARWIN: crack formation life for entire load history, and crack size at end of crack formation life (a , c).

Linking two independent computer programs together is a nontrivial task, particularly when multiple platforms and associated operating systems must be supported. The approach used is to create a third program that is linked separately with the other two programs. A formation Application Program Interface (API) was developed for this purpose, in which DARWIN and the Formation API are compiled as stand-alone programs. The Crack Formation Module is also compiled as a stand-alone program. During run time, data is passed between DARWIN and the Crack Formation Module via the Formation API. This approach does not require the sharing of source code, nor does it require the creation of ASCII files to pass data. In the future, the interface between DARWIN and the Crack Formation Module can easily be expanded to include additional variables associated with enhanced crack formation life models.

Calculation of Crack Growth Life

DARWIN has a comprehensive capability for fatigue crack growth analysis. The Flight_Life fracture mechanics module contains libraries of stress intensity factor (SIF) solutions and multiple models for FCG rate calculations. SIF solutions include original univariant and/or bivariant weight function solutions for elliptical embedded cracks, semi-elliptical surface cracks,

quarter-elliptical corner cracks, and straight through cracks in plates or at holes (Enright *et al.* 2003; McClung *et al.*, 2004b; Lee *et al.*, 2008). Available crack growth equations include Paris, bilinear Paris, sigmoidal, hyperbolic sine, and the NASGRO 4.0 equation, as well as general capabilities to accommodate tabular data. Available mean stress models include Walker and closure models, as well as Walker interpolation. Interpolation of crack growth rates at different temperatures is also available. Scatter or uncertainty in calculated FCG rates is described by a life scatter factor (a log-normal distribution with a user-specified coefficient of variation) that is uniformly applied at all crack sizes.

DARWIN currently has no explicit treatment of small-crack behavior, except that the standard NASGRO crack growth equation in DARWIN does include a size-dependent threshold term that reduces ΔK_{th} at very small crack sizes, following the El Haddad functional form. Some investigations of alternative small-crack formulations are underway at SwRI in the current FAA grant, and this could potentially lead to a new small-crack model being implemented in DARWIN.

Static and fatigue testing of coupons with either artificial or natural hard alpha defects gave results indicating the potential influence of local residual stresses on fracture behavior (McKeighan *et al.*, 2001). Experimental measurements of the coefficient of thermal expansion of the hard alpha (titanium nitride) inclusion and the base titanium alloy indicated a large enough difference to induce significant local residual stresses under some conditions (Laz *et al.*, 2003). Idealized models were developed to estimate these residual stress fields and their effect on crack initiation and growth behavior, and they agreed satisfactorily with the observed cracking. These models have not been implemented in DARWIN, however.

Residual Stress Effects

DARWIN currently has a basic capability to superimpose a user-provided tabular residual stress gradient with the 2D finite element model stress results. The resulting combined stress gradient is used to calculate ΔK and R ; the superposition of the residual stress does not change ΔK but it does change R , which will change the predicted FCG rate. Special optimum point spacing algorithms facilitate the accurate and efficient superposition of stress gradients with significantly different length scales.

This capability is currently limited to semi-elliptical surface cracks with univariant stress gradients in 2D axisymmetric models. Work is planned under the current FAA grant to extend the superposition capability to some additional crack types and also to 3D finite element models.

DARWIN currently has no capability to calculate relaxation or redistribution of residual stresses due to thermal exposure, mechanical loading, fatigue cycling, or crack growth, and no facilities are provided to allow the user to update the residual stress inputs as cycling proceeds. A comprehensive literature review of this topic was conducted under one of the FAA grants and has been published (McClung, 2007).

Environmental Effects

DARWIN currently permits the user to supply different crack growth properties (even different crack growth equation types) for embedded cracks versus all other crack types (which are all surface-breaking). This was specifically designed to facilitate the specification of properties obtained under vacuum conditions for embedded cracks, while other crack types would use customary air properties.

The earlier FAA grants led by SwRI also generated fatigue crack growth properties under appropriate vacuum conditions at relevant temperatures for several selected rotor alloys, both titanium and nickel-based superalloys (McClung *et al.*, 1999). This effort included the generation of vacuum FCG properties for U720 using material provided by NASA GRC (material identical to that used in the GRC studies of P/M lifing). U720 data were generated using Kb-bar (surface crack) specimens at 800°F for $R = 0.05$ and $R = 0.5$. These data have been provided to GRC, but they have not yet been published.

DARWIN includes the ability to extract from finite element models not only the full stress tensor throughout the model, but also the temperature distributions at each time point. DARWIN also permits the user to provide different crack growth properties at different temperatures. During complex thermal-mechanical cycling, DARWIN currently calculates FCG rates using the properties at the temperature corresponding to the time point at which the maximum stress in that particular load pair (cycle) occurs, performing temperature interpolation as needed. Work is underway in the current FAA grant to implement new capabilities for time-dependent crack growth (*e.g.*, fatigue cycling with dwell periods) as well as more advanced thermal-mechanical fatigue crack growth algorithms.

Reliability Calculations

Anomalies in gas turbine engine materials can lead to fracture. The fracture event is dependent on (1) the presence of an anomaly, and (2) the formation and growth of a crack that exceeds the fracture toughness of the material before the design life has been reached. The occurrence probability of an anomaly $P(d_j)$ can be measured by counting the number of anomalies of various sizes on the surface or within the volume of a component. $P(d_j)$ is typically modeled as a Poisson point process (Roth, 1998; Haldar and Mahadevan, 2000):

$$P(d_j) = \frac{(\lambda_i V_i)^j}{j!} \exp(-\lambda_i V_i) \quad (1)$$

The likelihood of fracture failure can be estimated using fatigue crack growth modeling. Since this value is dependent on the presence of an anomaly of a specified initial size, it is commonly expressed as a conditional probability $P(F|d)$, the probability of fracture given that an anomaly is present. $P(F|d)$ is dependent on a number of random variables related to the applied stress values and the fatigue nucleation and growth processes (Wu *et al.*, 2002).

The occurrence of an anomaly in a component is a relatively rare event for some materials, such as hard alpha in titanium (Aerospace Industries Association Rotor Integrity Subcommittee, 1997; Leverant *et al.*, 2003). For these materials, the probability of more than one anomaly is assumed to be negligible (Wu *et al.*, 2002). The probability of fracture at a specified location p_i is therefore based on the occurrence of a single rare anomaly $P(d_1)$ and the probability of fracture at location i given that a single anomaly is present $P(F_i|d_1)$:

$$p_i = P(F_i|d_1)P(d_1) \quad (2)$$

On the other hand, components made from some rotor-grade alloy materials (including P/M alloys) may contain hundreds or even thousands of anomalies. For these multiple anomaly materials, the conditional probability $P(F|d)$ is dependent on the number of anomalies present, and is expressed as $P(F_i|d_j)$. Since cracks can form at the location of any anomaly, the failure of the component can be considered as a weakest-link (series) system consisting of the fracture failure associated with each discrete number of anomalies. For conservative risk estimates, $P(F_i|d_j)$ is set to the maximum probability of fracture associated with any one of the j anomalies present. The resulting system model is expressed as (Enright and Huysse, 2006):

$$P(F_i|d_j) = 1 - [1 - P(F_i|d_1)]^j \quad (3)$$

The influence of the number of anomalies j on $P(F_i|d_j)$ is illustrated conceptually in Figure 2. The anomaly occurrence probability is also influenced by the number of anomalies in a component. This relationship is reflected in the Poisson model of Eqn. (1). The dependence of $P(F_i|d_j)$ and $P(d_j)$ on the number of anomalies j is shown conceptually in Figure 3. The members in Figure 3 represent the discrete number of anomalies that could be present in a given component which are events that have a mutually exclusive relationship (*i.e.*, it is not possible for a selected component to have only two anomalies and only three anomalies simultaneously). p_i is equal to the sum of the failure probabilities associated with each discrete number of anomalies (Hoyland and Rausand, 1994). To obtain p_i , Eqns. (1) and (3) are substituted into Eqn. (2) for each member and summed over the total number of members:

$$p_i = \sum_{j=1}^n \left[\left\{ 1 - [1 - P(F_i|d_1)]^j \right\} \cdot \frac{(\lambda_i V_i)^j}{j!} \exp(-\lambda_i V_i) \right] \quad (4)$$

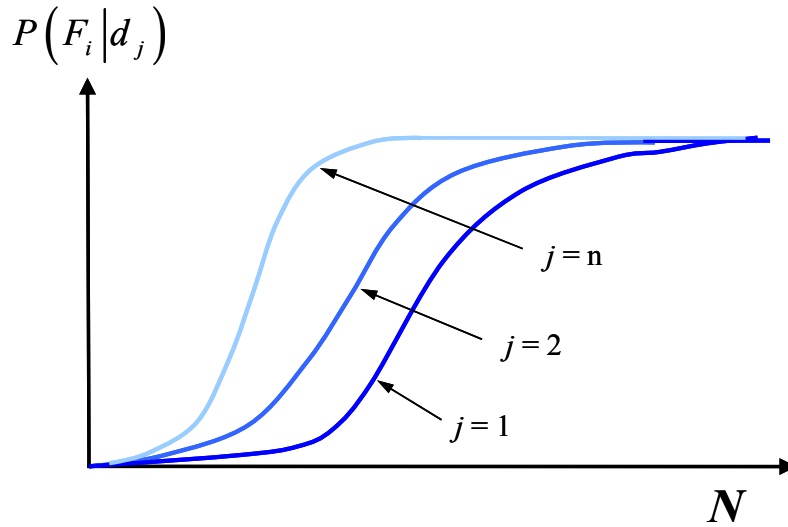


Figure 2. The conditional probability of fracture failure $P(F|d)$ of multiple anomaly materials is dependent on the number of anomalies j at a specified location in the component.

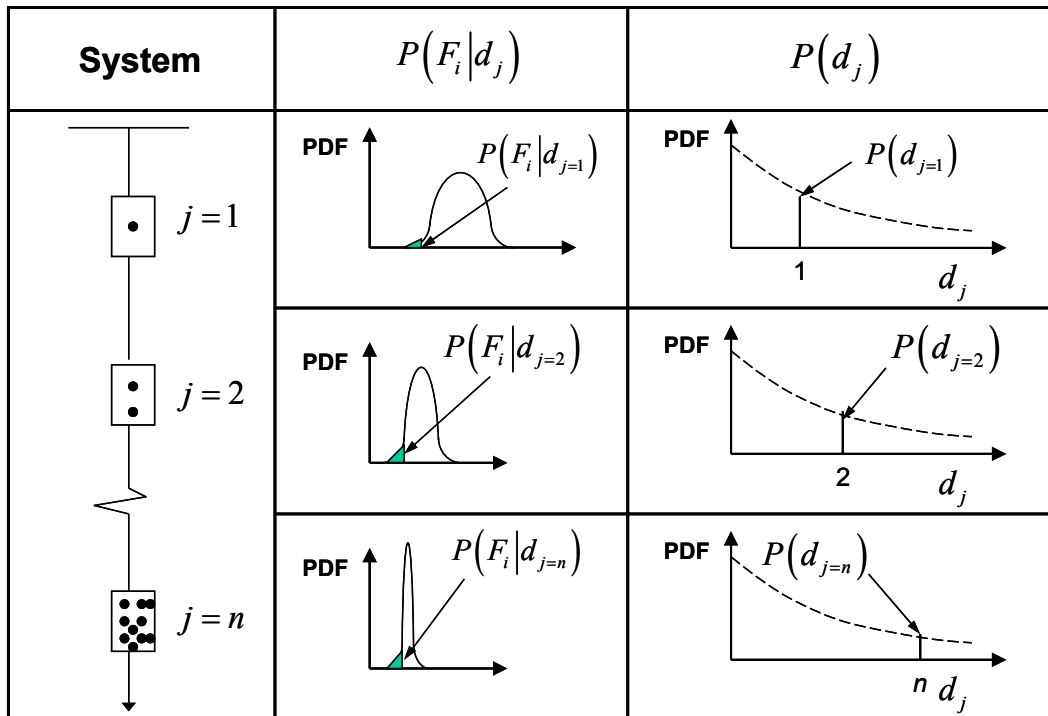


Figure 3. For multiple anomaly materials, both the probability of fracture given an anomaly $P(F_i | d_j)$ and the anomaly occurrence probability $P(d_i)$ are dependent on the number of anomalies present.

Eqn. (4) requires specification of the number of anomalies n . It is shown in Enright *et al.* (2005) that Eqn. (4) reduces to:

$$p_i = 1 - \exp\left[-\lambda_i V_i \cdot P(F_i | d_1)\right] \quad (5)$$

Note that Eqn. (5) is based on the average number of anomalies present at location i ($\lambda_i V_i$).

The probability of fracture is also dependent on the location of an anomaly within a component. The component is often discretized into a number of subregions called zones, and the probability of fracture is assessed for anomalies located within each zone (McClung *et al.*, 2004a). Since component failure occurs when there is a failure within any zone, the component is modeled as a series system of zones with a probability of fracture that can be expressed as:

$$p_F = P[F_1 \cup F_2 \cup \dots \cup F_m] = 1 - \prod_{i=1}^m (1 - p_i) \quad (6)$$

If multiple anomalies are present in each zone, p_i can be estimated for each zone using Eqn. (5). Substitution of Eqn. (5) into Eqn. (6) yields the following expression for multiple anomalies at multiple locations (Enright and Huyse, 2006):

$$p_F = 1 - \prod_{i=1}^m \exp\left[-\lambda_i V_i \cdot P(F_i | d_1)\right] \quad (7)$$

Multiple anomaly types may also be present in one or more regions of a component. The multiple anomaly types can be modeled as additional members of the series system of zones. This is illustrated conceptually in Figure 4, where it is shown that components with multiple anomaly types and locations can be modeled using several nested series systems to represent the relationship among the various failure events.

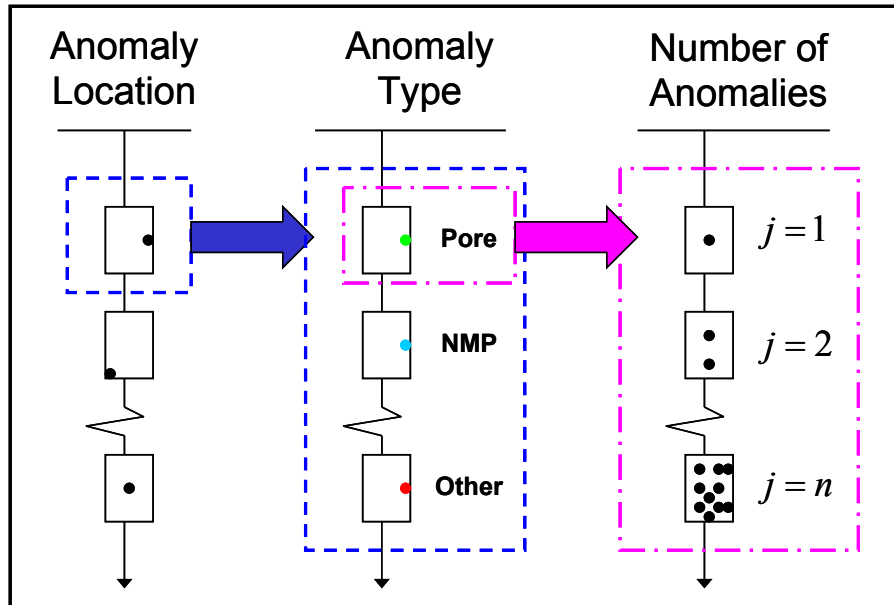


Figure 4. For components with multiple anomalies of multiple types at multiple locations, the probability of failure can be modeled using several nested series systems to represent the various failure events.

Several sampling-based probabilistic analysis methods are used in DARWIN to predict the life of disks subjected to periodic inspection. Monte Carlo simulation provides accurate results (the accuracy is dependent on the failure probability, confidence interval, and number of random samples) but is relatively inefficient because the failure limit state must be evaluated for each random sample using a fatigue crack growth algorithm. A method called a life approximation function (LAF) creates deterministic life and grown area arrays for a family of initial anomalies. During Monte Carlo simulation, the failure limit state is evaluated for each random sample using values interpolated from the deterministic arrays, thereby improving computational efficiency. Another method referred to as importance sampling (IS) focuses analysis on the initial conditions (anomaly size and other random variables) that would result in lives shorter than the specified design life. This approach reduces the size of the analysis region and is significantly more efficient than Monte Carlo simulation. However, it is currently limited to 2D anomalies and does not provide treatment for crack formation life.

Previous DARWIN versions required the user to specify the dimensions and orientation of the fracture mechanics model (rectangular plate) that is superimposed on the finite element model geometry. To reduce the bias introduced by individual users, an automated fracture model called “auto-plate” was recently developed that automatically identifies the optimum dimensions and orientation of the fracture mechanics model at a user-specified location. A new feature to display life contours for 2D axisymmetric finite element models was also recently developed that automatically places an anomaly at each of the nodes in the finite element model, generates a fracture model at each anomaly location, and computes the fatigue crack growth (FCG) lifetime at each location. The resulting family of calculated life results is displayed in the GUI using conventional contouring methods. Future development will be focused on automatic generation of fracture risk contours based on the recently developed auto-plate and life contours capabilities.

3.0 ALGORITHM DEVELOPMENT

The critical reviews of accomplishments and existing capabilities in the GRC methods/models and the SwRI DARWIN software identified a number of significant technology gaps. Addressing all of these technology gaps was always understood to be well beyond the scope of this initial effort. Instead, the primary intended outcome of this initial effort was the development of a program plan for further research, and that program plan is provided in the later Section 4.0. However, it was possible to perform some new algorithm development under the current project, and the results of these activities are documented in the following subsections.

New algorithm development was conducted in three areas. First, a methodology for estimating anomaly distributions for materials in which multiple anomaly types are operative was developed and verified. Second, an unfolding algorithm to estimate the dimensions and orientations of 3D spheroids based on 2D sectioning measurements was implemented and investigated. Third, the behavior of small fatigue cracks in U720 tests conducted by GRC was investigated, and an existing model to predict this small-crack behavior from large-crack growth rates was evaluated.

3.1 Algorithms for Multiple Anomaly Types

3.1.1 Introduction

As noted earlier in the Status Summary section, all of the GRC work developing methods to determine anomaly distributions was based on the assumption that only one type of defect is causing fatigue failure. However, other GRC investigations with unseeded U720 specimens did observe multiple failure modes due to multiple anomaly types, including inclusions and pores. Therefore, in order to address this technology gap, additional work was undertaken under the current project to develop methods for generating anomaly distributions when multiple anomaly types are operative.

Prior to the current project, SwRI performed work for the Air Force Research Laboratory (AFRL) investigating multiple fatigue failure modes in a representative nickel-based superalloy, IN-100 (McClung and Enright, 2009). As part of this work for AFRL, SwRI developed a preliminary method to treat multiple anomaly types. However, this preliminary method had several limitations. Under the current project, SwRI conducted additional research to develop a more rigorous treatment, using the IN-100 data from the AFRL effort to demonstrate the new method. That new work is described in this section.

The probability of failure of a component with multiple anomaly types can be predicted using established system reliability methods provided that the failure probabilities associated with individual anomaly types are known (Thoft-Christensen and Murotsu, 1986; Hoyland and Rausand, 1994; Enright and Frangopol, 1998; Melchers, 1999; Enright and Huyse, 2006). If test data are available for components containing a single anomaly of a single type, they can be used to construct probability density function distributions (PDFs) describing the likelihood of fatigue failure versus flight cycles. These PDFs can be transformed to predict PDFs of components containing more than one anomaly of a single type by considering each of the anomalies as a

single member of a series system of anomalies. If a material contains more than one type of anomaly, it is usually impractical (if not impossible) to prepare test specimens with a single type of naturally occurring anomaly. When the test specimens contain multiple types of anomalies, it may be difficult to accurately estimate the failure probabilities associated with the individual anomaly types, even when component failures can be traced to individual anomaly types. This is due to the potential overlap among failure of different anomaly types that is not captured by system-level testing, the so-called problem of competing risks.

One of the primary challenges associated with modeling materials with multiple types of anomalies is that the test specimens typically contain multiple types of anomalies. If the lives associated with individual anomaly types cannot be characterized from the test data, then it becomes impossible to develop nucleation and growth models for each anomaly type that are required for the system reliability models. A review of failure data for a nickel-based superalloy provided by the Air Force Research Laboratory (Jha *et al.*, 2008) revealed that the overlap among the failure modes for various anomaly types and locations can be significant for some engine materials (the extent of this overlap is presented later in this section). Since all of the life models are eventually based on test specimen data, and test specimens for this class of materials commonly contain multiple types of anomalies, it became essential to identify and demonstrate a method to accurately quantify the lives associated with individual anomaly types.

If the failures of different anomaly types are independent and sufficient failure data are available, the marginal cumulative distribution functions (CDFs) associated with them can be estimated using nonparametric statistical models such as Kaplan-Meier (1958), Nelson (1972), and Aalan (1978), among others. The Kaplan-Meier approach is most commonly used. It is based on the widely accepted theorem of conditional probability (Ang and Tang, 1975), and is even included in some statistical software. When derived in maximum likelihood estimator format, it can be expressed as an asymptotic normal distribution with quantifiable confidence bounds (Hoyland and Rausand, 1994). It is restricted to systems with independent failure modes, an assumption that may be difficult to test in practice (Pepe and Mori, 1993). However, this may become less of an issue as new methods emerge for assessing the dependence among failure modes (*e.g.*, Crowder, 1997). Some researchers have noted that in some cases it may lead to overly conservative risk estimates when the survivability estimates are converted to CDF predictions (Gaynor *et al.*, 1993).

It is well known that correlation among failure modes can have a substantial influence on system reliability predictions (Thoft-Christensen and Murotsu, 1986; Enright and Frangopol, 1998; Melchers, 1999). Researchers have reported that failure mode correlation also can have a substantial influence on survival function estimates for the problem of competing risks (Peterson, 1976; Crowder, 1991). To quantify the extent of this influence, several models have been developed that establish the upper and lower bounds associated with the range of correlation among the failure modes (Peterson, 1976; Slud and Rubinstein, 1983; Klein and Moeschberger, 1988; Zheng and Klein, 1995). In addition, many new models are emerging for the prediction of the marginal failure densities that are not restricted to independent failure modes (Moeschberger and David, 1974; Moeschberger and Klein, 1995; Chen *et al.*, 2008; Cai and Prentice, 1995). Specialized models have also been developed to provide treatment of

competing risks for sequential failures (Dignam *et al.*, 2007) and parallel systems (Tan, 2007) as well.

Once the failure probabilities associated with the individual anomaly types are known, they can be used to calibrate probabilistic models for each anomaly type. The resulting calibrated probabilistic models can then be used to predict the behavior of components with different numbers and types of anomalies.

3.1.2 Estimating Marginal Probability Densities from Component Failure Data

The conditional probability of failure $P(F_i|d_1)$ associated with a single anomaly can be estimated from test specimens containing single anomalies. The probability of failure associated with multiple anomalies p_i can then be obtained by inserting $P(F_i|d_1)$ in Eqn. (5). However, if the test specimens contain multiple anomalies, the results are provided in terms of p_i . Reliability predictions based on these test results are only valid for components with exactly the same number of anomalies associated with the test specimens. To estimate risk for different numbers of anomalies, the test results can be converted to conditional probability format by solving Eqn. (5) for $P(F_i|d_1)$ and applying the values of p_i and $\lambda_i V_i$ associated with the test:

$$P(F_i|d_1) = \frac{-1}{\lambda_i V_i} \ln[1 - p_i] \quad (8)$$

The conditional probability density associated with $P(F_i|d_1)$ is referred to herein as a “parent distribution” because it represents life values without the influence of multiple anomalies. The mean life value associated with the parent distribution may be significantly greater than the mean of the measured life values of specimens containing multiple anomalies, particularly when the number of anomalies is large.

For components with more than one type of anomaly, the above procedure can be performed separately for test specimens each containing a single anomaly type. If test data are available only for specimens containing multiple anomalies of multiple types, then the test results are an expression of p_F (Eqn. (7)) rather than p_i (Eqn. (5)). In this situation, each component test represents the entire system of multiple anomaly types/locations as well as the multiple anomalies subsystems associated with each. If the failure of components with multiple anomalies can be traced to specific anomaly types, then the p_i values can be estimated using the Kaplan-Meier (1958) method. The approach is illustrated in the following example.

Consider the fictitious component indicated in Table 1 with two types of anomalies (types *A* and *B*) that can form growing cracks which can lead to fracture failure of the component. The component has a volume of 1 mm³ and contains an average of 10 and 100 anomalies of type *A* and *B*, respectively. For each anomaly type, the total fatigue life given the presence of a single anomaly of a single type (parent life) is modeled as a lognormal random variable with the main descriptors (median and coefficient of variation (COV)) indicated in Table 1.

Table 1. Anomaly Parameters for Example Component Containing Two Types of Anomalies

Anomaly Type	Anomaly Rate (1/mm ³)	Total Life Given a Single Anomaly of a Single Type (Parent Life)		
		Median	COV	Dist
<i>A</i>	10	1000	0.3	Lognormal
<i>B</i>	100	2000	0.5	Lognormal

The analytical probability of failure cumulative distribution functions (CDFs) associated with the life distributions of the parent total life and multiple anomalies of a single type are shown in Figure 5. Also shown is the probability of failure of the example component containing multiple anomalies of type *A* and *B*, computed analytically using Eqn. (7). This figure illustrates the risk prediction approach of components with multiple anomaly types when the parent lives are known.

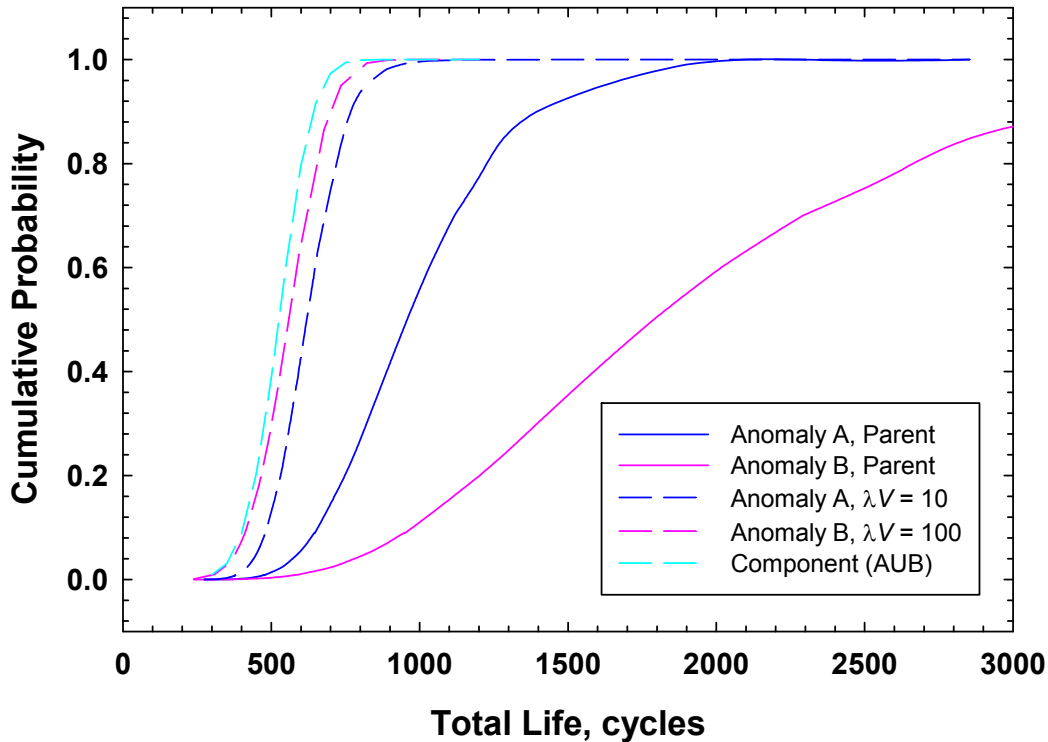


Figure 5. Analytical probability of failure values associated with single and multiple anomalies of a single type for the example component containing multiple anomaly types.

The probability of failure of the example component containing multiple anomaly types can also be obtained using numerical simulation. 1000 simulated specimens containing multiple anomalies of each anomaly type were obtained using Monte Carlo simulation, indicated in Table 2. The failure time of each component (the minimum life associated with anomaly types *A* and *B*) was recorded along with the anomaly type responsible for the failure.

Table 2. Simulated Failure of Example Component with Two Types of Anomalies

Simulated Specimen	Cycles to Failure			Failure Data		
	<i>A</i>	<i>B</i>	$\min(A,B)$	<i>A</i>	<i>B</i>	<i>AUB</i>
1	607	648	607	607	—	607
2	492	501	492	492	—	492
3	633	566	566	—	566	566
4	488	720	488	488	—	488
5	483	642	483	483	—	483
7	803	664	664	-	664	664
8	488	508	488	488	—	488
—	—	—	—	—	—	—
998	567	534	534	-	534	534
999	619	663	619	619	—	619
1000	818	602	602	—	602	602

The CDF for the simulated component can be obtained by arranging the component failure times in ascending order and assigning cumulative failure probabilities $F(t)$ to each time value. For uncensored failure data, $F(t)$ is typically estimated as $a/(b+1)$ (Ang and Tang, 1975) or $(a-0.5)/b$ (Meeker and Escobar, 1998), where i is the rank order of the specimens and k is the total number of specimens. Using this approach (with $F(t) = a/(b+1)$), CDF values were obtained as indicated in Table 3 and shown in Figure 6. Also shown in Figure 6 is the CDF obtained analytically using Eqn. (7), which is in close agreement with the simulated values, as expected.

Table 3. Simulated CDF Values for Example Component Containing Two Types of Anomalies

<i>k</i>	Total Life (cycles)	$F(t)$
1	247	0.0010
2	279	0.0020
3	284	0.0030
4	290	0.0040
5	292	0.0050
—	—	—
997	747	0.9960
998	756	0.9970
999	773	0.9980
1000	815	0.9990

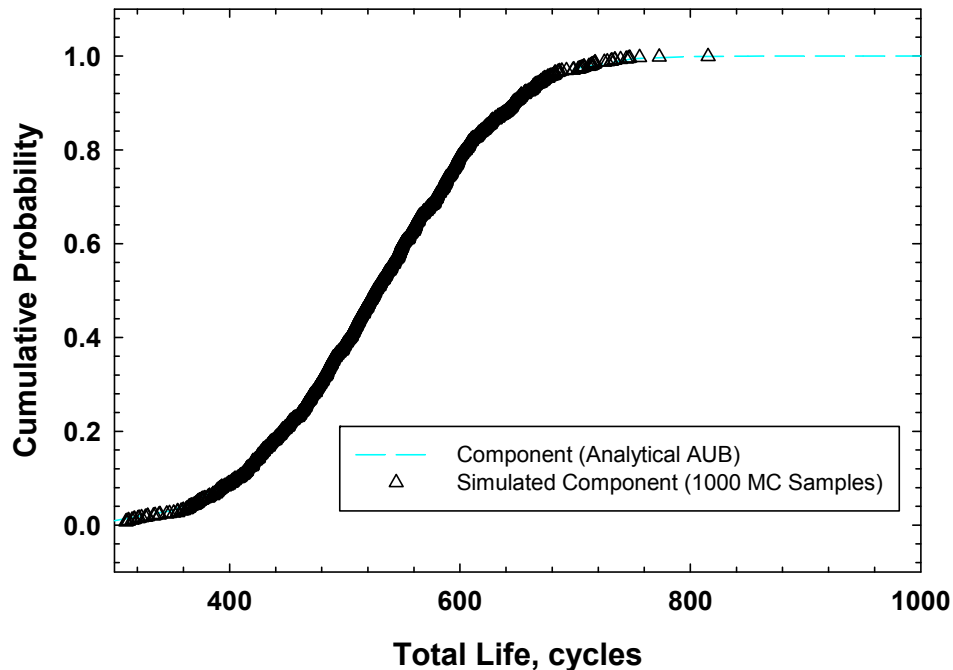


Figure 6. Analytical and simulated probability of failure of failure values for the example component containing two anomaly types were in close agreement, as expected.

But suppose instead that the 1000 samples were obtained from component fatigue tests. In this situation, the CDFs for the individual anomaly types and their associated parent distributions would be unknown, and would have to be estimated from the failed specimen data. Assuming that the failure of each specimen could be traced to a specific anomaly type, the data could then be used to estimate the CDF associated with each anomaly type. However, since the data were not obtained from specimens of a single anomaly type, special care must be taken when fitting the data to CDFs.

A common approach for estimating the CDF of a single anomaly type from test data containing multiple anomaly types is to consider only the failure times that can be traced to the individual anomaly type and constructing a CDF using the previously described procedure for uncensored data. The CDFs obtained using this approach are shown in Figure 7 for anomaly types *A* and *B*. The analytical CDF values for anomaly types *A* and *B* are also shown in Figure 7 for comparison purposes. The CDF curves based on a fit of only the failure times that can be traced to the individual anomaly types are significantly different from the analytical values. Furthermore, when these CDF curves are used to predict the CDF of the component (using Eqn. (6)), the results are not in agreement with either the analytical or simulated results of the component (from Figure 6).

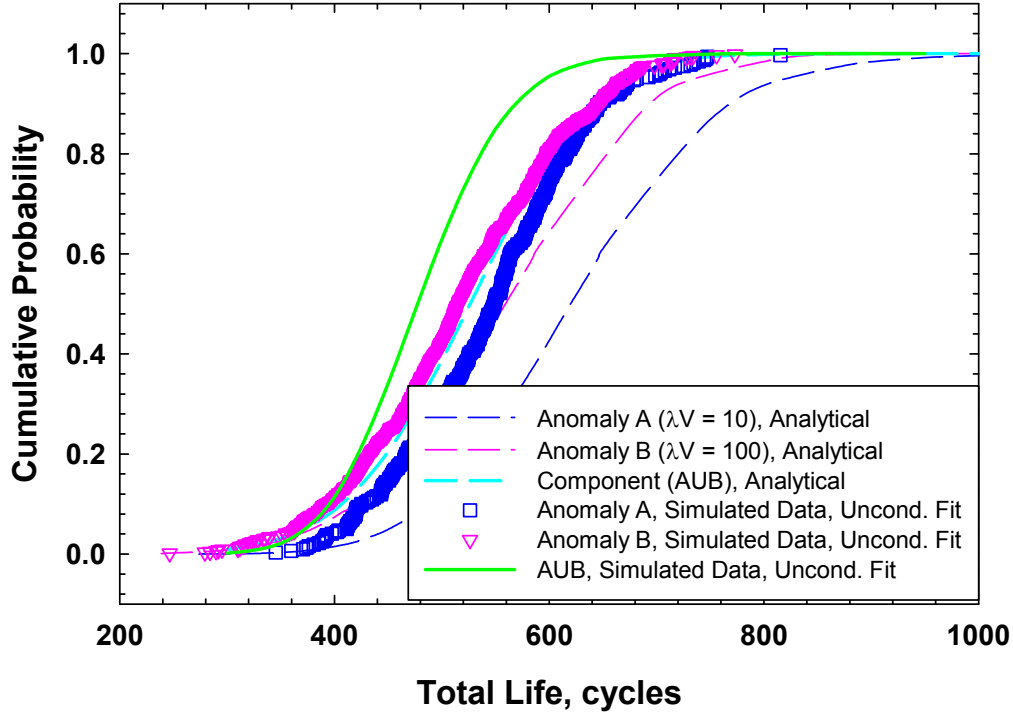


Figure 7. CDF values for individual anomaly types estimated from censored failure data were significantly different from the analytical values.

The reason for this difference is that some of the life values are censored by the testing process. A given component fails when the minimum lifetime associated with any anomaly is reached, and the lifetimes associated with all other anomaly types in the component are not recorded (they are censored). The CDFs cannot be obtained using this approach because many of the data are missing.

Fortunately, statistical methods are well-established for treatment of competing risks (Kaplan and Meier, 1958; Nelson, 1972; Aalan, 1978; Moeschberger and David, 1974; Moeschberger and Klein, 1995; Chen *et al.*, 2008; Cai and Prentice, 1995) that can be applied to this problem. If the failure times associated with the different anomaly types are treated as independent random variables, then the Kaplan-Meier method (1958) can be used to estimate the CDFs associated with each anomaly type. In this method, the lifetime is discretized into k intervals, and the probability of survival within an interval P_k for an anomaly type is based on the ratio of the number of components that survive over the interval to the number of components that were available at the beginning of the interval:

$$P_k = \frac{n_k - f_k}{n_k} \quad (9)$$

A conditional probability argument is made to establish the relationship among the survival probabilities associated with all of the non-overlapping intervals. After the first time interval, some of the components may fail. During the second time interval, only the components that

have not failed during the first interval are tested. In other words, to survive the second time interval, it is implied that the component has also survived the first time interval:

$$P(I_2) = P(I_1 \cap I_2) = P(I_1) \cdot P(I_2 | I_1) \quad (10)$$

Combining Eqns. (9) and (10), and recognizing that P_2 is the conditional probability that a component survives interval 2 given that it has also survived interval 1 ($P(I_2 | I_1)$):

$$P(I_1 \cap I_2) = P_1 \cdot P_2 = \left(\frac{n_1 - f_1}{n_1} \right) \cdot \left(\frac{n_2 - f_2}{n_2} \right) \quad (11)$$

It follows that the probability of survival over m number of time intervals is given by:

$$P(t) = \prod_{k=1}^m \left(\frac{n_k - f_k}{n_k} \right) \quad (12)$$

and the associated probability of failure is:

$$F(t) = 1 - P(t) = 1 - \prod_{k=1}^m \left(\frac{n_k - f_k}{n_k} \right) \quad (13)$$

One potential drawback of the Kaplan-Meier method is that the probability of failure values are expressed in a step function format, similar to the integrated form of a histogram. The resulting curve contains discontinuities at each of the failure times and therefore does not satisfy the requirements of a true CDF. To estimate the continuous CDF, Meeker and Escobar (1998) recommend setting the CDF values at each step equal to the average of the two values associated with each step change:

$$F(t) = \frac{1}{2} [F(t_k) + F(t_{k-1})] \quad (14)$$

The application of the Kaplan-Meier approach is illustrated in Tables 4 and 5 for the simulated failure data associated with anomaly types A and B , respectively. Similar to the approach previously presented for uncensored data, the component failure times were arranged in ascending order, and the time intervals were selected so that only a single failure occurred during a given interval. However, for a given anomaly type, CDF values were assigned to all of the component failure times for both anomaly types. In Table 4, the first failure associated with anomaly A did not occur until interval 24. The CDF value obtained using the Kaplan-Meier method (indicated as “K-M” in Table 4) experienced a step change at interval 24, and remained unchanged until the next failure of anomaly A at interval 31, and so on. In Table 5, the first failure associated with anomaly B occurred at the first interval, and the K-M CDF experienced a step change over every interval until the first failure associated with anomaly A . The continuous CDF estimate obtained using Eqn. (14) is also indicated in Tables 4 and 5 as the “M-E” CDF.

Table 4. Failure CDF for Anomaly Type A Using Kaplan-Meier Approach Combined with Meeker-Escobar Data Fit

Total Life	k	n_k	f_k	p_k	P_k	K-M F(t)	M-E F(t)
0	0	1000	0	1.000	1.000	0.000	0.0000
247	1	1000	0	1.000	1.000	0.000	0.0000
279	2	999	0	1.000	1.000	0.000	0.0000
—	—	—	—	—	—	—	—
340	23	978	0	1.000	1.000	0.000	0.0000
345	24	977	1	0.999	0.999	0.001	0.0005
348	25	976	0	1.000	0.999	0.001	0.0010
—	—	—	—	—	—	—	—
358	30	971	0	1.000	0.999	0.001	0.0010
360	31	970	1	0.999	0.998	0.002	0.0015
360	32	969	0	1.000	0.998	0.002	0.0021
—	—	—	—	—	—	—	—
747	997	4	1	0.750	0.075	0.925	0.9122
756	998	3	0	1.000	0.075	0.925	0.9247
773	999	2	0	1.000	0.075	0.925	0.9247
815	1000	1	1	0.000	0.000	1.000	0.9624

Table 5. Failure CDF for Anomaly Type B Using Kaplan-Meier Approach Combined with Meeker-Escobar Data Fit

Total Life	k	n_k	f_k	p_k	P_k	K-M F(t)	M-E F(t)
0	0	1000	0	1.000	1.000	0.000	0.0000
247	1	1000	1	0.999	0.999	0.001	0.0005
279	2	999	1	0.999	0.998	0.002	0.0015
284	3	998	1	0.999	0.997	0.003	0.0025
290	4	997	1	0.999	0.996	0.004	0.0035
—	—	—	—	—	—	—	—
453	221	780	1	0.999	0.824	0.176	0.1752
453	222	779	0	1.000	0.824	0.176	0.1757
454	223	778	0	1.000	0.824	0.176	0.1757
—	—	—	—	—	—	—	—
746	996	5	0	1.000	0.040	0.960	0.9601
747	997	4	0	1.000	0.040	0.960	0.9601
756	998	3	1	0.667	0.027	0.973	0.9668
773	999	2	1	0.500	0.013	0.987	0.9801
815	1000	1	0	1.000	0.013	0.987	0.9867

The CDFs estimated using the Kaplan-Meier approach combined with the Meeker-Escobar adjustment are shown in Figure 8 for anomaly types *A* and *B*. Also shown is the analytical probability of failure of components containing multiple anomalies of only type *A* or type *B*. It can be observed that the CDF values for individual anomaly types estimated using the Kaplan-Meier approach combined with the Meeker-Escobar data fit were in close agreement with the analytical values. The CDF for a component with anomalies *A* and *B* (estimated using Eqn. (6)) is also shown in Figure 8. It is also in close agreement with the analytical component values.

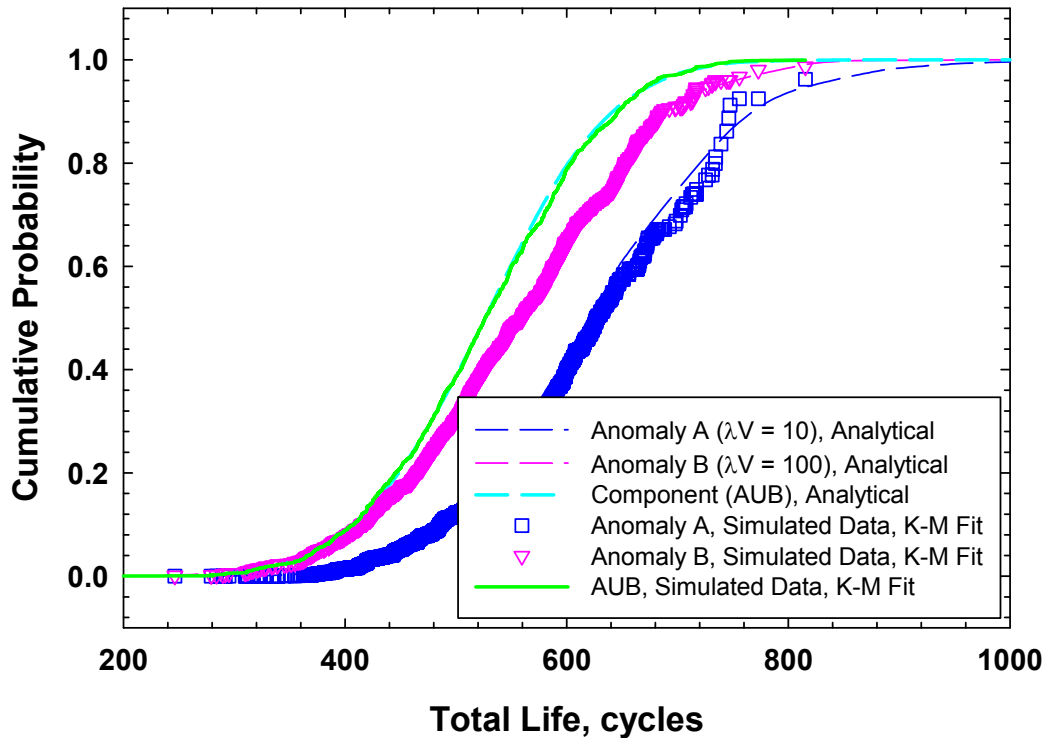


Figure 8. CDF values for individual anomaly types estimated using the combined Kaplan-Meier/Meeker-Escobar approach were in close agreement with the analytical values.

Once the marginal CDF values for anomaly types *A* and *B* have been estimated using the Kaplan-Meier/Meeker-Escobar approach, they can be transformed to the associated parent distributions using Eqn. (8). The resulting CDF values are shown in Fig. 9. The analytical parent distributions are also shown in Fig. 9, where it can be observed that they are both in close agreement with the values estimated from the transformed failure data. This illustrates how the approach is used to obtain the parent distributions which are ultimately used for risk prediction of components with different numbers of anomalies of multiple types.

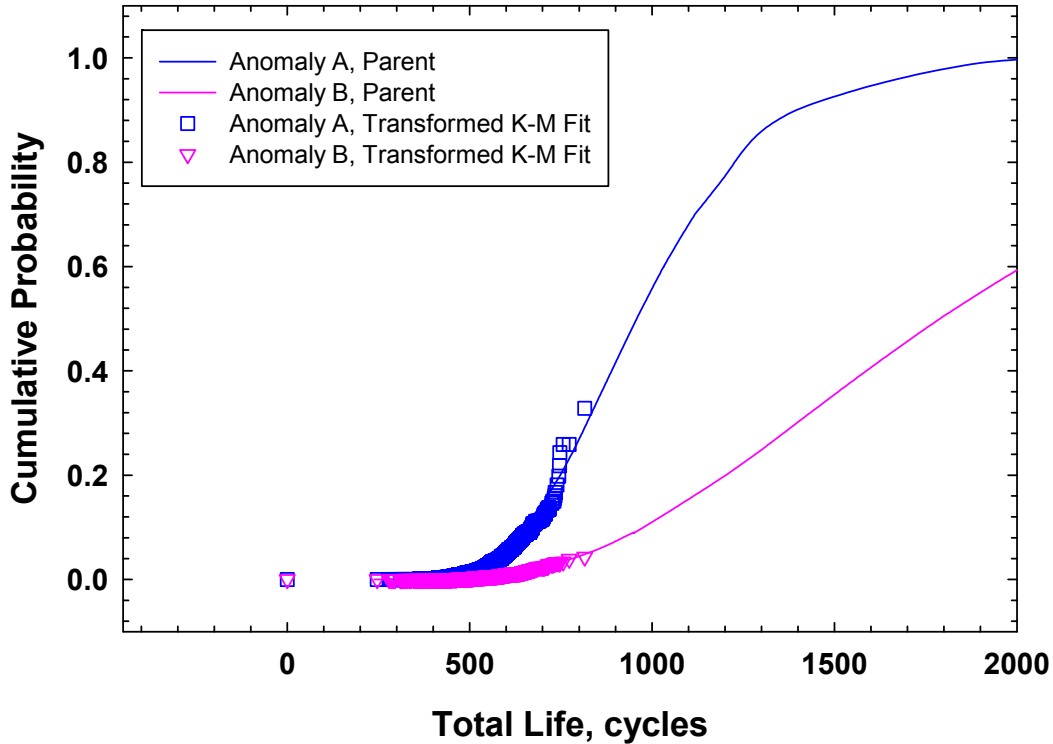


Figure 9. The transformed CDF values based on the Kaplan-Meier/Meeker-Escobar approach were in close agreement with the analytical parent distributions.

3.1.3 Application to Gas Turbine Engine Materials

The approach described in Section 3.1.2 was applied to reliability prediction of a nickel-based superalloy based on data provided by the AFRL (AFRL, also reported in Jha *et al.*, 2008). The material contained non-metallic particles (NMPs) and pores with anomaly occurrence rates indicated in Table 6. AFRL had previously performed fatigue tests on cylindrical smooth specimens (diameter = 5 mm and gage length = 15 mm) at four stress levels (1200 MPa, 1150 MPa, 1100 MPa, and 1000 MPa). All tests were conducted at a stress ratio of $R = 0.05$ and a temperature of 650C. The test results at 1100 MPa revealed failures that could be traced to several anomaly types/locations and were selected for use in the reliability studies. As indicated in Table 7, NMP failures were identified at both the surface and subsurface of the specimens at this stress level, whereas pore failures occurred only on the surface.

Table 6. Anomaly Types Associated with Nickel-Based Superalloy Test Specimens

Anomaly		Occurrence Rate		Volume	Average Number	
Type	Location	per mm ³	per mm ²	mm ³	Total	Effective
NMPs	Surface	10	0.17	4.0	40.2	3.4
NMPs	Subsurface	10	0.17	290.5	2905.1	250.3
Pores	Surface	2445	19	1.8	4475.0	306.9

Table 7. Component Failure CDF for Nickel-Based Superalloy Smooth Specimen Fatigue Failure Data with Applied Stress of 1100 MPa

<i>k</i>	Type	Location	Total Life	F(t)
0	—	—	0	0
1	NMP	Surface	1736	0.0625
2	NMP	Surface	2210	0.1250
3	NMP	Surface	2309	0.1875
4	NMP	Surface	3237	0.2500
5	Pore	Surface	9446	0.3125
6	Pore	Surface	13188	0.3750
7	NMP	Subsurface	18405	0.4375
8	Pore	Surface	18525	0.5000
9	NMP	Subsurface	21936	0.5625
10	NMP	Subsurface	25081	0.6250
11	NMP	Subsurface	26417	0.6875
12	NMP	Subsurface	31736	0.7500
13	Pore	Surface	45337	0.8125
14	NMP	Subsurface	65021	0.8750
15	NMP	Subsurface	76339	0.9375

The volume of material associated with the surface anomalies was based on a thin annulus (often referred to as an “onion skin”) at which the number of anomalies associated with the volumetric occurrence rate (Table 6) matched the number of anomalies associated with the surface occurrence rate. The subsurface volume was based on the remaining volume (*i.e.*, the total volume minus the surface volume). The average number of anomalies for each anomaly type and location was computed as the product of the volume and the volumetric occurrence rate, indicated in Table 6. Since many of the anomalies were too small to initiate growing cracks, an effective number of anomalies that could lead to failure was estimated based on a minimum threshold equivalent anomaly diameter (40 μm for NMPs, and 21 μm for pores).

The CDFs for each of the three anomaly type/location combinations associated with the material were estimated using the combined Kaplan-Meier/Meeker-Escobar approach described in Section 3.1.2. The results for surface NMPs are indicated in Table 8, where the failures all occurred at relatively short life values compared to the other anomaly types/locations. The results for subsurface NMPs and surface pores are indicated in Tables 9 and 10, respectively. The marginal CDFs indicated in Tables 8-10 are shown in Figure 10. Also shown in Figure 10 is the CDF for all anomalies (indicated in Table 7) which was obtained using the approach for uncensored data described previously in Section 3.1.2.

Table 8. Failure CDF for Surface NMPs Using Kaplan-Meier/Meeker-Escobar Approach

Total Life	k	n_k	f_k	p_k	P_k	K-M F(t)	M-E F(t)
0	0	15	0	1.000	1.000	0.000	0.000
1736	1	15	1	0.933	0.933	0.067	0.033
2210	2	14	1	0.929	0.867	0.133	0.100
2309	3	13	1	0.923	0.800	0.200	0.167
3237	4	12	1	0.917	0.733	0.267	0.233
9446	5	11	0	1.000	0.733	0.267	0.267
13188	6	10	0	1.000	0.733	0.267	0.267
18405	7	9	0	1.000	0.733	0.267	0.267
18525	8	8	0	1.000	0.733	0.267	0.267
21936	9	7	0	1.000	0.733	0.267	0.267
25081	10	6	0	1.000	0.733	0.267	0.267
26417	11	5	0	1.000	0.733	0.267	0.267
31736	12	4	0	1.000	0.733	0.267	0.267
45337	13	3	0	1.000	0.733	0.267	0.267
65021	14	2	0	1.000	0.733	0.267	0.267
76339	15	1	0	1.000	0.733	0.267	0.267

Table 9. Failure CDF for Subsurface NMPs Using Kaplan-Meier/Meeker-Escobar Approach

Total Life	k	n_k	f_k	p_k	P_k	K-M F(t)	M-E F(t)
0	0	15	0	1.000	1.000	0.000	0.000
1736	1	15	0	1.000	1.000	0.000	0.000
2210	2	14	0	1.000	1.000	0.000	0.000
2309	3	13	0	1.000	1.000	0.000	0.000
3237	4	12	0	1.000	1.000	0.000	0.000
9446	5	11	0	1.000	1.000	0.000	0.000
13188	6	10	0	1.000	1.000	0.000	0.000
18405	7	9	1	0.889	0.889	0.111	0.056
18525	8	8	0	1.000	0.889	0.111	0.111
21936	9	7	1	0.857	0.762	0.238	0.175
25081	10	6	1	0.833	0.635	0.365	0.302
26417	11	5	1	0.800	0.508	0.492	0.429
31736	12	4	1	0.750	0.381	0.619	0.556
45337	13	3	0	1.000	0.381	0.619	0.619
65021	14	2	1	0.500	0.190	0.810	0.714
76339	15	1	1	0.000	0.000	1.000	0.905

Table 10. Failure CDF for Surface Pores using Kaplan-Meier/Meeker-Escobar Approach

Total Life	k	n_k	f_k	p_k	P_k	K-M F(t)	M-E F(t)
0	0	15	0	1.000	1.000	0.000	0.000
1736	1	15	0	1.000	1.000	0.000	0.000
2210	2	14	0	1.000	1.000	0.000	0.000
2309	3	13	0	1.000	1.000	0.000	0.000
3237	4	12	0	1.000	1.000	0.000	0.000
9446	5	11	1	0.909	0.909	0.091	0.045
13188	6	10	1	0.900	0.818	0.182	0.136
18405	7	9	0	1.000	0.818	0.182	0.182
18525	8	8	1	0.875	0.716	0.284	0.233
21936	9	7	0	1.000	0.716	0.284	0.284
25081	10	6	0	1.000	0.716	0.284	0.284
26417	11	5	0	1.000	0.716	0.284	0.284
31736	12	4	0	1.000	0.716	0.284	0.284
45337	13	3	1	0.667	0.477	0.523	0.403
65021	14	2	0	1.000	0.477	0.523	0.523
76339	15	1	0	1.000	0.477	0.523	0.523

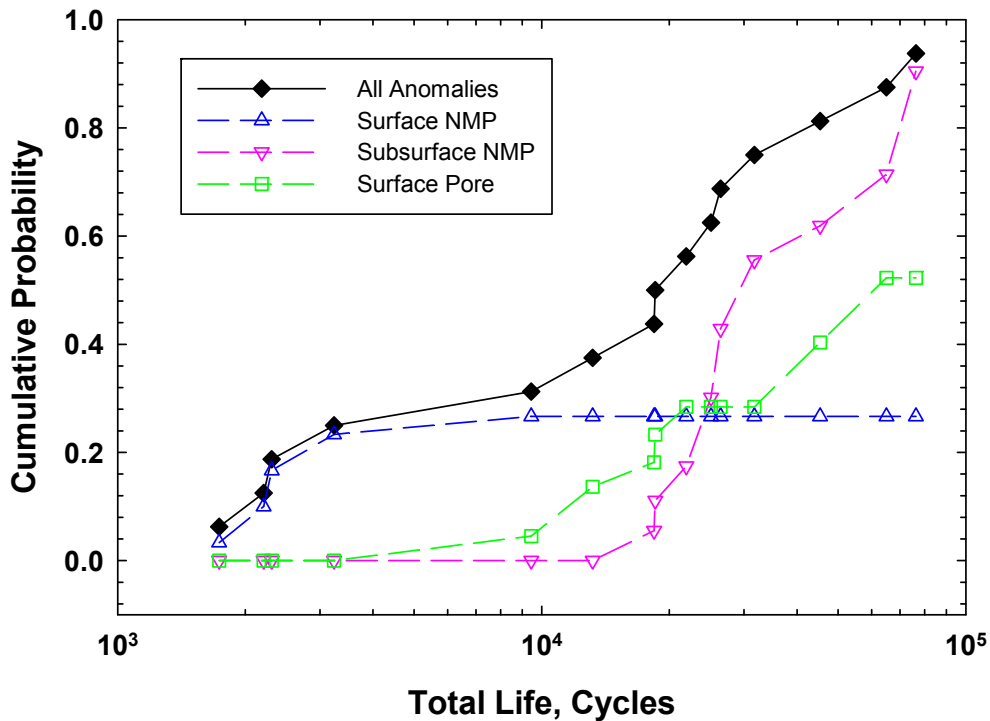


Figure 10. The marginal CDFs for each anomaly type were obtained from the Kaplan-Meier/Meeker-Escobar fit of the failure data.

The parent distributions were obtained by applying the effective number of anomalies and the $F(t)$ values to Eqn. (8) at each life value. The transformed CDFs are shown in Figure 11, where it can be observed that the surface NMPs have a significant influence on component reliability when single anomalies are considered.

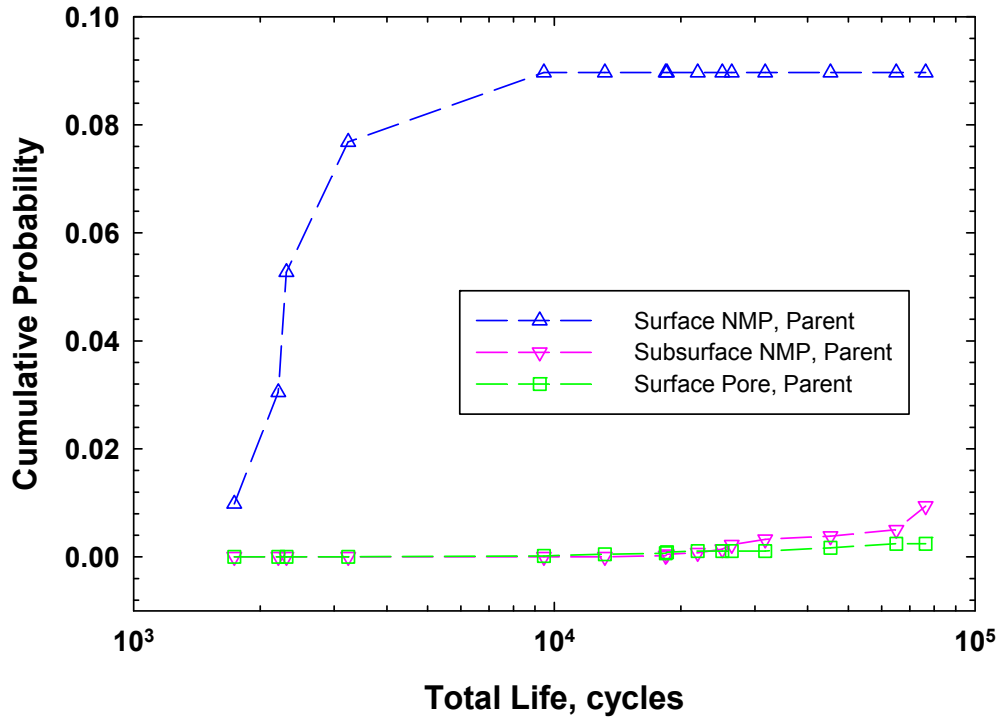


Figure 11. The parent CDFs were determined by transforming the marginal CDF values for each anomaly type.

The parent CDFs shown in Figure 11 can be used to make reliability predictions for components with different numbers of anomalies. Compared to realistic engine components such as rotors or disks, the smooth specimens have a relatively small volume to surface area ratio. To study this effect, reliability predictions were made for a range of volume to surface area ratio values indicated in Table 11 (the volume to area ratio of the test specimens was assigned a value of 1.0). The results are shown in Figure 12, where it can be observed that component failure probabilities at early lives were dominated by surface NMPs for all of the volume to surface area ratios considered. The surface pores and subsurface NMPs had the most influence near the middle and end of life, where the component CDF values were already very large.

Table 11. Influence of Component Volume to Surface Area Ratio on Number of Anomalies for Each Anomaly Type

Volume to Area Ratio	Diameter (mm)	Number of Active Anomalies		
		Surface NMP	Subsurface NMP	Surface Pore
1	5	3	250	306
2	10	7	1008	613
5	25	17	6326	1532
10	50	35	25338	3065

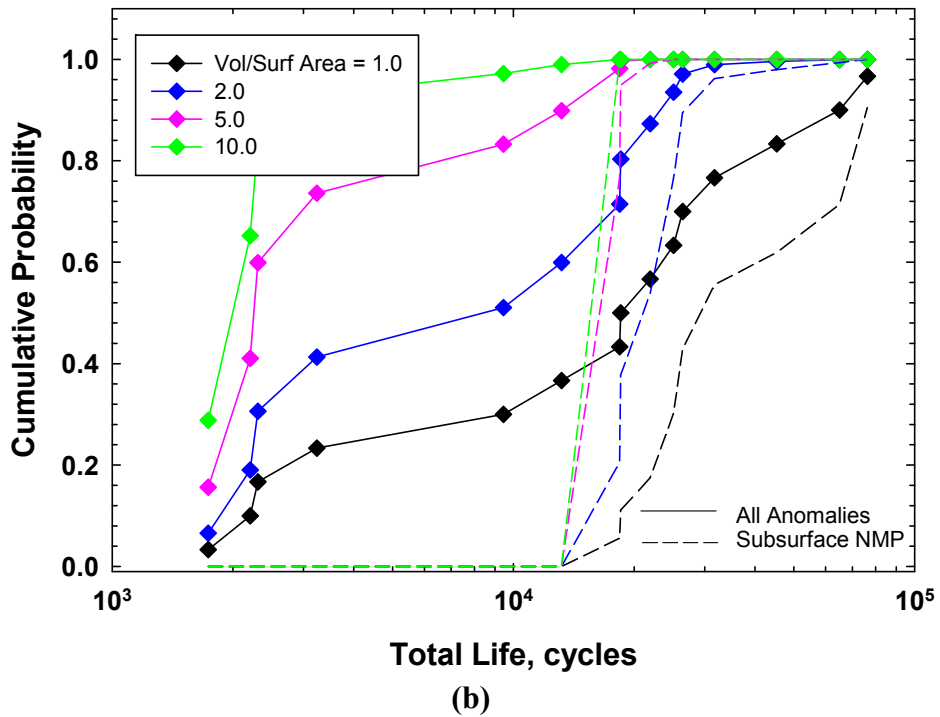
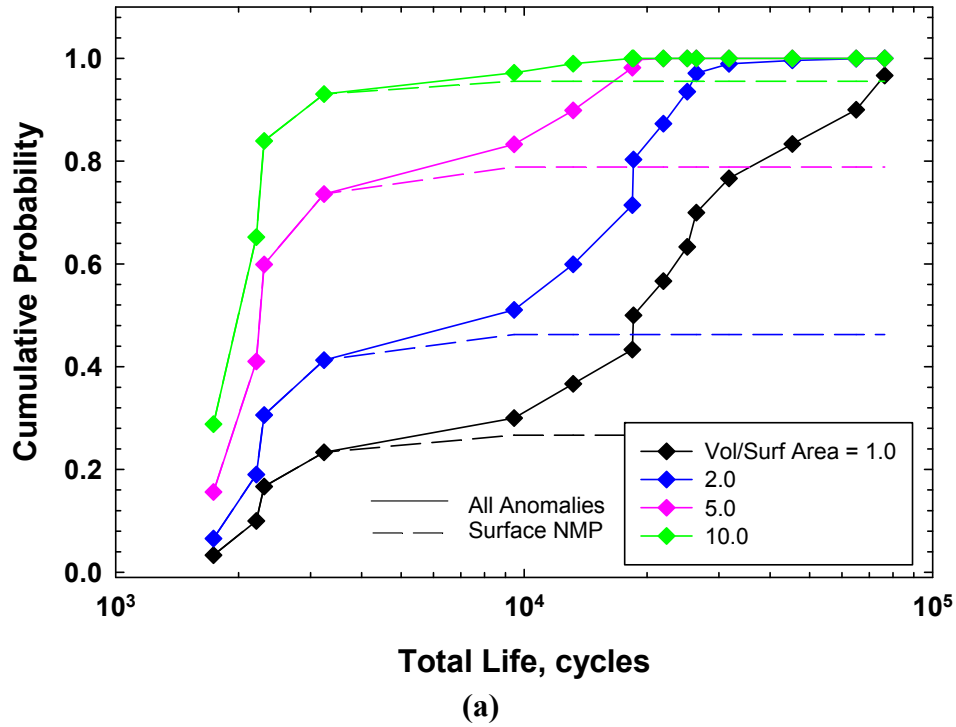


Figure 12. The influence of volume to surface area ratio on probability of failure and associated contribution of: (a) surface NMPs, (b) subsurface NMPs, and (c) surface pores.

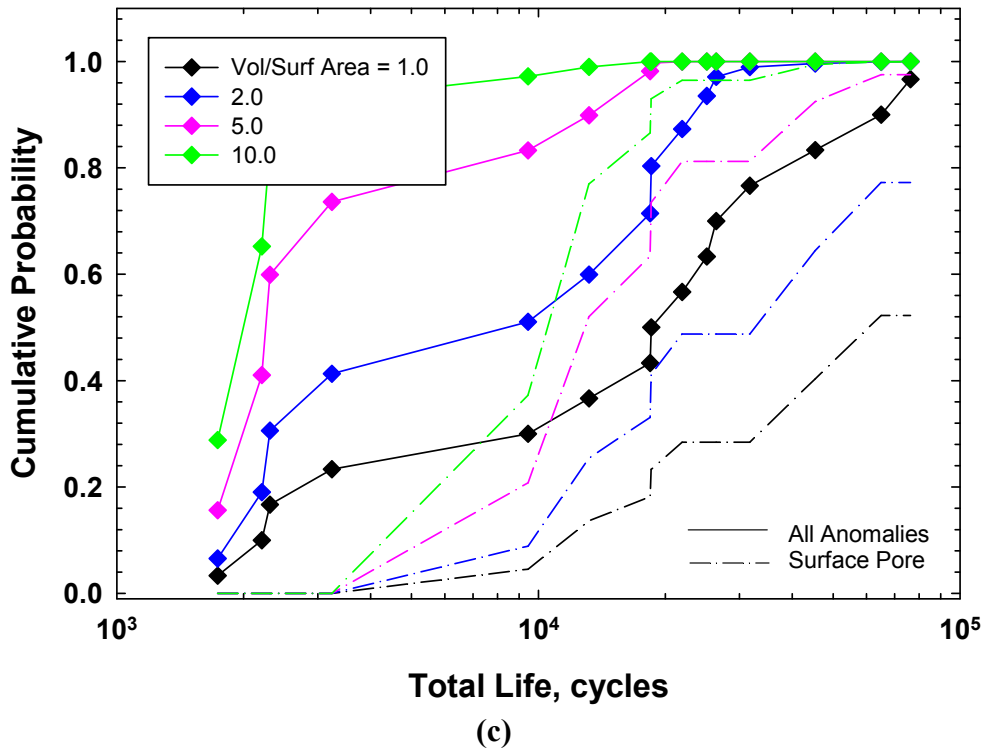


Figure 12 (cont). The influence of volume to surface area ratio on probability of failure and associated contribution of: (a) surface NMPs, (b) subsurface NMPs, and (c) surface pores.

As indicated in Table 11, the number of subsurface NMPs becomes very large as the volume to area ratio is increased. For a volume/area value of 10, there are substantially more subsurface NMP anomalies compared to the other types present. This suggests that these anomaly types should play more of a role in component failures as the volume to area ratio is increased. This is confirmed in Figure 12(b) where it can be observed that the slope of the CDF associated with subsurface NMPs becomes considerably steeper as the volume to area ratio increases from 1 to 10. With such a large number of subsurface NMPs available at relatively high volume to area ratios, one might intuitively expect subsurface NMPs to also play a role in component failures at relatively low life values. However, Figure 12(a) shows that the surface NMPs are much more likely to fail at the low life values because the slope of the CDF of surface NMPs increases significantly with an increase in the volume to surface area ratio. The probabilistic model predicts that subsurface NMPs and surface pores will fail only after the surface pores have been exhausted. So although the subsurface NMPs are more plentiful than the other anomaly types, there are still enough surface NMPs available to substantially influence the early stages of component life.

For this material, the dominant failure mechanism was not significantly influenced by changes in the volume to area ratio, which suggests that the smooth specimen test results could be directly used to predict the failure mechanisms of full scale engine components. Further research is required to investigate the extent of this relationship.

3.2 Development of an Unfolding Algorithm for Estimating Spheroid Parameters from Sectioning Data Measurements

3.2.1 Introduction

As part of the OEM engagement task, SwRI learned that at least one of the OEMs uses only sectioning data to characterize anomalies in powder materials. Several GRC studies focused on this method, and an unfolding algorithm was developed by Ghosn *et al.* (2003) that was successful for some anomalies (-80+100 mesh metal powder) but was less successful for others (-270 mesh metal powder). Since one of the ultimate objectives of this project was to transfer the technologies developed at GRC into DARWIN, an unfolding algorithm was developed and implemented in software at SwRI to investigate the accuracy of the unfolding method. To verify the algorithm, a fictitious material containing a known distribution of spheroidal anomalies was simulated through sectioning and unfolding to reveal the potential computational errors associated with this approach.

Wicksell (1925, 1926) investigated the problem of estimating the size-shape distributions of spheres and ellipsoids from the data of the circles or ellipses observed in planar sections. Cruz-Orive (1976, 1977) proved that the ellipsoidal problem cannot be solved universally. The equation for the general stereological problem has unique solutions only for particular families of ellipsoids called spheroids, which are biaxial ellipsoids. The spheroids may have random size and shape, not necessarily independent from each other, but they must all be either prolate or oblate for a given model. For prolate spheroids (elongated “football” shape) the major axis is the rotator axis, whereas the minor axis is the rotator axis for oblate spheroids (flattened “pancake” shape).

3.2.2 The Stereological Equation`

The general problem of predicting the size-shape distribution from the measurements of section profiles is described by the stereological equation (Cruz-Orive 1976, 1977; Ohser and Mücklich 2000). Let the size parameters U and S be the major caliper parameter of a spheroid and its planar section profile, respectively. Let V be the shape parameter of a typical spheroid and T be the random shape parameter of a random section profile. Let $F_V(u, v)$ and $F_A(s, t)$ denote the bivariate size-shape distribution functions of the spheroids and their elliptical section profiles, respectively, where $F_V(u, v) = P(U \leq u, V \leq v)$ and $F_A(s, t) = P(S \leq s, T \leq t)$. The probability of both $S > s$ and $T > t$ is given by:

$$P(S > s, T > t) = 1 - F_A(\infty, t) - F_A(s, 1) + F_A(s, t) \quad (15)$$

The stereological equation describes the relationship among the distribution functions of the spheroids and elliptical section profiles of prolate or oblate spheroids whose principal major and minor semi-axes are a and b , respectively:

$$N_A [1 - F_A(\infty, t) - F_A(s, 1) + F_A(s, t)] = N_V \int_s^\infty \int_t^1 p(u, v, s, t) dF_V(u, v), \quad (16)$$

where $0 < s$ and $0 < t \leq 1$. The shape parameter is defined as $v = 1 - (b/a)^2$. The bi-dimensional size-shape variables (u, v) for prolate and oblate spheroids are (b, v) and (a, v) , respectively. Similarly, the size-shape parameter (s, t) for elliptical profiles is defined as $(a, 1 - (b/a)^2)$, where a and b are the principal major and minor semi-axes of the elliptical profiles, respectively (Cruz-Orive, 1976).

3.2.3 Numerical Solution of the Stereological Equation

The unfolding algorithm proposed by Cruz-Orive is described in this section. There is a close correspondence between linear integral Eqn. (2) which specify linear relations among distribution functions and linear equations which specify analogous relations among vectors of relative frequencies. The stereological integral Eqn. (2) can be transformed into a linear equation system:

$$\mathbf{N}_A = \mathbf{P}\mathbf{N}_V\mathbf{Q} \quad (17)$$

where \mathbf{N}_V and \mathbf{N}_A are vectors of relative frequencies of the spheroids and their elliptical profiles, respectively. \mathbf{P} and \mathbf{Q} are transformation matrices corresponding to the kernel function $p(u, v, s, t)$ in Eqn. (2). Suppose the range $(0, B)$ of size component b (or a) is divided into s bins of equal width B/s , and the range $(0, 1)$ of the shape component is divided into k bins of equal width $1/k$. The rectangular domain of variable (b, v) or (a, v) is divided into a grid comprising $s \times k$ “cells”. The relative frequencies of spheroids per unit volume are:

$$\mathbf{N}_V = \{N_V(i, j); i = \overline{1, s}, j = \overline{1, k}\}, \quad (18)$$

where $N/V \equiv N_V$, note that $\sum_{i=1}^s \sum_{j=1}^k N_V(i, j) = N_V$. The relative frequencies of elliptical profiles per unit area are:

$$\mathbf{N}_A = \{N_A(\alpha, \beta); \alpha = \overline{1, s}, \beta = \overline{1, k}\}, \quad (19)$$

where $N_A(\alpha, \beta) \equiv N_A f_{\alpha\beta}$. Clearly, $\sum_{\alpha=1}^s \sum_{\beta=1}^k N_A(\alpha, \beta) = N_A$. Solving Eqn. (3) yields:

$$N_V(i, j) = \Delta^{-1} \sum_{\alpha=i}^S \sum_{\beta=j}^k p^{i\alpha} N_A(\alpha, \beta) q^{\beta j}, \quad (i = \overline{1, s}, j = \overline{1, k}), \quad (20)$$

where $p^{i\alpha}$, $q^{j\beta}$ are the elements of matrices \mathbf{P}^{-1} and \mathbf{Q}^{-1} , respectively. \mathbf{P} is an upper triangular matrix that is size dependent, whereas \mathbf{Q} is a lower triangular matrix that is shape dependent. The elements of matrices \mathbf{P} and \mathbf{Q} are given as follows:

$$P_{\alpha i} = \begin{cases} \sqrt{(i - 1/2)^2 - (\alpha - 1)^2} - \sqrt{(i - 1/2)^2 - \alpha^2}; & (\alpha = \overline{1, i-1}, i = \overline{2, s}), \\ \sqrt{i - 3/4} & ; (\alpha = i, \quad i = \overline{1, s}), \\ 0 & ; (\alpha > i, \quad i = \overline{1, s}). \end{cases} \quad (21)$$

For populations consisting of prolate spheroids, we have,

$$q_{j\beta} = \begin{cases} \sqrt{t_1^2 - 1}[f(t_\beta) - f(t_{\beta+1})]; & (\beta = \overline{1, j-1}, j = \overline{2, k}), \\ \sqrt{t_1^2 - 1} f(t_j) & ; (\beta = j, \quad j = \overline{1, k}), \\ 0 & ; (\beta > j, \quad j = \overline{1, k}), \end{cases} \quad (22)$$

where:

$$f(t) = t/(t^2 - 1) + \arg \tanh(t), \quad t_\beta = [(2k - 2\beta + 2)/(2j - 2\beta + 1)]^{1/2}.$$

and:

$$q_{j\beta} = \begin{cases} \sqrt{1 + t_1^{-2}}[f(t_\beta) - f(t_{\beta+1})]; & (\beta = \overline{1, j-1}, j = \overline{2, k}), \\ \sqrt{1 + t_1^{-2}} f(t_j) & ; (\beta = j, \quad j = \overline{1, k}), \\ 0 & ; (\beta > j, \quad j = \overline{1, k}), \end{cases} \quad (23)$$

where:

$$\text{where } f(t) = t/(t^2 + 1) + \arctan(t), \quad t_\beta = [(2j - 2\beta + 1)/(2k - 2j + 1)]^{1/2}.$$

3.2.4 Application Example

A Fortran program based on the Cruz-Orive unfolding algorithm was implemented and illustrated for a cubic section of a fictitious material containing oblate spheroidal anomalies. The spheroid dimensions (major axis a and aspect ratio b/a) and orientation angles were modeled as independent uniformly distributed random variables with the values indicated in Table 12. Using Monte Carlo simulation, spheroids with random values of a and b/a were generated and placed at random 3D locations within a cubic section of the fictitious material. To compute the relative frequency of anomalies per unit volume N_V of a given size and aspect ratio, the full ranges of a and b/a values were discretized into s and k bins, respectively. Two discretization schemes were considered: 5×5 and 10×10 .

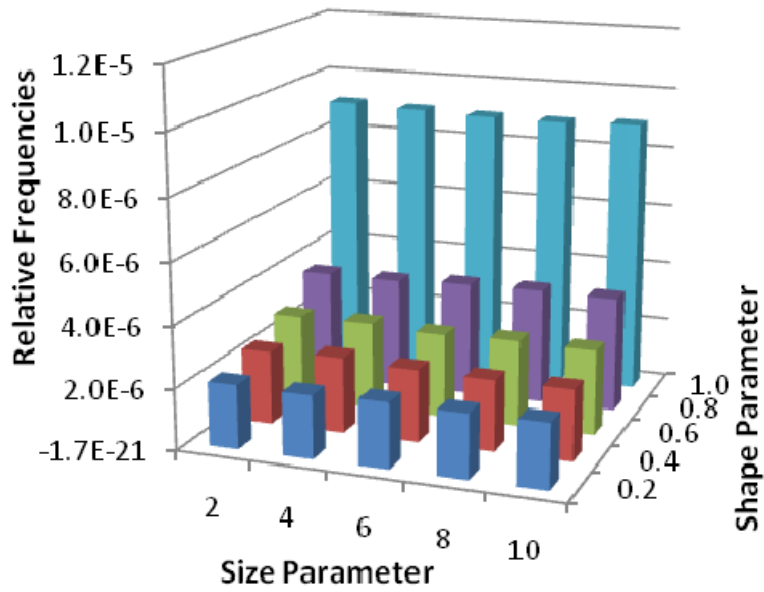
To simulate the measurements that would be obtained by the sectioning process, horizontal section cuts were applied at various heights within the cube, and the relative frequency of anomalies per unit area N_A was obtained for the size and shape parameters associated with each anomaly that appeared on the section plane. The values obtained from the section plane were converted using the Cruz-Orive unfolding algorithm to predict the size and shape distribution of the spheroids.

Table 12. Spheroid Parameters Associated with Application Example

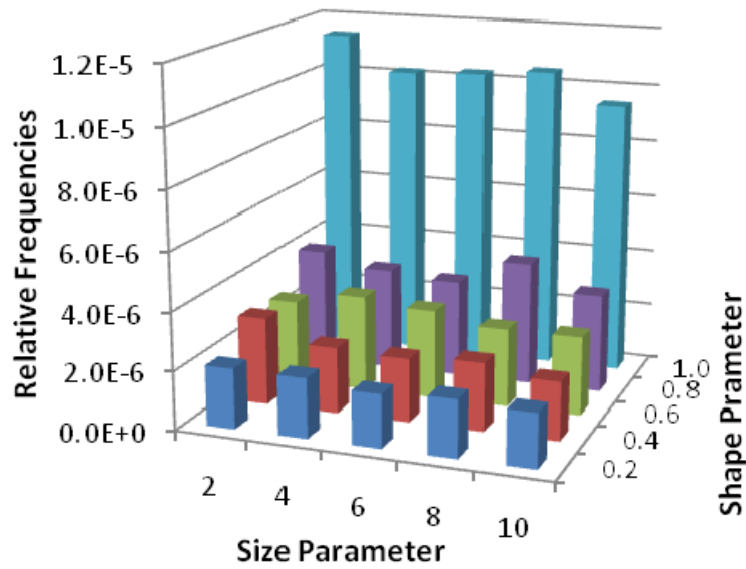
Variable	Description	Lower Bound	Median	Upper Bound	Distribution
a	major axis	0.0	5.0	10.0	Uniform
b/a	aspect ratio	0.0	0.5	1.0	Uniform
$\alpha_1, \alpha_2, \alpha_3$	orient. angles	0.0	π	2π	Uniform

Figure 13 shows the 3D histogram plots of the relative frequencies of the actual population of spheroids and the predicted population based on measurements of their elliptical profiles on 98 planar sections. The predicted results have reasonable agreement with the actual distributions. Computational accuracy improves with the increasing number of sections, as expected, due to the increased total number of Monte Carlo samples associated with the additional sections. The influence of the number of section plane measurements on predicted spheroid size parameter and shape parameter values is shown in Figures 14 and 15, respectively for a 10×10 grid and a 5×5 grid. For both parameters, predictions were significantly improved when the number of sections was increased from 1 to 10, but increasing the number of sections by another order of magnitude (*i.e.*, from 10 to 100) had only a marginal improvement on prediction accuracy. This suggests that there may be an optimum number of sections that provides a good balance between computational accuracy and the number of sections (and associated costs).

Generally, the errors associated with the stereological unfolding algorithm come from two primary competing sources: statistical error (*i.e.*, not enough Monte Carlo samples) and discretization (*i.e.*, bin size) error. Discretization error decreases with increasing number of bins, while statistical error increases with increasing number of bins. The bin size should not be too large or too small. There is an optimal discretization parameter that minimizes the total error (Ohser and Sandau, 2000). In practical experiments, the number of sections is limited and data noise often dominates, so the discretization error is generally insignificant compared with statistical error. For example, the accuracies of the results using 5×5 bins are comparable to those with 10×10 bins, if not better. Therefore, the focus should be on reducing statistical error in practical applications. It is important to have a sufficient number of samples in each bin to have small statistical errors. Statistical error is smaller if measurements are done on more planar sections, or if the material has a higher density of spheroid centers and the spheroids are larger. However, there is a maximum limit on the density of spheroids for the Cruz-Orive stereological unfolding algorithm because this algorithm assumes that the spatial distribution of spheroids is uniform and dilute. In practice, “dilution” is satisfactory whenever the volume fraction of the spheroids to the total volume is less than about 10% (Cruz-Orive, 1977). This condition is required to assume that the set of spheroid centers approximately forms a “Poisson ensemble” in three dimensions.

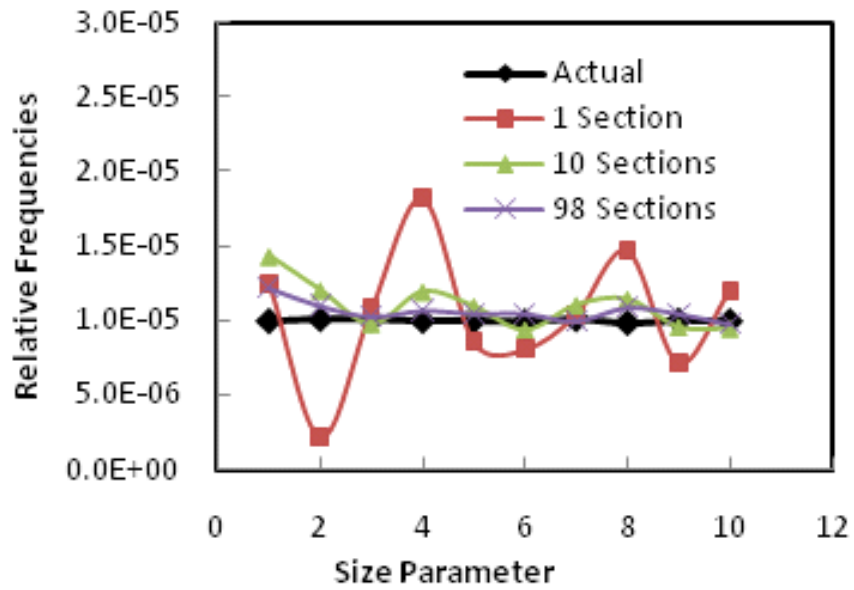


(a)

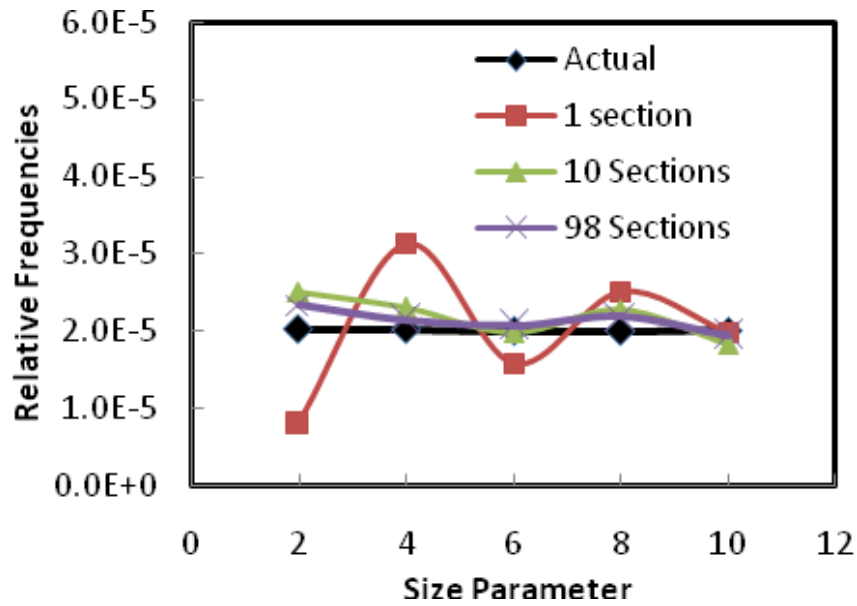


(b)

Figure 13. Bivariate histograms (stereograms) of anomaly size and shape parameter associated with anomalies in the fictitious material: (a) original population of spheroids, and (b) predicted population of spheroids based on sectioning data transformed using the Cruz-Orive unfolding algorithm.

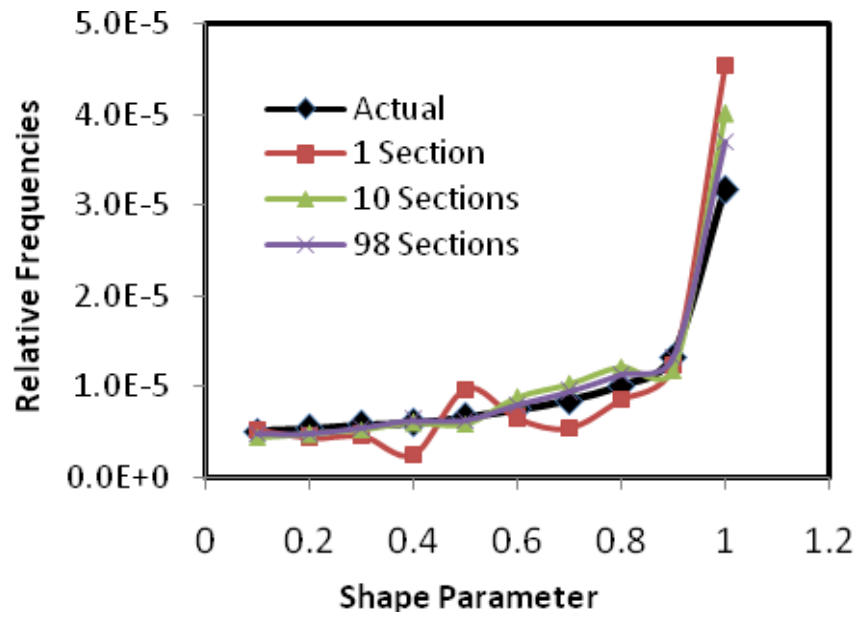


(a)

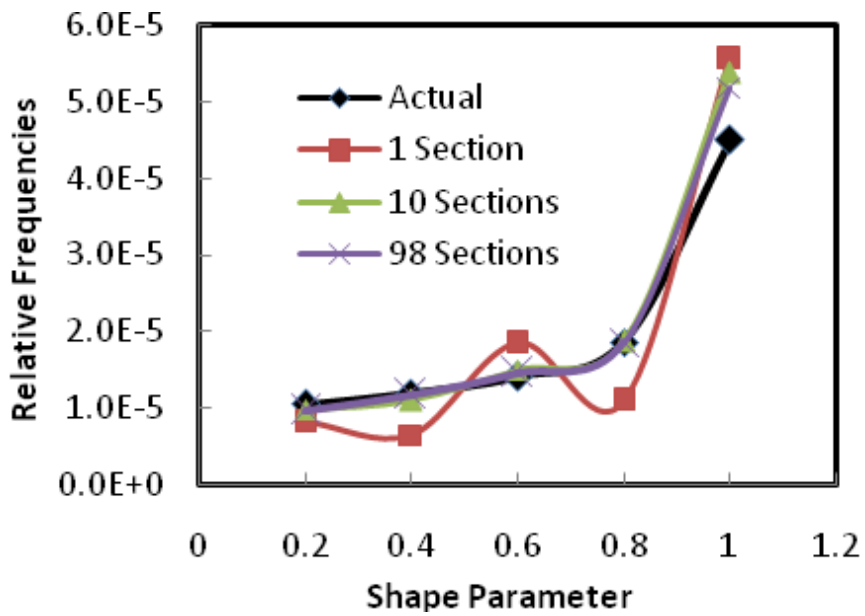


(b)

Figure 14. Influence of the number of section plane measurements on predicted spheroid size parameter values: (a) 10×10 bin grid, and (b) 5×5 bin grid.



(a)



(b)

Figure 15. Influence of the number of section plane measurements on predicted spheroid shape parameter values: (a) 10×10 bin grid, and (b) 5×5 bin grid.

3.2.5 Discussion

As mentioned in Section 3.2.1, it currently is impossible to accurately predict the shape and orientation parameters of a general ellipsoid based on measurements obtained from 2D sectioning data. If data are available in another form, such as HLS, then it may be possible to predict general ellipsoid parameters by combining the data using Bayesian updating or a similar method. On the other hand, if data are only available from 2D sectioning, then a general ellipsoid model is probably not an appropriate one because it simply cannot be fully characterized. In this situation, the anomaly model should be limited to either the prolate or oblate spheroid model.

In this study, an unfolding algorithm was implemented and verified that can be used to estimate the dimensions and orientations of 3D spheroids based on 2D sectioning measurements. It was shown that the accuracy of the predicted spheroid model is dependent on the number of sections and the discretization of the mesh used to characterize the data. In section 2.1.1, it was mentioned that the unfolding algorithm developed by Ghosn *et al.* (2003) performed well for some mesh sizes and not so well for others. This difference may possibly have been due to the number of sections or the discretization bin width.

In some instances, the number of sections may be a fixed quantity (*e.g.*, historical data). In this case, the unfolding algorithm could be used to quantify confidence bounds on fracture risk associated with the uncertainty in the spheroid model for the fixed number of sections. For new design, the number of sections is probably limited by the cost to obtain them. In this situation, the unfolding algorithm could be used to identify the minimum number of sections that would be required to meet a fracture risk reliability target that accounts for the uncertainty associated with the number of sections. In addition, since DARWIN includes a capability to quantify the influences of manufacturing and service inspections on fracture risk, it could be used to extend the cost tradeoff to include the cost of inspection. This would allow the engineer to identify the best combination of testing (sectioning) and inspections to minimize overall life-cycle cost.

The unfolding algorithm used in this study was limited to spheroid dimensions and orientations that were modeled as independent random variables. GRC studies have shown that anomaly dimensions are strongly correlated variables, so this influence would need to be considered before implementing an unfolding algorithm in DARWIN.

3.3 Algorithms for Modeling the Growth Rates of Small Fatigue Cracks

3.3.1 Introduction

The tendency for small fatigue cracks to grow at rates faster than anticipated from large-crack data trends and/or to grow at stress intensity factor ranges below the usual large-crack threshold has long been noted, and a variety of reasons have been proposed (McClung *et al.*, 1996; Davidson *et al.*, 2003).

GRC measured the growth rates of small fatigue cracks in Udimet 720 and compared the results with large-crack behavior (Telesman *et al.*, 2006). Their initial comparison suggested that classic small-crack behavior was observed, including high initial crack growth rates and large scatter. Many cracks exhibited decreasing crack growth rates and some arrested completely. Few small cracks grew to become dominant cracks with increasing crack growth rates. However, further examination of the data revealed that much of the characteristic “small crack” behavior was associated with “pop-in” behavior during the first 250 cycles. When data from this initial crack formation and growth period were removed, the remaining data often fell at or below the extrapolated Paris line, and some of the classic “small crack” behavior was no longer apparent.

In research (currently unpublished) funded by the FAA, the current authors have recently surveyed small-crack behavior in a variety of common gas turbine engine rotor materials. Small-crack data were collected from the literature and (when possible) from related private communications with the experimentalists who generated the data. The specific rotor materials included Ti-6Al-4V, Ti-6Al-2Zr-4Sn-6Mo, IMI685, IN-100, and Astroloy. Classic small-crack effects were observed in every case.

The pragmatic engineering challenge is not only to predict when this “anomalous” small-crack behavior will occur, but to predict the actual growth rates of small fatigue cracks on the basis of large-crack data and other appropriate parameters (but without actually having to generate fatigue crack growth (FCG) rate data for small cracks, since this is typically an expensive effort). The FAA-funded study critically evaluated one simple engineering model that can be used to correlate small-crack behavior with corresponding large-crack behavior.

A brief study was conducted in the present project to extend this survey of small-crack behavior to the GRC U720 data, and to evaluate the same engineering model using the U720 data.

3.3.2 Analysis Methods

Two types of crack growth data analysis methods require delineation. The first method is that used to calculate the average crack growth rate, da/dN , from measured crack length vs. cycles data. In this study, a direct secant method that calculates the slope between each two adjacent (a, N) pairs was used. The second method is that used to calculate the stress intensity factor range from the crack size and applied stress range. The U720 small-crack data were generated with small cylindrical specimens under uniform remote axial tension. The surface crack depth was estimated to be equal to half of the measured surface length, and the Forman-Shivakumar (1986) solution for a thumbnail crack in a solid cylinder (also available in NASGRO as the SC07

solution) was used to calculate the stress intensity factor. This solution was used for consistency with the other data analysis performed in the FAA-funded effort.

A wide variety of different analysis methods have been proposed to calculate an enhanced crack driving force for small cracks and hence to predict their accelerated growth rates compared to large cracks with the same nominal driving force. The purpose of this small study was to investigate one simple method that has shown some promise in earlier studies. The method was originally proposed by El Haddad *et al.* (1979) based on the so-called Kitagawa (Kitagawa and Takahashi, 1976) diagram construction, Figure 16. The Kitagawa diagram integrates the traditional large crack fracture mechanics threshold, ΔK_{th} , with the traditional smooth specimen endurance limit, $\Delta\sigma_e$. The region on the Kitagawa diagram both above the horizontal endurance limit line and above the sloping threshold line is “unsafe” because fatigue failure is predicted to occur. The region below both lines is “safe” because fatigue failure is predicted not to occur. The intersection of the two lines, defined as a_0 , is given by the equation:

$$a_0 = \frac{1}{\pi} \left(\frac{\Delta K_{th}}{F\Delta\sigma_e} \right)^2 \quad (24)$$

where, for consistency with the smooth specimen endurance limit data, $F = 0.67$ is the geometry correction factor in the K solution for the semi-circular surface crack in the smooth specimen.

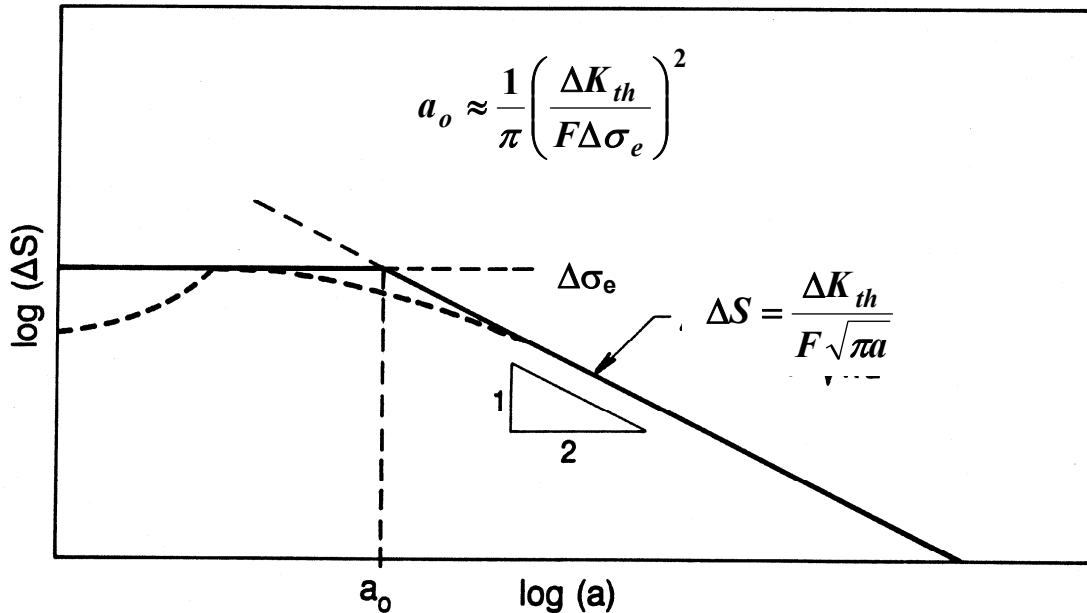


Figure 16. Schematic Kitagawa diagram relating smooth specimen fatigue endurance limit ($\Delta\sigma_e$) and large-crack threshold (ΔK_{th}).

The Kitagawa diagram indicates that cracks smaller than a_0 must be able to grow at nominal stress intensity factor ranges that are less than the large crack threshold, since smooth specimens fail by the initiation and growth of microcracks to failure in this regime. El Haddad suggested that small cracks could grow below the large-crack threshold because the effective driving force of the small cracks was larger than expected from traditional large-crack fracture mechanics. He proposed that the actual “equivalent” driving force could be calculated by replacing the physical crack size a with the sum $(a + a_0)$ according to the relationship:

$$\Delta K_{eq} = F(a)\Delta S\sqrt{\pi(a + a_0)} \quad (25)$$

Here $F(a)$ is the crack shape and specimen/component geometry correction factor for the geometry of interest; a_0 is not included in the $F(a)$ calculation. Note that the a_0 contribution is negligible for large values of a , but becomes increasingly significant for smaller values of a .

Although the El Haddad (EH) concept has been criticized for its apparent lack of physical justification, several researchers have independently derived similar formulations based on detailed micromechanical considerations, and these have been shown to be numerically identical to the EH formulation under typical conditions. Chan (1999) related a_0 to dislocation pileups and mode II shear cracks, and found satisfactory agreement with small-crack data from titanium aluminides. Tanaka *et al.* (1981) formulated the problem in terms of a crack-tip slip band propagating across one or more grain boundaries, and demonstrated reasonable agreement between his formulation and a variety of experimental data, mostly for steels and aluminum alloys.

3.3.3 Results

The ability of the EH small-crack model to correlate small-crack and large-crack data is first illustrated by showing some of the data evaluated in the FAA-funded study.

Lenets *et al.* (2000, 2002) at Honeywell and Caton *et al.* (unpublished) at the AFRL tested Ti-6Al-4V from a common material source. The Ti-6Al-4V was provided in a solution-treated and over-aged (STOA) condition. The microstructure consisted of 60 volume percent primary alpha phase and 40 volume percent lamellar transformed beta phase. The grain structure was equiaxed and uniform with an average alpha grain size around 10 μm (0.0004 in.).

Both sets of small-crack tests were conducted on smooth cylindrical specimens at room temperature. Lenets *et al.* and Caton *et al.* both conducted tests at $R = 0.1$ and $R = 0.5$, and Caton *et al.* also conducted tests at $R = -1$. The small surface cracks in the Caton *et al.* tests were initiated at focused ion beam (FIB) micro-notches roughly 30 – 40 μm wide, 15 – 20 μm deep, and 3 – 4 μm high. The small surface cracks in the Lenets *et al.* tests were initiated naturally. Crack growth was monitored in both laboratories with standard cellulose acetate replication methods. Large-crack data had been generated at the same stress ratios with the same material using both compact tension and surface-crack tension specimens (Sheldon *et al.*, 1999; Boyce and Ritchie, 2001).

Comparisons of the small-crack and large-crack growth rate data for the HCF program Ti-6Al-4V are shown in Figure 17 for stress ratio $R = 0.1$. The data exhibited a pronounced small-crack effect at the smallest crack sizes, growing faster than the corresponding large-crack trends.

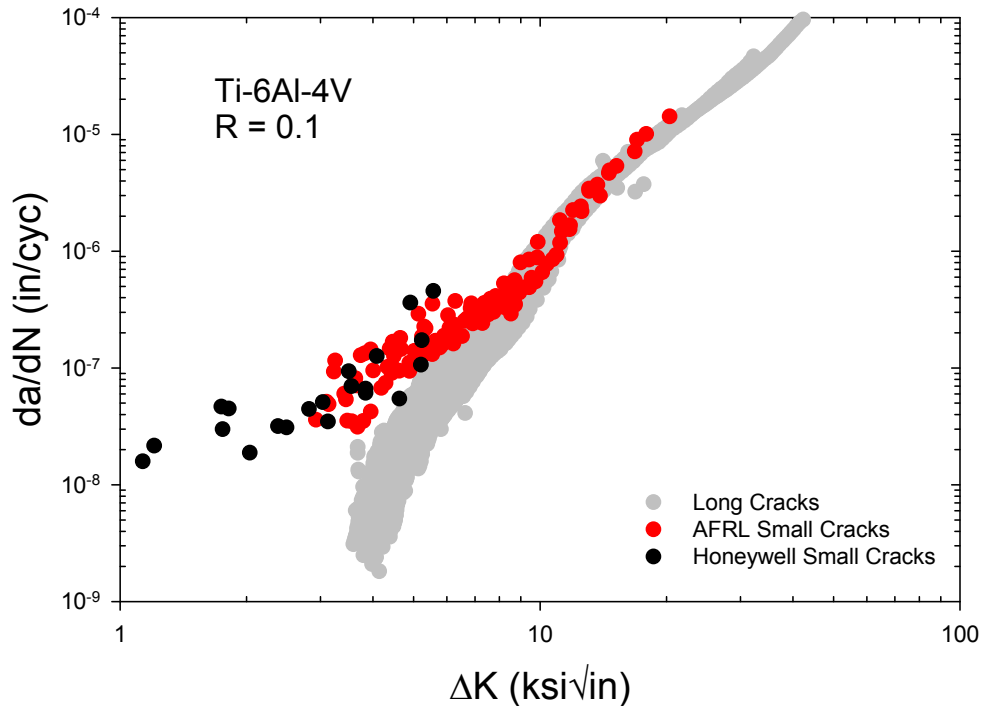


Figure 17. Comparison of small-crack and large-crack growth rate data for Ti-6Al-4V tested by Lenets *et al.* and Caton *et al.* at $R = 0.1$.

The EH small-crack parameter a_0 was calculated to be $a_0 = 0.0021$ in. ($53 \mu\text{m}$) from Eqn 1 based on available large-crack threshold and smooth-specimen endurance limit data for the same material. The El Haddad-corrected values of ΔK were then calculated from Eqn 2 for all data. The results are shown for $R = 0.1$ in Figure 18. Following the EH correction, the small-crack data agree very closely with the large-crack data trends. Similar correlations (not shown here) were successful at $R = 0.5$ and $R = -1$, although the available data were more limited.

Jha *et al.* (2008) performed large-crack and small-crack tests at 650°C (1200°F) with the nickel-based superalloy IN-100. The material was fine-grained, subsolvus, and powder-processed with a median γ -grain size about $4 \mu\text{m}$ (0.00016 in.). The yield strength at the test temperature was about 1100 MPa (160 ksi), the UTS was about 1379 MPa (200 ksi), and the % elongation at fracture was about 20%.

Small-crack tests were performed at $R = 0.05$ using mostly cylindrical smooth specimens under uniform tension (one test was conducted with a square bar under bending). Some cracks originated naturally at non-metallic particles on the surface, while other cracks initiated naturally at surface pores. Crack length measurements were performed with acetate replicas at room temperature during interruptions in the test. Large crack da/dN vs. ΔK data were generated with C(T) specimens.

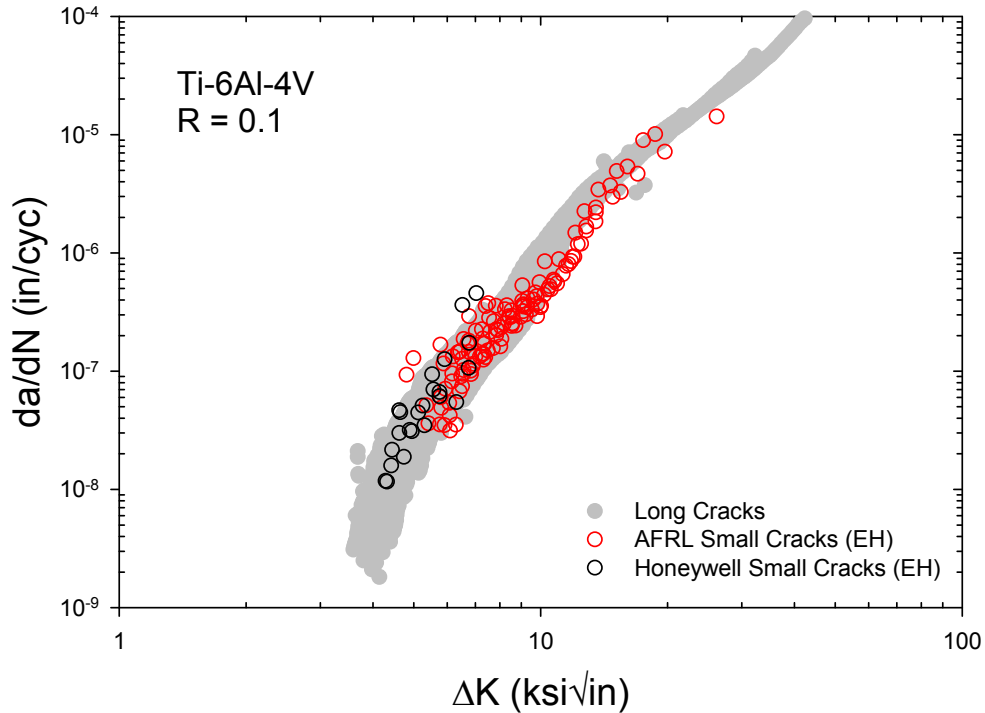


Figure 18. Comparison of small-crack and large-crack growth rate data for Ti-6Al-4V tested by Lenets *et al.* and Caton *et al.* at $R = 0.1$, with small-crack data adjusted using El Haddad parameter.

Two approaches were used to estimate the EH parameter, one based on Eqn. (24) and one based on scaling the grain size. The large-crack threshold was measured to be $12.3 \text{ MPa}\sqrt{\text{m}}$ from a single reported large-crack test. Estimating the “endurance limit” was difficult because smooth-specimen fatigue tests ($R = 0.05$) were only conducted at maximum stresses of 1000 MPa, 1100 MPa, 1150 MPa, and 1200 MPa. At the lowest stress level tested, failures were observed at lives ranging from 60,000 cycles to nearly 1,000,000 cycles. The earlier failures were mostly associated with crack initiation at subsurface non-metallic particles. The longer lives (300,000 to 950,000 cycles) were mostly associated with crack initiation at surface pores, which is thought to be more relevant to the EH estimate. Based on extrapolation of the available failure data for surface pore cracks, the endurance limit was crudely estimated to be about $\Delta\sigma_e = 900 \text{ MPa}$. This estimate and the measured large-crack threshold led to an estimated EH parameter $a_0 = 132 \text{ }\mu\text{m}$ (0.0052 in.). An alternative value was calculated by scaling the median γ -grain size: six times this dimension is $24 \text{ }\mu\text{m}$ (about 0.001 in.). The earlier studies of small-crack behavior in titanium rotor alloys had found six-times-grain-size to be a reasonable estimate of the EH parameter.

Comparisons of the large-crack and small-crack data are shown in Figure 19, and comparisons of large-crack data and EH-corrected small-crack data are shown in Figure 20. The EH estimate based on Eqn. (24) over-predicted the small-crack effect (compared to the available large-crack data), while the EH estimate based on scaling the median γ -grain size slightly under-predicted the small-crack effect.

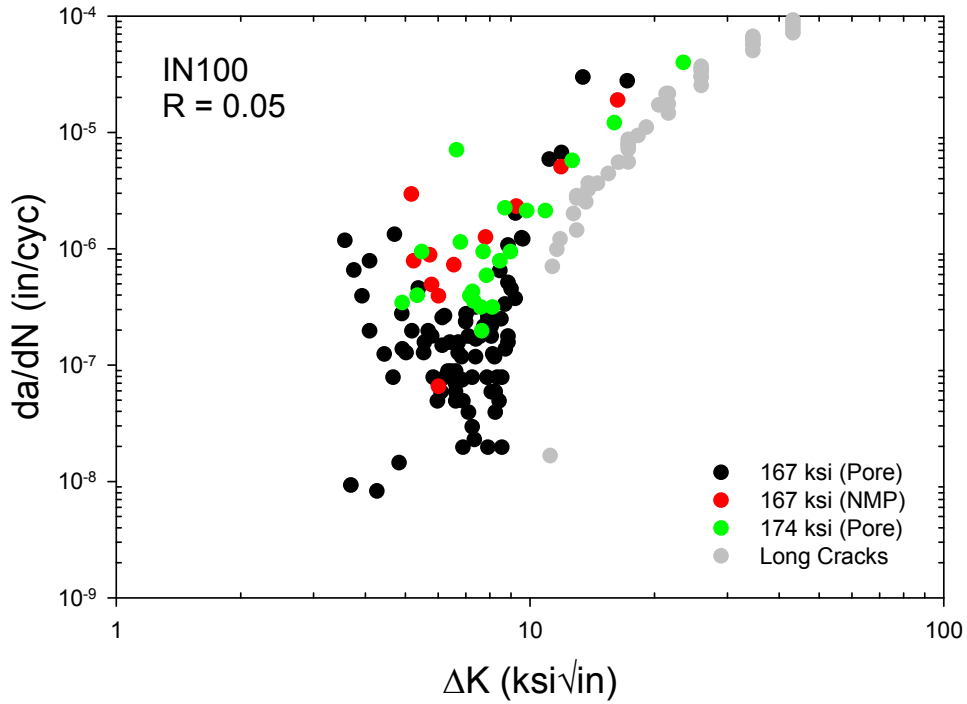


Figure 19. Comparison of small-crack and large-crack growth rate data for IN-100 tested by Jha *et al.* at $R = 0.05$.

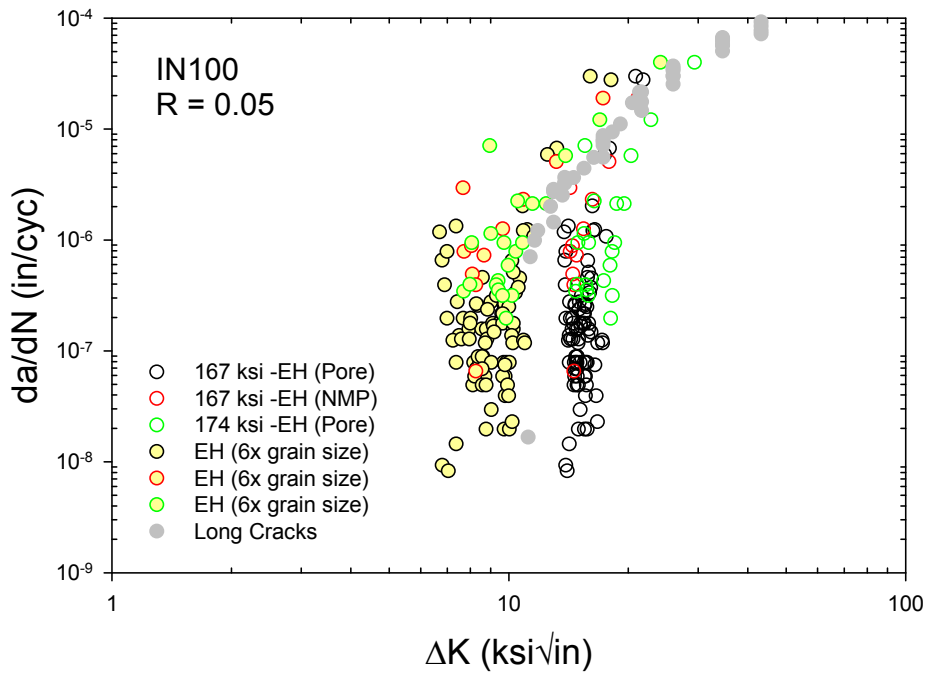


Figure 20. Comparison of small-crack and large-crack growth rate data for IN-100 tested by Jha *et al.* at $R = 0.05$, with small-crack data adjusted using two estimates of the El Haddad parameter.

Consider now the GRC U720 data. The GRC small-crack tests were performed at 1200°F (650°C) on cylindrical, axially-loaded fatigue specimens with a 0.40-inch (10.2 mm) diameter. All cracks were initiated naturally at artificially-seeded ceramic inclusions with average seed diameters of 0.0021 in. (54 μm) or 0.0048 in. (122 μm). Crack size measurements were performed in a special rotational stage in a scanning electron microscope. Fatigue cycling at 20 cpm in ambient laboratory air was periodically interrupted and the specimen transferred to the SEM stage to map and track surface crack growth. The fatigue cycling was initially performed under strain control at 20 cpm (0.33 Hz) with strain ratios of $R_\epsilon = 0$ or -1 under strain ranges of 0.6% or 0.8%. Following an initial cycling period during which maximum and minimum loads stabilized, testing continued to failure under load control at a frequency of 5 Hz. The corresponding small-crack load ratios were approximately $R = -0.33$ or $R = -1$. The maximum stresses in the small crack tests varied from 154 ksi to 163 ksi for $R = -0.33$ and from 107 ksi to 109 ksi for $R = -1$.

GRC provided an extensive data base of small-crack results to SwRI, and only a representative selection of these tests were included in this study. Specifically, $R_\epsilon = 0$ specimens included were 5776-C-L17, 5776-J-L22, 5776-D-L3, and 5776-H-L21. The $R_\epsilon = -1$ specimens included were 5776-C-L2, 5776-D-L18, 5776-H-L14, and 5776-J-L5. Furthermore, data from the first 250 cycles of fatigue testing (the so-called pop-in period) were excluded from this study.

Large-crack tests were performed for comparison under load control at 1200°F with so-called Kb bar (surface crack) specimens at $R = -0.25$ or -1 . Comparisons of large-crack and small-crack data (with and without EH corrections) are shown in Figures 21 and 22 for $R = -0.33$ and Figures 23 and 24 for $R = -1$. Since endurance limit data were not available, the EH parameter was again estimated by scaling the average grain size (8 μm) by a factor of six.

Even after excluding the data from the pop-in period, the remaining small-crack data still exhibited classical small-crack effects, growing at ΔK values smaller than the large-crack threshold, and growing at rates faster than large-crack trends. The EH correction was generally successful in correlating large-crack and small-crack data at $R = -0.33$. At $R = -1$, the EH correction under-corrected the small-crack data relative to the large-crack data, although it did successfully consolidate the small-crack data. Unfortunately, only near-threshold small-crack data were available.

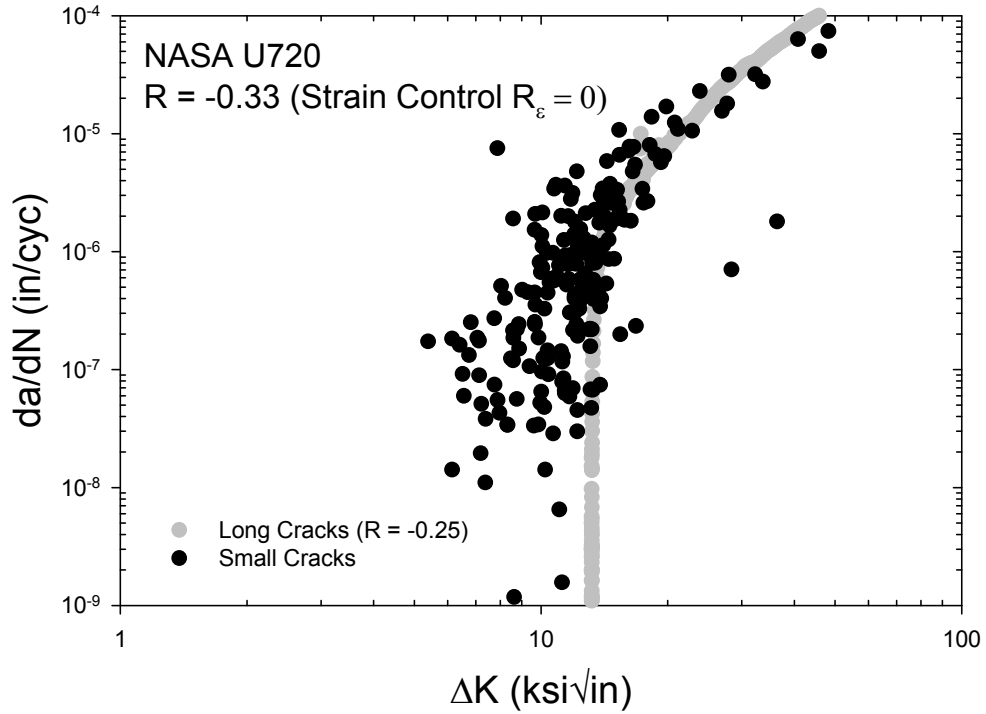


Figure 21. Comparison of small-crack and large-crack growth rate data for U720 at $R = -0.33$.

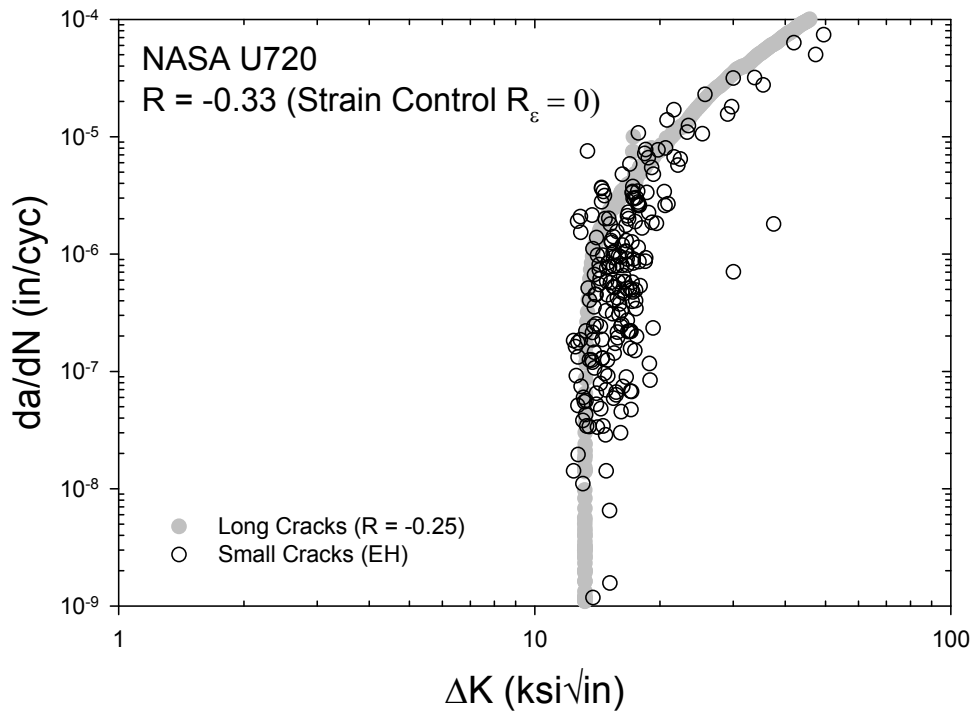


Figure 22. Comparison of small-crack and large-crack growth rate data for U720 at $R = -0.33$, with small-crack data adjusted using El Haddad parameter.

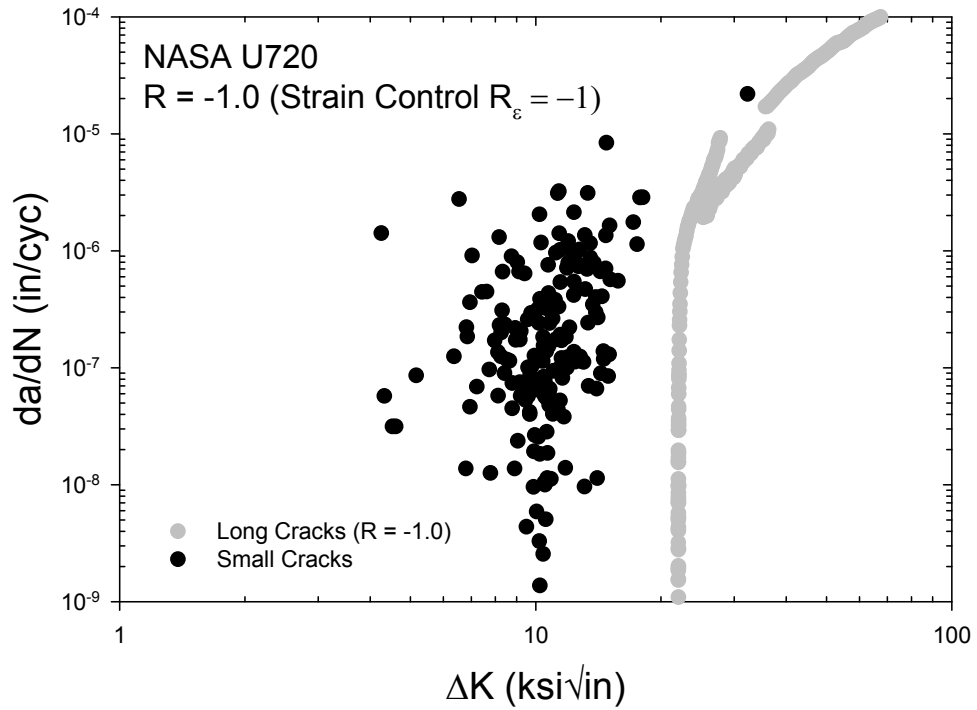


Figure 23. Comparison of small-crack and large-crack growth rate data for U720 at $R = -1$.

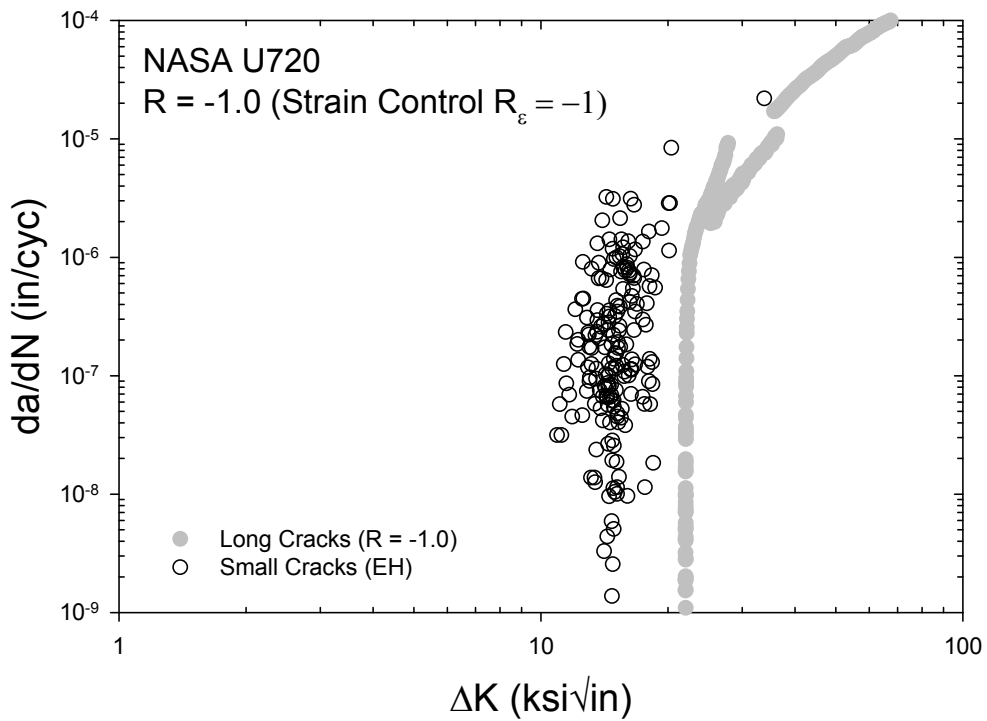


Figure 24. Comparison of small-crack and large-crack growth rate data for U720 at $R = -1$, with small-crack data adjusted using El Haddad parameter.

3.3.4 Discussion

There are several practical difficulties associated with the El Haddad approach when a_0 is estimated from Eqn. (24). For example, it is sometimes difficult to define an “endurance limit” for some materials. Studies during the last two decades in the high cycle fatigue and very high cycle fatigue regimes have indicated that many materials do not exhibit a distinct plateau in fatigue strength at very long lives, but that the fatigue strength may continue to decrease with further cycling. A stated “endurance limit” may merely reflect the limits imposed on fatigue test duration. A shorter test duration may lead to an overestimate of the endurance limit, which will give an underestimate of the EH parameter, and potentially an underestimate of small-crack growth rates.

In addition, it is sometimes observed that the failure mode for smooth specimen fatigue tests may shift from surface initiation to subsurface initiation at very long lifetimes. Since Eqn. (24) requires some assumption about the crack geometry of interest, a shift from a surface crack to an embedded crack will require a change in the formulation (and may introduce a discontinuity or conflict between data derived from different failure modes). Eqn (24) as written above is applicable only to endurance limits associated with surface failure modes. The failure origins associated with high cycle fatigue specimens are not always reported. If the endurance limit for surface crack behavior is estimated to be too low because it is influenced by subsurface failures at longer lives, then the EH parameter may be estimated to be too large, thereby overestimating small-crack growth rates.

Furthermore, fatigue failure behavior in some materials may be controlled by populations of inclusions, and the life-limiting crack in a specimen may be associated with a particularly large defect. Any effect of this defect on the growth (or non-growth) of microcracks (associated, for example, with local stress concentrations or residual stresses) is not reflected in the formulation behind Eqn. (24). In some cases, the defect may be sufficiently large that the initial resulting microcrack is larger than a_0 , thereby raising additional questions about the formulation. If the intended goal of the EH small-crack formulation is to describe crack growth behavior in normal matrix material, then properties derived from defect-dominating behavior may be inappropriate. However, if the cracks of interest in the material always arise from such defects, then the formulation may end up being self-consistent.

A different set of difficulties are associated with characterization of the large-crack threshold, the other key input into Eqn. (24). It is now known that the apparent large-crack threshold can be influenced both by test technique (*e.g.*, traditional load-shedding methods) and specimen geometry (large-crack thresholds generated with C(T) specimens are sometimes observed to be significantly higher than with M(T) specimens). The most common error appears to be an overestimation of ΔK_{th} based on C(T) tests at $R \approx 0$ using traditional load-shedding methods. Underestimation of ΔK_{th} appears to be less likely. An overestimate of ΔK_{th} will contribute to an overestimate of a_0 and an overestimate of small-crack growth rates.

Another complication associated with the large-crack threshold is that other environmental factors may influence the apparent value of this threshold (for example, if corrosion product builds up on the crack faces and causes premature arrest due to oxide-induced crack closure).

There may also be environmental influences on small surface cracks in service, but there may not be adequate similitude between the threshold test configuration and the small-crack configuration for the threshold data to be transferable to the EH calculation. Again, an overestimate of ΔK_{th} would lead to an overestimate of small-crack growth rates by the EH model.

Given these difficulties associated with obtaining appropriate input data to estimate the EH parameter, it is encouraging that some success was observed using microstructurally-motivated estimates of a_0 . It may also be practical to use totally empirical estimates of a_0 in some cases, as was also done here in a few cases. However, the more empirical the estimate, the greater is the need for adequate small-crack growth rate data to validate the estimate.

The physical meaning of the EH length parameter also deserves some further discussion. El Haddad originally considered a_0 to be an intrinsic crack length in the microstructure. Such an interpretation is troublesome, however, since a_0 is on the order of several grain diameters. The FCG threshold value for small cracks is known to increase with crack length, approaching the long-crack value when the crack becomes large. A more reasonable and physically appealing interpretation for a_0 is simply that it describes the length scale where the FCG threshold of the small crack approaches that of the large-crack threshold.

4.0 PROGRAM PLAN FOR FUTURE RESEARCH

One of the primary objectives of the current study was to identify technologies for assessment of P/M materials developed at GRC that could be transferred for use by gas turbine engine manufacturers. Based on the GRC status summary and the DARWIN capabilities summary, several technology gaps were identified related to (1) characterization and simulation of 3D anomalies based on data from different types of inspections, (2) understanding and analysis of anomaly deformation and breakup during the forging process, and (3) treatment of various factors that can influence fatigue crack growth lives. A program plan for the development and implementation of key algorithms and software modules in DARWIN to address the technology gaps has been developed and is described in this section.

Pre-Processing Module for 3D Anomalies. Over the past decade, GRC pioneered a number of studies that focused on methods for measuring 3D anomalies in P/M materials anomalies. Several methods were identified for anomaly characterization, including direct measurement of the three orthogonal axes of anomalies recovered using the heavy liquid separation process (HLS), and indirect measurement of these dimensions based on data from sectioning and fractography. 3D anomalies are simulated in DARWIN using six independent random variables based on three orientation angles and the dimensions of the primary axis and two aspect ratios for the remaining two orthogonal axes. A software module is needed to convert the data from anomaly measurements into the format that is used in DARWIN. For HLS data, the module would convert anomaly major and minor axis measurements into anomaly primary axis and aspect ratios. For data from sectioning or fractography, the module would convert the data from 2D measurements into 3D anomaly dimensions/orientations using the unfolding algorithm described previously. Since the number of sections probably will be limited, DARWIN would need to be enhanced to quantify confidence bounds on fracture risk associated with the uncertainty in the spheroid model for the limited number of sections. Note that HLS measurements do not provide any information regarding the orientation or breakup of anomalies due to the forging process. On the other hand, 3D ellipsoids cannot be fully characterized based on data from sectioning or fractography. A Bayesian updating algorithm is therefore envisioned that would combine data from the various test data sources into a common set of variables for use in numerical simulations. DARWIN would also be enhanced to display fracture risk confidence bounds reduction associated with use of combined data from the various test data sources.

Pre-Processing Module for Failure Data from Multiple Anomaly Types. As mentioned in Section 3.1, one of the challenges associated with modeling P/M materials is that the materials—and the test specimens (particularly unseeded specimens)—typically contain multiple types of anomalies that can cause fatigue failure. Under this project, a method was developed for estimating the marginal CDFs associated with individual anomaly types, using an approach based on the nonparametric statistical model of Kaplan-Meier (1958) combined with the data smoothing algorithm proposed by Meeker and Escobar (1998). This method was documented in Section 3.1. Although the approach has been demonstrated using real failure data, some effort would be required to implement the algorithm in DARWIN. It is envisioned that this would be implemented in a separate module that would be used to preprocess the raw failure data into a form that could be used directly in DARWIN.

Probabilistic Simulation of 3D Anomalies. The current version of DARWIN is limited to simulation of uncorrelated random variables. However, GRC studies suggest that the anomaly dimensions could be highly correlated random variables, and anomaly orientations could be correlated to additional random variables related to forging strain. DARWIN enhancements would be required to model these relationships among the various anomaly dimensions and orientations. One of the key challenges with the use of correlated random variables to represent anomaly dimensions is that it may be difficult to visualize the relationships among the crack dimensions in the fracture plane. Further DARWIN enhancements would be required to provide GUI visualization of 3D anomalies at user-specified fracture planes.

Identification of Life-Limiting Anomaly Orientation. To estimate the fracture risk of disk materials, the analyst is typically faced with identifying the minimum life location in a component. Since the minimum life location is dependent on a number of factors, such as the orientation of the fracture plane, the projected area of the anomaly on the fracture plane, and local constraint changes associated with crack transitions, it may be difficult to identify. Fortunately, DARWIN enhancements such as life contours and risk contours are under development, and these will assist the user with identifying the location once a fracture plane has been selected. However, the user will still need to identify the orientation of the fracture plane, and there is no guarantee that it will be conservative. Anomaly orientation may also influence the life-limiting location within a component. An algorithm is therefore needed in DARWIN that will automatically identify the life-limiting anomaly orientation.

Small-Crack Modeling. Small-crack behavior has been identified as being potentially significant for accurate lifing of P/M materials. The current DARWIN software does not include any special treatment of small-crack behavior, either in terms of accelerated growth rates (from a deterministic perspective) or in terms of greater scatter in possible growth rates (from a probabilistic perspective). As noted in Section 3.3, SwRI has been investigating a simple model for deterministic small-crack growth rate behavior under FAA funding (a model which showed some promise for P/M U720), and it is possible that this particular model might be implemented in the FAA project. Investigation/development/implementation of alternative models would require additional funding. The current DARWIN model for life scatter is independent of crack size, and there are no current plans in the FAA project to develop and implement alternative probabilistic models for scatter in small-crack growth rates. Therefore, this would require additional work.

Analysis of Forging Effects. Previous GRC studies with P/M materials have indicated that the size, orientation, and behavior of inherent anomalies may be significantly influenced by the forging process. Several of the aircraft engine manufacturers have expressed interest in exploring this phenomenon, and the U.S. Air Force has recently funded research programs related to the topic. SwRI will participate in two studies, one a Small Business Innovative Research (SBIR) project in partnership with Scientific Forming Technologies Corporation (SFTC), and the other as a subcontractor to Pratt & Whitney (P&W). The SFTC study will focus on linking the SFTC DEFORM software with DARWIN, with the initial phase focused on the transfer of forging residual stress data from DEFORM to DARWIN. Future phases, if funded, would consider additional variables such as anomaly size and orientation as well as microstructural information. The SwRI effort for the P&W study will also use DEFORM data to model the influence of the

forging process on anomaly orientation. Since the USAF has funded only very specific features, it is anticipated that further funding may be required to combine the various features related to forging effects into a comprehensive toolset that will be of use to the general DARWIN user.

Residual Stress Issues. A number of residual stress issues are relevant to P/M lifing. As noted in the earlier Status Summary (Section 2.2), DARWIN currently has a basic capability to superimpose a user-provided residual stress gradient with 2D finite element model stress results for a single crack geometry. Some additional work is planned under the current FAA grant to extend this capability to additional crack geometries and additional analysis modes. Further effort would be required to address a complete set of crack geometries and analysis modes. As noted in the previous paragraph, SwRI is currently working with SFTC to develop a new DARWIN capability to read DEFORM results files for forging (bulk) residual stresses and superimpose these with DARWIN service stresses, and this effort should be completed if the SBIR funding continues. Additional work remains to develop and implement predictive models for local residual stresses (*e.g.*, machining residual stresses, or residual stresses arising from differential thermal expansion of inclusions) and for the significant relaxation and redistribution of residual stresses that can occur in service due to both thermal and mechanical mechanisms.

Other Issues. The development of DARWIN has been funded primarily by the FAA, and the existing features reflect the priorities of the FAA, RISC, and the Industry Steering Committee. There are a number of issues that influence fracture risk that are not addressed in the current project, and due to competing FAA priorities, probably will not be completed in future FAA projects. For example, an approach is needed to model anomalies that intersect the free surface of the component. In the current version of DARWIN, the free surface is assumed to intersect the midpoint of the anomaly, but an approach is needed to model intersections at various anomaly locations to simulate the volume of material that is removed by the machining process.

Modeling of the crack formation life is another critical area of need for DARWIN. Currently, DARWIN provides no internal models for predicting the formation/nucleation/initiation life. It instead provides a software link to a separate user-supplied crack formation module that provides only limited treatment of the crack formation life. Additional work is needed to develop general crack formation modeling capabilities, or to expand the existing software link to include other important variables that the user may wish to consider in their own crack formation module.

The implementation of formal algorithms in DARWIN necessarily requires validation of the engineering models, which is commonly achieved by comparison to actual test data. Verification of the software algorithms is also required to confirm that the engineering models are implemented in the intended form, and a standardized procedure has been developed at SwRI to accomplish this task. It is essential to include verification and validation (V&V) activities in any future task funded to enhance DARWIN for P/M lifing. GRC has generated extensive test data on the behavior of inclusions in P/M materials and the resulting effect on fatigue life, and these data should prove invaluable in future V&V activities.

(This page intentionally left blank.)

5.0 SUMMARY

Southwest Research Institute and NASA Glenn Research Center have worked independently in recent years on the development of probabilistic lifing methods for gas turbine engine rotor materials. This final report summarizes a brief investigation into the current status of relevant technology at SwRI and GRC with a view towards a future integration of methods and models developed by GRC for probabilistic lifing of powder metallurgy (P/M) nickel rotor alloys into the DARWIN software developed by SwRI. The current status of GRC data and models and the DARWIN software was reviewed in detail, and significant accomplishments/capabilities and technology gaps were identified. New algorithm development was conducted in three areas. First, a rigorous methodology for estimating anomaly distributions for materials in which multiple anomaly types are operative was developed and verified. Second, an unfolding algorithm that can be used to estimate the dimensions and orientations of 3D spheroids based on 2D sectioning measurements was implemented and investigated. Third, the behavior of small fatigue cracks in U720 tests conducted by GRC was investigated, and an existing model to predict small-crack behavior from large-crack growth rates was evaluated. Finally, a program plan was outlined for potential future research, identifying the most significant opportunities to address technology gaps and to develop needed new DARWIN capabilities.

(This page intentionally left blank.)

6.0 BIBLIOGRAPHY

- Aalan, O., 1978, "Nonparametric Estimation of Partial Transition Probabilities in Multiple Decrement Models," *The Annals of Statistics*, Vol. 6, No. 3, pp. 534-545.
- Aerospace Industries Association Rotor Integrity Subcommittee, 1997, "The Development of Anomaly Distributions for Aircraft Engine Titanium Disk Alloys," Proceedings 38th Structures, Structural Dynamics, and Materials Conference, Kissimmee, FL, pp. 2543-2553.
- Ang, A. H-S. and W. H. Tang, 1975, *Probabilistic Concepts in Engineering Planning and Design*, Vol. I, John Wiley, New York.
- Barrie, R. L., T. P. Gabb, J. Telesman, P. T. Kantzos, A. Prescenzi, T. Biles, and P. J. Bonacuse, 2008, "Effectiveness of Shot Peening in Suppressing Fatigue Cracking at Non-Metallic Inclusions in Udimet[®] 720," *Materials Science and Engineering A*, Vol. 474, pp. 71-81.
- Bonacuse, P. J., P. Kantzos, J. Telesman, T. Gabb, and R. Barrie, 2002, "Modeling Ceramic Inclusions in Powder Metallurgy Alloys," *Fatigue 2002*, Proc. 8th International Fatigue Congress, Stockholm, Sweden, Vol. 2, pp. 1339-1346.
- Bonacuse, P., L. Ghosn, J. Telesman, P. Kantzos, T. Gabb, and R. Barrie, 2003, "Modeling the Distribution in Fatigue Life from Inclusion Initiated Failures in PM Superalloys," 6th FAA/Air Force/NASA/Navy Workshop on the Application of Probabilistic Methods to Gas Turbine Engines, Solomon's Island, Maryland (presentation only).
- Bonacuse, P. J., P. Kantzos, J. Telesman, and T. Gabb, 2006, "A Refined Geometric Inclusion Model for Crack Initiation in Powder Metallurgy Alloys," *Fatigue 2006*, 9th International Fatigue Congress, Atlanta, Georgia, unpublished manuscript.
- Bonacuse, P. J., 2008, "Geometric Modeling of Inclusions as Ellipsoids," *NASA/TM—2008-215477*.
- Boyce, B. L., and R. O. Ritchie, 2001, "Effect of Load Ratio and Maximum Stress Intensity on the Fatigue Threshold in Ti-6Al-4V," *Engineering Fracture Mechanics*, Vol. 68, 2001, pp. 129-147.
- Cai, J. and R. L. Prentice, 1995, "Estimating Equations for Hazard Ratio Parameters Based on Correlated Failure Time Data," *Biometrika*, Vol. 82, pp. 151-164.
- Caton, M. J., R. John, W. J. Porter, and M. E. Burba, "Stress Ratio Effects on Small Fatigue Crack Growth in Ti-6Al-4V," in review.
- Chan, K. S., 1999, "Fatigue Crack Growth Threshold of TiAl Alloys," Proc. 2nd International Symposium Gamma Titanium Aluminides, TMS, pp. 517-525.
- Chen, B. E., J. L. Kramer, M. H. Greene, and P. S. Rosenberg, 2008, "Competing Risks Analysis of Correlated Failure Time Data," *Biometrics*, Vol. 64, pp. 172-178.

- Crowder, M., 1991, "On the Identifiability Crisis in Competing Risks Analysis," *Scandinavian Journal of Statistics, Theory, and Applications*, Vol. 18, No. 3, pp. 223-233.
- Crowder, M., 1997, "A Test for Independence of Competing Risks with Discrete Failure Times," *Lifetime Data Analysis*, Vol. 3, pp. 215-223.
- Cruz-Orive, L. M., 1976, "Particle Size-Shape Distributions: the General Spheroid Problem I: Mathematical Model," *Journal of Microscopy*, Vol. 107, pp. 235-253.
- Cruz-Orive, L. M., 1977, "Particle Size-Shape Distributions: the General Spheroid Problem II: Stochastic Model and Practical Guide," *Journal of Microscopy*, Vol. 112, pp. 153-167.
- Davidson, D., K. Chan, R. McClung, and S. Hudak, 2003, "Small Fatigue Cracks," *Comprehensive Structural Integrity, Vol. 4: Cyclic Loading and Fatigue*, Elsevier, pp. 129-164.
- Dignam, J. J., K. Wieland, and P. J. Rathouz, 2007, "A Missing Data Approach to Semi-Competing Risks Problems," *Statistics in Medicine*, Vol. 26, pp. 837-856.
- El Haddad, M. H., K. N. Smith, and T. H. Topper, 1979, "Fatigue Crack Propagation of Short Cracks," *Journal of Engineering Materials and Technology, Trans. ASME*, Vol. 101, pp. 42-46.
- Enright, M. P. and D. M. Frangopol, 1998, "Failure Time Prediction of Deteriorating Fail-Safe Structures," *Journal of Structural Engineering*, Vol. 124, No. 12, pp. 1448-1457.
- Enright, M. P., Y-D. Lee, R. C. McClung, L. Huyse, G. R. Leverant, H. R. Millwater, and S. H. K. Fitch, 2003, "Probabilistic Surface Damage Tolerance Assessment of Aircraft Turbine Rotors," Paper GT-2003-38731, Proceedings of ASME Turbo Expo 2003, Atlanta, Georgia.
- Enright, M. P., L. Huyse, and R. C. McClung, 2005, "Fracture Mechanics-Based Probabilistic Life Prediction of Components with Large Numbers of Inherent Material Anomalies," Proceedings, Ninth International Conference on Structural Safety and Reliability (ICOSSAR), Rome, Italy, pp. 601-607.
- Enright, M. P. and L. Huyse, 2006, "Methodology for Probabilistic Life Prediction of Multiple Anomaly Materials," *AIAA Journal*, Vol. 44, No. 4, pp. 787-793.
- Forman, R. G. and V. Shivakumar, 1986, "Growth Behavior of Surface Cracks in the Circumferential Plane of Solid and Hollow Cylinders," *Fracture Mechanics: Seventeenth Volume, ASTM STP 905*, American Society for Testing and Materials, pp. 59-74.
- Gabb, T. P., P. J. Bonacuse, L. J. Ghosn, J. W. Sweeney, A. Chatterjee, and K. A. Green, 2000, "Assessments of Low Cycle Fatigue Behavior of Powder Metallurgy Alloy U720," *Fatigue and Fracture Mechanics: 31st Volume, ASTM STP 1389*, pp. 110-127. Also published as NASA/TM-2000-209418.

- Gabb, T. P., J. Telesman, P. T. Kantzos, J. W. Sweeney, and P. F. Browning, 2002, "Effects of High-Temperature Exposures on the Fatigue Life of Superalloy Udimet® 720," NASA/TM-2002-211570.
- Gabb, T. P., J. Telesman, P. T. Kantzos, P. J. Bonacuse, and R. L. Barrie, 2003, "Initial Assessment of the Effects of Non-Metallic Inclusions on Fatigue Life of Powder Metallurgy Processed Udimet® Alloy 720," *Advanced Materials and Processes for Gas Turbines*, Proceedings of the International Conference, TMS, 2003, pp. 237-244. Also published as NASA/TM-2002-211571, August 2002.
- Gabb, T. P., J. Telesman, P. T. Kantzos, P. J. Bonacuse, R. L. Barrie, and D. J. Hornbach, 2004, "Stress Relaxation in Powder Metallurgy Superalloy Disks," *TMS Letters*, Vol. 5, pp. 115-116.
- Gaynor, J. J., E. J. Feuer, C. C. Tan, D. H. Wu, C. R. Little, D. J. Straus, B. D. Clarkson, and M. F. Brennan, 1993, "On the Use of Cause-Specific Failure and Conditional Failure Probabilities: Examples from Clinical Oncology Data," *Journal of the American Statistical Association*, Vol. 88, No. 422, pp. 400-409.
- Ghosn, L. J., P. T. Kantzos, R. L. Barrie, and P. J. Bonacuse, 2003, "Unfolding the Ceramic Inclusion Size Distribution in a Powder Metallurgy Alloy from Planar Sections," *Materials Science and Technology 2003*, Chicago, Illinois, November 11, 2003 (presentation only).
- Ghosn, M., J. Telesman, P. Bonacuse, L. Ghosn, and P. Kantzos, 2005, "Probabilistic Analysis of Fatigue Life of Superalloy Metals," *Safety and Reliability of Engineering Systems and Structures*, Proceedings ICOSSAR 2005, pp. 3675-3681. Another unpublished report without listed date or authorship ("Statistical Analysis and Probabilistic Fatigue Life Estimation of Seeded Udimet 720 Superalloy Specimens"), appears to be a longer version of the 2005 ICOSSAR paper.
- Haldar, A. and S. Mahadevan, 2000, *Probability, Reliability, and Statistical Methods in Engineering Design*, John Wiley, New York.
- Hoyland, A. and M. Rausand, 1994, *System Reliability Theory Models and Statistical Methods*, John Wiley, New York, pp. 355-414.
- Jha, S. K., M. J. Caton, and J. M. Larsen, 2008, "Mean vs. Life-Limiting Fatigue Behavior of a Nickel-Based Superalloy," *Superalloys 2008*, 11th International Symposium on Superalloys, Champaign, Pennsylvania, TMS, pp. 565-572.
- Kantzog, P. T., R. Barrie, P. Bonacuse, T. Gabb, and J. Telesman, 2003, "The Effects of Forging Strain on Ceramic Inclusions in a Disk Superalloy," *Advanced Materials and Processes for Gas Turbine Engines*, Proceedings of the International Conference, TMS, pp. 245-254.
- Kantzog, P., P. Bonacuse, J. Telesman, T. Gabb, R. Barrie, and A. Banik, 2004, "The Effect of Powder Cleanliness on the Fatigue Behavior of Powder Metallurgy Ni-Disk Alloy Udimet 720," *Superalloys 2004*, Proceedings of the 10th International Symposium on Superalloys, TMS, pp. 409-417.

- Kantzios, P., 2006, "Probabilistic Lifting Approach for P/M Nickel Turbine Disks," February 24, 2006 charts (unpublished).
- Kaplan, E.L. and P. Meier, 1958, "Nonparametric Estimation from Incomplete Observations," *Journal of the American Statistical Association*, Vol. 53, pp. 457-481.
- Kitagawa, H. and S. Takahashi, 1976, "Applicability of Fracture Mechanics to Very Small Cracks or the Cracks in the Early Stage," Proceedings of the 2nd International Conference on Mechanical Behavior of Materials, Boston, Massachusetts, pp. 627-631.
- Klein, J. P. and M. L. Moeschberger, 1988, "Bounds on Net Survival Probabilities for Dependent Competing Risks," *Biometrics*, Vol. 44, pp. 529-538.
- Laz, P. J., K. S. Chan, R. C. McClung, and G. R. Leverant, 2003, "Effects of CTE-Induced Residual Stresses Around Hard Alpha Particles on Fatigue Crack Growth in Ti-6Al-4V," *Fatigue and Fracture of Engineering Materials and Structures*, Vol. 26, No. 12, pp. 1145-1157.
- Lee, Y.-D., R. C. McClung, and G. G. Chell, 2008, "An Efficient Stress Intensity Factor Solution Scheme for Corner Cracks at Holes under Bivariant Stressing," *Fatigue and Fracture of Engineering Materials and Structures*, Vol. 31, No. 11, pp. 1004-1016.
- Lenets, Y., R. S. Bellows, and H. F. Merrick, 2000, "Propagation Behavior of Naturally Initiated Fatigue Cracks in Round Bars of Ti-6Al-4V," 5th National Turbine Engine High Cycle Fatigue Conference, Chandler, Arizona.
- Lenets, Y., R. Nelson, and H. Merrick, 2002, "Growth of Small Cracks at Different Stress Ratios," 7th National Turbine Engine High Cycle Fatigue Conference, Palm Beach, Florida.
- Leverant, G. R., R. C. McClung, H. R. Millwater, and M. P. Enright, 2003, "A New Tool for Design and Certification of Aircraft Turbine Rotors", *Journal of Engineering for Gas Turbines and Power*, Vol. 126, No. 1, pp. 155-159.
- Leverant, G. R., R. C. McClung, H. R. Millwater, and M. P. Enright, 2004, "A New Tool for Design and Certification of Aircraft Turbine Rotors," by *ASME Journal of Engineering for Gas Turbines and Power*, Vol. 126, pp. 155-159. Also published as Paper GT-2002-30303, Proceedings of ASME Turbo Expo 2002, Amsterdam, The Netherlands.
- McClung, R. C., K. S. Chan, S. J. Hudak, Jr., and D. L. Davidson, 1996, "Behavior of Small Fatigue Cracks," *ASM Handbook*, Vol. 19, *Fatigue and Fracture*, ASM International, pp. 153-158.
- McClung, R. C., B. H. Lawless, M. Gorelik, C. Date, Y. Gill, and R. S. Piascik, 1999, "Fatigue Crack Growth of Titanium Rotor Alloys in Vacuum And Air," *Fatigue Behavior of Titanium Alloys*, R. R. Boyer, D. Eylon, and G. Lutjering, Eds., The Minerals, Metals, and Materials Society, pp. 211-218.

- McClung, R. C., M. P. Enright, H. R. Millwater, G. R. Leverant, and S. J. Hudak, Jr., 2004a, "A Software Framework for Probabilistic Fatigue Life Assessment of Gas Turbine Engine Rotors," *Journal of ASTM International*, Vol. 1, Paper JAI11563. Also published in *Probabilistic Aspects of Life Prediction, ASTM STP 1450*, ASTM International, pp. 199-215.
- McClung, R. C., M. P. Enright, Y.-D. Lee, L. Huyse, and S. H. K. Fitch, 2004b, "Efficient Fracture Design for Complex Turbine Engine Components," Paper GT-2004-53323, *Proceedings of ASME Turbo Expo 2004*, Vienna, Austria.
- McClung, R. C., 2007, "A Literature Survey on the Stability and Significance of Residual Stresses During Fatigue," *Fatigue and Fracture of Engineering Materials and Structures*, Vol. 30, No. 3, pp. 173-205.
- McClung, R. C., and M. P. Enright, 2009, "Extension of Bimodal Failure Distribution Concepts," Final Report to Air Force Research Laboratory, SwRI Project No. 18.13663, GDIT Subcontract Order No. USAF-5212-STI-SC-0029.
- McClung, R. C., Y.-D. Lee, M. P. Enright, and S. H. K. Fitch, 2009, "A New Computational Framework for Fatigue Crack Growth Analysis of Components," 12th International Conference on Fracture, Ottawa, Canada.
- McKeighan, P. C., A. E. Nicholls, L. C. Perocchi, and R. C. McClung, 2001, "Sensing Crack Nucleation and Growth in Hard Alpha Defects Embedded in Ti-6Al-4V Alloy," *Nontraditional Methods of Sensing Stress, Strain and Damage in Materials and Structures: Second Volume, ASTM STP 1323*, American Society for Testing and Materials, pp. 15-35.
- Meeker, W. Q. and L. A. Escobar, 1998, *Statistical Methods for Reliability Data*, John Wiley, New York, pp. 129-130.
- Melchers, R., 1999, *Structural Reliability Analysis and Prediction*, Second Edition, Wiley, New York.
- Millwater, H., J. Wu, D. S. Riha, M. P. Enright, G. R. Leverant, R. C. McClung, C. Kuhlman, G. Chell, Y.-D. Lee, S. H. K. Fitch, and J. Meyer, 2000, "A Probabilistically-Based Damage Tolerance Analysis Computer Program for Hard Alpha Anomalies in Titanium Rotors," ASME Paper 2000-GT-0421, *Proceedings of ASME Turbo Expo 2000*, Munich, Germany.
- Moeschberger, M. L. and H. A. David, 1974, "Life Tests Under Competing Causes of Failure," *Technometrics*, Vol. 16, pp. 39-47.
- Moeschberger, M. L., and J. P. Klein, 1995, "Statistical Methods for Dependent Competing Risks," *Lifetime Data Analysis*, Vol. 1, pp. 195-204.
- Nelson, W., 1972, "Theory and Application of Hazard Plotting for Censored Failure Data," *Technometrics*, Vol. 14, pp. 945-966.
- Ohser, J. and F. Mücklich, 2000, "Statistical Analysis of Microstructures in Material Science," John Wiley & Sons, LTD, West Sussex, England.

- Ohser, J. and K. Sandau, 2000, "Considerations about the Estimation of the Size Distribution in Wicksell's Corpuscle Problem," in *Statistical Physics and Spatial Statistics*, Mecke and Stoyan (Eds), Springer-Verlag, New York, pp. 185-202.
- Pepe, M. S. and M. Mori, 1993, "Kaplan-Meier, Marginal or Conditional Probability Curves in Summarizing Competing Risks Failure Time Data?," *Statistics in Medicine*, Vol. 12, No. 8, pp. 737-751.
- Peterson, A. V., 1976, "Bounds for a Joint Distribution Function with Fixed Subdistribution Functions: Applications to Competing Risks," *Proceedings of the National Academy of Sciences*, Vol. 73, pp. 11-13.
- Roth, P. G., J. C. Murray, J. E. Morra, and J. M. Hyzak, 1994, "Heavy Liquid Separation: A Reliable Method to Characterize Inclusions in Metal Powder," *Characterization, Testing, and Quality Control*, Proceedings of the 1994 International Conference on Powder Metallurgy and Particulate Materials, Vol. 2, Princeton, NJ: Metal Powder Industries Federation, pp. 1-12.
- Roth, P. G., 1998, "Probabilistic Rotor Design System – Final Report," AFRL-PR-WP-TR-1999-2122.
- Sheldon, J. W., K. R. Bain, and J. K. Donald, 1999, "Investigation of the Effects of Shed-Rate, Initial K_{max} , and Geometric Constraint on ΔK_{th} in Ti-6Al-4V at Room Temperature," *International Journal of Fatigue*, Vol. 21, pp. 733-741.
- Slud, E. V. and L. V. Rubinstein, 1983, "Dependent Competing Risks and Summary Survival Curves," *Biometrika*, Vol. 70, pp. 643-649.
- Tan, Z., 2007, "Estimation of Exponential Component Reliability from Uncertain Life Data in Series and Parallel Systems," *Reliability Engineering and System Safety*, Vol. 92, pp. 223-230.
- Tanaka, K., Y. Nakai, and M. Yamashita, 1981, "Fatigue Growth Threshold of Small Cracks," *International Journal of Fracture*, Vol. 17, pp. 519-533.
- Telesman, J., 2002, "Low Cycle Fatigue Behavior of a Udimet 720 Superalloy Seeded with Alumina Inclusions," 2002 ASME International Mechanical Engineering Conference, Fatigue of High Temperature Materials, New Orleans, November 17, 2002 (presentation only).
- Telesman, J., P. Kantzos, T. Gabb, and P. Bonacuse, 2006, "Fatigue Initiation and Propagation Behavior of Naturally Initiated Cracks," P-SAR 2006, Jacksonville, Florida (presentation only).
- Telesman, J., T. Gabb, and P. Bonacuse, 2007, "Effect of Surface Enhancement Treatments on LCF Behavior in a Udimet 720 Superalloy," P-SAR 2007, San Diego, California (presentation only).

- Thoft-Christensen, P. and Y. Murotsu, 1986, *Application of Structural Systems Reliability Theory*, Springer Verlag, New York.
- Wicksell, S.D., 1925, “The Corpuscle Problem I: Case of Spherical Corpuscles,” *Biometrika*, Vol. 17, pp. 84-99.
- Wicksell, S.D., 1926, “The Corpuscle Problem II: Case of Ellipsoidal Corpuscles,” *Biometrika*, Vol. 18, pp. 151-172.
- Wu, Y. T., M. P. Enright, and H. R. Millwater, 2002, “Probabilistic Methods for Design Assessment of Reliability with Inspection,” *AIAA Journal*, Vol. 40, No. 5, pp. 937-946.
- Zheng, M. and J. P. Klein, 1995, “Estimates of Marginal Survival for Dependent Competing Risks Based on an Assumed Copula,” *Biometrika*, Vol. 82, pp. 127-138.

REPORT DOCUMENTATION PAGE			Form Approved OMB No. 0704-0188		
<p>The public reporting burden for this collection of information is estimated to average 1 hour per response, including the time for reviewing instructions, searching existing data sources, gathering and maintaining the data needed, and completing and reviewing the collection of information. Send comments regarding this burden estimate or any other aspect of this collection of information, including suggestions for reducing this burden, to Department of Defense, Washington Headquarters Services, Directorate for Information Operations and Reports (0704-0188), 1215 Jefferson Davis Highway, Suite 1204, Arlington, VA 22202-4302. Respondents should be aware that notwithstanding any other provision of law, no person shall be subject to any penalty for failing to comply with a collection of information if it does not display a currently valid OMB control number.</p> <p>PLEASE DO NOT RETURN YOUR FORM TO THE ABOVE ADDRESS.</p>					
1. REPORT DATE (DD-MM-YYYY) 01-03-2011		2. REPORT TYPE Final Contractor Report		3. DATES COVERED (From - To)	
4. TITLE AND SUBTITLE Integration of NASA-Developed Lifing Technology for PM Alloys into DARWIN®			5a. CONTRACT NUMBER NNC08CB06C		
			5b. GRANT NUMBER		
			5c. PROGRAM ELEMENT NUMBER		
6. AUTHOR(S) McClung, R., Craig; Enright, Michael, P.; Liang, Wuwei			5d. PROJECT NUMBER		
			5e. TASK NUMBER		
			5f. WORK UNIT NUMBER WBS 877868.02.07.03.05.01		
7. PERFORMING ORGANIZATION NAME(S) AND ADDRESS(ES) National Aeronautics and Space Administration John H. Glenn Research Center at Lewis Field Cleveland, Ohio 44135-3191			8. PERFORMING ORGANIZATION REPORT NUMBER E-17619		
9. SPONSORING/MONITORING AGENCY NAME(S) AND ADDRESS(ES) National Aeronautics and Space Administration Washington, DC 20546-0001			10. SPONSORING/MONITOR'S ACRONYM(S) NASA		
			11. SPONSORING/MONITORING REPORT NUMBER NASA/CR-2011-216977		
12. DISTRIBUTION/AVAILABILITY STATEMENT Unclassified-Unlimited Subject Category: 39 Available electronically at http://www.sti.nasa.gov This publication is available from the NASA Center for AeroSpace Information, 443-757-5802					
13. SUPPLEMENTARY NOTES					
14. ABSTRACT In recent years, Southwest Research Institute (SwRI) and NASA Glenn Research Center (GRC) have worked independently on the development of probabilistic life prediction methods for materials used in gas turbine engine rotors. The two organizations have addressed different but complementary technical challenges. This report summarizes a brief investigation into the current status of the relevant technology at SwRI and GRC with a view towards a future integration of methods and models developed by GRC for probabilistic lifing of powder metallurgy (P/M) nickel turbine rotor alloys into the DARWIN (Darwin Corporation) software developed by SwRI.					
15. SUBJECT TERMS Fatigue; Probabilistic life prediction; P/M disk superalloy; Fatigue crack growth					
16. SECURITY CLASSIFICATION OF:			17. LIMITATION OF ABSTRACT UU	18. NUMBER OF PAGES 83	19a. NAME OF RESPONSIBLE PERSON STI Help Desk (email:help@sti.nasa.gov)
a. REPORT U	b. ABSTRACT U	c. THIS PAGE U			19b. TELEPHONE NUMBER (include area code) 443-757-5802

